

THE BELL SYSTEM TECHNICAL JOURNAL

DEVOTED TO THE SCIENTIFIC AND ENGINEERING
ASPECTS OF ELECTRICAL COMMUNICATION

Volume 56

January 1977

Number 1

Copyright © 1977, American Telephone and Telegraph Company. Printed in U.S.A.

Engineering Traffic Networks for More Than One Busy Hour

By M. EISENBERG

(Manuscript received July 6, 1976)

A procedure is described that is used to engineer traffic networks for more than one hour of point-to-point load data. The procedure differs significantly from existing methods, which are based upon the concept of "economic load on the last trunk" (ECCS). (When the peak-load hours on most routes coincide, however, the procedure reduces to the ECCS method.) This "multihour" procedure has been implemented in a computer program used in design studies of three end offices in the Los Angeles local network. For the cases examined, the multihour technique produced networks whose costs averaged approximately 7 percent below those achieved with the presently used single-hour methods. Thus, the multihour technique appears to promise considerable cost benefits in future network designs.

I. INTRODUCTION

In this paper, we describe a procedure used to engineer networks for more than one hour of point-to-point traffic data. Specifically, for a given routing structure, set of switching and transmission costs, and point-to-point offered load between each pair of offices for each of several hours, this method produces a (nearly) least-cost network that satisfies the constraint that the blocking probabilities on all final groups be below

a predetermined value (the "grade of service") for all hours. This multihour procedure is a major departure from currently used single-hour methods based upon the concept of "economic load on the last trunk"¹ (ECCS). The new technique reduces to the ECCS method, however, when the peak-load hours on most routes coincide. After computer programs are written and operating practices are developed, this new procedure should become suitable for routine field use.

The underlying theoretical basis for multihour engineering was developed by Rapp.² Rather than attempting to construct an optimal solution, however, Rapp proposed an alternative approximate technique. Our aim is to get an exact solution. Although we do not fully achieve this aim, we obtain significant improvement in network performance relative to a single-hour approach.

A computer program that implements the multihour procedure was used to study three end offices located in the Los Angeles area. For the cases examined, where a significant amount of noncoincidence of peak-load hours existed, the multihour method produced network cost savings averaging 7 percent over the single-hour methods currently employed. In addition, in each case, a very sizable reduction of tandem switching load was achieved.

II. SINGLE-BUSY-HOUR ENGINEERING

Before discussing the multihour technique, let us first review the considerations involved in engineering for a single hour. Figure 1 depicts a single high-usage group, the direct route, overflowing to an alternate route. (For now, we make the simplifying assumption that the alternate route consists only of a single trunk group.) We later consider more realistic alternate-route configurations.) The cost per trunk of the direct route is C_D , and the cost per trunk of the alternate route is C_A (which is assumed to include the cost of tandem switching). The offered load in the hour being considered is a . The problem is to determine the value of n , the number of trunks in the high-usage group, so that the total cost is minimized; however, the minimization of cost is subject to the con-

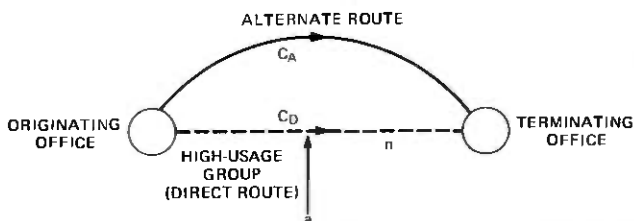


Fig. 1—High-usage trunk group overflowing to alternate route.

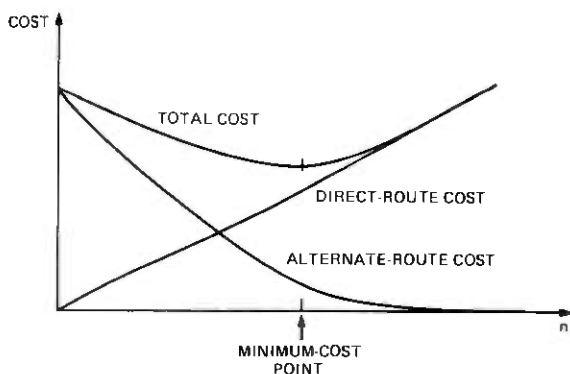


Fig. 2—Single-hour trunk-group sizing.

straint that the blocking probability on the alternate route is below a predetermined value.

The total cost is equal to the cost of trunks on the direct route plus the cost of trunks on the alternate route. To simplify matters, it can be assumed that the alternate-route cost is composed of a fixed component (the cost of carrying the “background” alternate-route load) plus a variable component (the cost of carrying the overflow) whose magnitude is proportional to the amount of overflow traffic.* Since the cost required to carry the background alternate-route load is independent of n , we may neglect this component and write the cost to be minimized as

$$\text{COST} = \frac{C_A}{\gamma} aB(n,a) + C_D n. \quad (1)$$

Here, γ is the marginal capacity of the alternate route, and $B(n,a)$ is the Erlang-B blocking probability. The marginal capacity is the amount of additional traffic that it is assumed can be offered to the alternate route, at fixed blocking, for the addition of one trunk. Thus, $aB(n,a)$ is the load overflowing to the alternate route, $1/\gamma aB(n,a)$ is the assumed number of additional alternate-route trunks required to carry this overflow, and $C_A/\gamma aB(n,a)$ is the cost of these additional trunks. $C_D n$ is, of course, the cost of trunks on the direct route. These two components of cost and their sum are shown as a function of n in Fig. 2. The total cost is seen to be a U-shaped curve having a minimum at the point indicated. This point is determined by the condition that the rate of change of COST with respect to n be equal to zero:

* This assumption is not quite true, particularly when the peakedness of the overflow traffic is taken into account. Nevertheless, in most cases of interest, the assumption yields a configuration whose cost differs negligibly from the optimal plan.

$$\frac{d}{dn} \text{COST} = 0. \quad (2)$$

From eq. (1), this implies

$$-\frac{d}{dn} [aB(n,a)] = \frac{\gamma}{C_R}, \quad (3)$$

where $C_R = C_A/C_D$ is the cost ratio, as discussed in Ref. 1. The quantity on the left-hand side of eq. (3), the rate of change of overflow with respect to the number of trunks on the high-usage group, is very nearly equal to the "load on the last trunk." * The quantity on the right-hand side of eq. (3) is the "economic" load on the last trunk, or ECCS (CCS is 100 call seconds per hour). Thus, the minimum cost is achieved by sizing the high-usage group such that its load on the last trunk is equal to its "economic" value, γ/C_R .

In this discussion, it is assumed that the network is designed to carry only a single hour's load. In practice, of course, the load on the high-usage group, as well as the background load on the alternate route, varies from hour to hour. The question arises as to which of the hours of loads should be used to engineer the group.

It is clear that it would be uneconomical to engineer a high-usage group for its individual group busy hour if this hour does not coincide with the busy hour of the alternate route; the alternate route has spare capacity in off-hours. A moment's reflection reveals that the appropriate hour for which to size the group is the alternate-route's busy hour; only in this hour does the cost of carrying the overflow traffic from the high-usage group need to be considered.

This fact has long been recognized by traffic engineers.¹ The method of choosing the engineering hour which was adopted, consequently, involved the concept of the "cluster busy hour." A "cluster" is defined as a set of high-usage trunk groups originating at the same office and overflowing to a common alternate-route leg, together with the alternate-route leg itself. The cluster busy hour is defined as that time-consistent hour for which the total load offered to the cluster (specifically, the sum of the carried loads on all high-usage groups in the cluster, plus the offered load on the alternate-route leg) is maximum. It was assumed that the alternate-route busy hour would be the same as the cluster busy hour, and thus the adopted engineering practice was to size every high-usage group for its cluster-busy-hour load.

The difficulties that can arise with this method, however, are illustrated by the example in Fig. 3. In the figure, we show a simple network

* "Load on the last trunk" is defined to be $a[B(n-1,a)-B(n,a)]$ if the group has n trunks.

cluster consisting of two one-way outgoing high-usage groups, A and B, overflowing to a common alternate route, F. The cost ratio is assumed to be 2, and the marginal capacity of the alternate route is assumed to be 28 CCS. Since a total of 1100 CCS is offered to the cluster in Hour 1 and 1000 CCS is offered in Hour 2, the cluster busy hour is Hour 1. For the Hour-1 loads the ECCS method yields a network consisting of 10 and 26 trunks on high-usage groups A and B, respectively. It is seen, however, that this network has a high overflow from group A during Hour 2. This high overflow occurs because the group is engineered for only 300 CCS, while in Hour 2 the offered load is 600 CCS. As a consequence, the total load on the alternate route is greater during Hour 2, contradicting the original assumption that the alternate route was busier in Hour 1. To guarantee a given grade of service in both hours, it is necessary to add trunks to the alternate route for its load in Hour 2.* Under the assumption that the number of extra alternate-route trunks required to carry this load is $n_F = 276/\gamma = 9.8$, we find the total cost of the network to be \$55.60.†

Figure 3 also shows the network derived on the basis of the Hour-2 loads. For this network, due to high overflow from group B during Hour 1, the final-group busy hour is Hour 1, again contradicting the initial assumption. The total cost of this network is \$59.40.

The third network in Fig. 3 was derived using the multihour technique. As can be seen, this network nearly equalizes the load on the alternate route in the two hours. (In general, the multihour technique tends to equalize the hourly loads on the alternate route or routes.) The cost of this network is \$46.80, substantially less than either single-hour network.

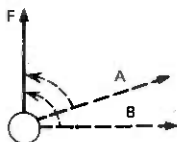
This example illustrates some of the problems inherent in single-hour engineering methods and the potential improvement obtainable with the multihour technique. We describe this technique in detail in Section III.

III. MULTIHOUR ENGINEERING

Figure 4 again shows a single high-usage group overflowing to an alternate route, where the trunk costs C_D and C_A are defined as before. The loads a_1 and a_2 are offered to the high-usage group in Hours 1 and 2, respectively. Also shown in the figure are the background loads in

* In practice, the servicing up of the alternate route might take place after the engineered network was in operation, when the service degradation in the side hour was actually observed.

† The use of an assumed marginal capacity for the alternate route, while reasonable for the purpose of sizing high-usage groups, is actually inappropriate for determining trunk requirements on the alternate route. Our aim here, however, is merely to obtain a rough indication of alternate-route cost for comparative purposes.



		OFFERED LOAD		COST RATIO = 2 $\gamma = 28\text{CCS}$ ECCS = 14
		HOUR 1	HOUR 2	
A		300	600	
B		800	400	
		1100	1000	

HOUR 1 ENGINEERING

$$n_A = 10$$

$$n_B = 26$$

		OVERFLOW		TOTAL COST = $10 + 26 + 2 \times 9.8$ = 55.6
		HOUR 1	HOUR 2	
A		41	276	
B		56	0	
		97	276	$\Rightarrow n_F = 9.8$

HOUR 2 ENGINEERING

$$n_A = 20$$

$$n_B = 13$$

		OVERFLOW		TOTAL COST = $20 + 13 + 2 \times 13.2$ = 59.4
		HOUR 1	HOUR 2	
A		0	47	
B		369	49	
		369	96	$\Rightarrow n_F = 13.2$

MULTIHOUR ENGINEERING

$$n_A = 14$$

$$n_B = 20$$

		OVERFLOW		TOTAL COST = $14 + 20 + 2 \times 6.4$ = 46.8
		HOUR 1	HOUR 2	
A		6	165	
B		172	0	
		178	165	$\Rightarrow n_F = 6.4$

Fig. 3—Comparison of engineering methods in the presence of noncoincidence.

Hours 1 and 2, A_1 and A_2 , offered to the alternate route. The background loads are the total loads offered to the alternate route, not including the overflow from the high-usage group under consideration.

In sizing the high-usage group, we attempt to minimize total cost. We

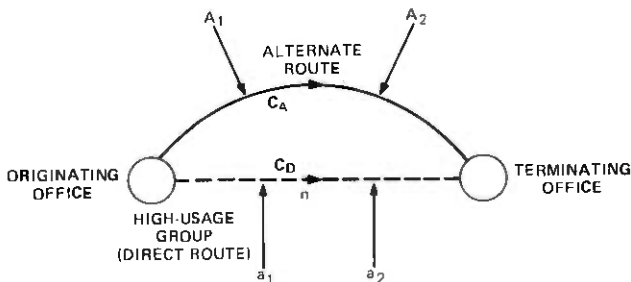


Fig. 4—High-usage group with offered load for two hours.

must recognize, however, that since the grade of service must be guaranteed for both hours, the cost of the alternate route depends upon the *greater* of its total offered loads in Hours 1 and 2. The cost is thus given by the formula*

$$\text{COST} = \frac{C_A}{\gamma} \text{Max} \left\{ \begin{array}{l} A_1 + a_1B(n, a_1) \\ A_2 + a_2B(n, a_2) \end{array} \right\} + C_D n. \quad (4)$$

The total load on the alternate route during Hour 1 is equal to the background load A_1 plus the overflow from the high-usage group, $a_1B(n, a_1)$. The total load during Hour 2, similarly, is $A_2 + a_2B(n, a_2)$. The controlling load for the alternate route is the greater of these. The total cost equals the maximum alternate-route load times C_A/γ plus the cost of the high-usage group $C_D n$.†

The term "multihour engineering" denotes the process of designing a network by searching along the cost curve of eq. (4) for each group—or actually, the more general cost curve of eq. (5) discussed below—to determine the minimum-cost point. The optimal number of high-usage trunks in each group determined by the use of this technique varies depending upon the loads and costs. Figure 5 shows two different cases that can arise.

In Case I, the plot of cost curves shows that the Hour-1 load on the alternate route dominates the Hour-2 load for all n . In this case, therefore, the maximization operator of eq. (4) always selects Hour 1, as suggested by the shading of this cost curve in the figure. Thus, in Case I, the multihour method reduces exactly to the single-hour method by using the Hour-1 load. This example illustrates the case discussed above, where the use of the cluster-busy-hour concept yields the correct solution. Note that the correct solution is confirmed if the actual alternate-route busy hour, determined by examining the load offered *after* engineering, is the same as that originally assumed.

Case II in Fig. 5 illustrates a different type of behavior. In this example, the background load on the alternate route is greater in Hour 2, and the offered load on the high-usage group is greater in Hour 1. Thus, for n small there is heavy overflow during Hour 1, and this causes the total alternate-route load to be greater in Hour 1. For n large, however, the overflow is small, so that the alternate-route load is greater in Hour 2 due to the background component. The costs of carrying the alternate-

* This formula, in the more general form of eq. (5), was first given by Rapp (Ref. 2).

† The equation again is not strictly correct since the cost of the alternate route is not proportional to its offered load. However, we shall not use eq. (4) to evaluate the absolute cost, but only to determine its relative minimum with respect to n . For this purpose, the equation yields accurate results.

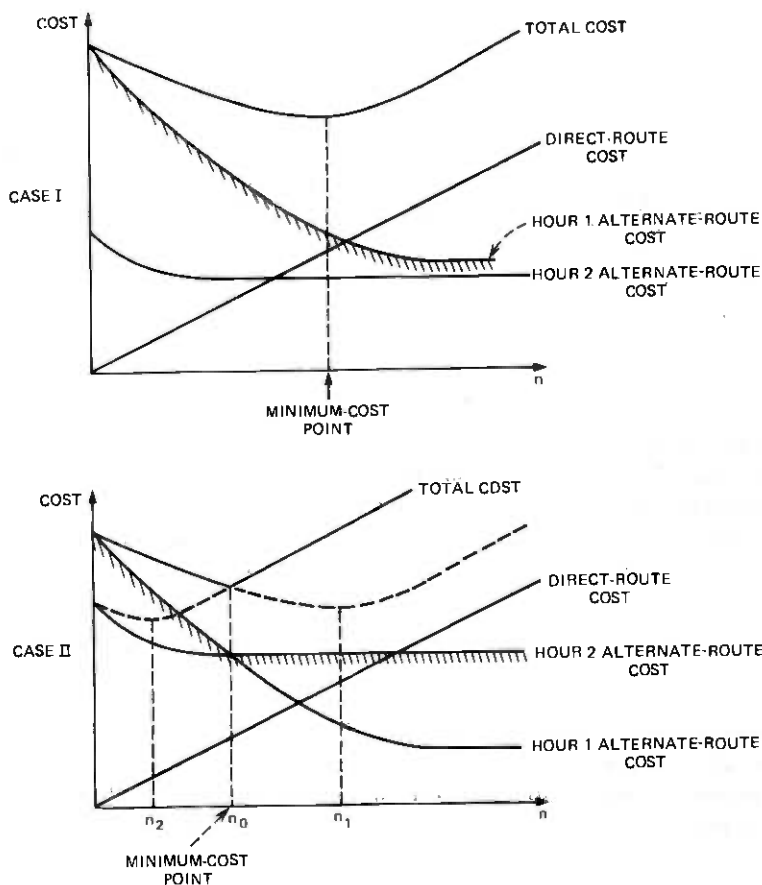


Fig. 5—Multihour trunk-group sizing for the network in Fig. 4.

route loads in Hours 1 and 2 are drawn in the figure and are seen to intersect. To the left of the intersection point, the cost of the alternate route is determined by the Hour-1 load, and to the right, the cost is determined by the Hour-2 load. The maximization operator selects these portions of the curves; this is suggested by the shading in the diagram. The total cost is the sum of the alternate-route cost and the straight-line direct-route cost and is represented by the solid-line curve on the top of the diagram. The curve shows a minimum at the point $n = n_0$ and has a discontinuous derivative at this point. The calculation of n_0 for this example, then, differs radically from the calculation in our previous examples. Whereas before, the minimum-cost design was determined by requiring the load on the last trunk to be equal to a prescribed value,

here n_0 is determined to be that value of n which equalizes the loads on the alternate route in the two hours.

It is instructive to observe what would happen if a single-hour method were used in this example. If Hour 1 were chosen as the engineering base hour, the resulting high-usage group size would be n_1 , shown in the diagram. Note that if n_1 trunks were installed, the alternate route would actually be busier in Hour 2 than in Hour 1, contrary to what was assumed. The total cost of the network after adding trunks to the alternate route to handle the Hour-2 load would be higher than at the optimum point n_0 . Similarly, if Hour 2 were the selected engineering base hour, the resulting group size would be n_2 . The alternate route would actually be busier in Hour 1, and again the total cost would be higher than optimum.

Up to this point we have, for simplification, been treating the case where the alternate route has consisted simply of a single trunk group. Actually, of course, the alternate-route configuration is more complicated. Figure 6 shows one possible arrangement where the alternate route consists of a final group, a tandem switch, and a tandem-completing group. The background loads for the two hours are F_1 and F_2 for the final, S_1 and S_2 for the tandem switch, and T_1 and T_2 for the tandem-completing group. The cost per trunk of the final group is C_F and the cost per trunk of the tandem-completing group is C_T . We assume that the switching cost is proportional to the load and is equal to C_S per CCS switched. The cost of each component of the alternate route again is determined by the maximum traffic offered to it. Thus, the engineering of the high-usage group requires three separate busy-hour comparisons.

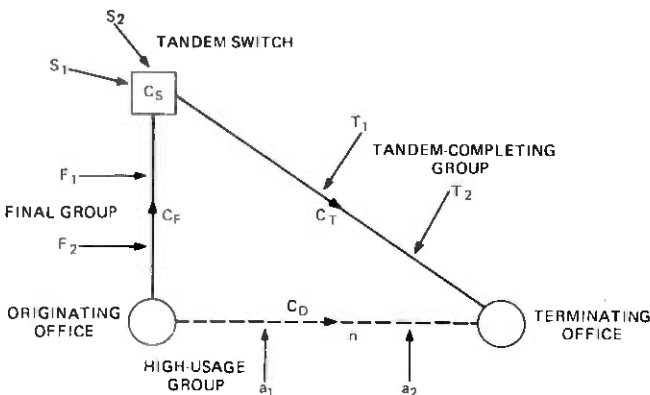


Fig. 6—Typical alternate-route configuration.

The total cost is given by the formula

$$\text{COST} = \frac{C_F}{\gamma} \text{Max} \left\{ \begin{array}{l} F_1 + a_1 B(n, a_1) \\ F_2 + a_2 B(n, a_2) \end{array} \right\} + C_S \text{Max} \left\{ \begin{array}{l} S_1 + a_1 B(n, a_1) \\ S_2 + a_2 B(n, a_2) \end{array} \right\} \\ + \frac{C_T}{\gamma} \text{Max} \left\{ \begin{array}{l} T_1 + a_1 B(n, a_1) \\ T_2 + a_2 B(n, a_2) \end{array} \right\} + C_D n, \quad (5)$$

which is explained exactly like eq. (4).

Figure 7 shows one possible example of the behavior of the cost curves as a function of n . In this example, the cost curves of the final group during Hours 1 and 2 intersect at a certain point. The switch cost curves also intersect, but at a different point. The tandem-completing cost is completely dominated by the Hour-1 load in this example. The sum of these three costs, plus the straight-line direct-route cost, yields the total cost curve shown at the bottom of the figure. In this example, the optimum design requires equalization of the switch loads in Hours 1 and 2. Of course, depending on the loads and costs, the minimum-cost point could instead have required equalizing of the final loads or of the tandem-completing loads. Alternatively, the minimum-cost network might not correspond to any of these "breakpoints" of the curve, but could lie on a smooth portion as in the single-hour case discussed previously.*

It is important to observe that even in the case where the optimum solution does not correspond to a breakpoint, the engineering does not necessarily reduce to the single-hour ECCS method. To use the single-hour ECCS method, we first compute the "effective alternate-route cost per trunk" as $C_A = C_F + \gamma C_S + C_T$. Then, using a single hour's load, we determine n such that the load on the last trunk during that hour is equal to γ divided by the cost ratio, C_A/C_D . To see how the multihour method differs from this, let us assume that the final group is dominated by its Hour- i load, the switch is dominated by its Hour- j load, and the tandem-completing group is dominated by its Hour- k load. (We make this assumption to avoid having to worry about breakpoints in the cost curve.) Then, it follows from the differentiation of eq. (5) that the optimum value of n satisfies the equation

$$\frac{C_F}{\gamma} L(a_i) + C_S L(a_j) + \frac{C_T}{\gamma} L(a_k) = C_D, \quad (6)$$

* Rather than attempting an exact minimization of eq. (5) in the manner we have described, Rapp adopted an approximate approach. He introduced the fictitious load, \bar{a} , as a function of the parameters a_1, a_2, A_1, A_2 , and then used it in the single-hour formula of eq. (3) to produce a trunk-group size.²

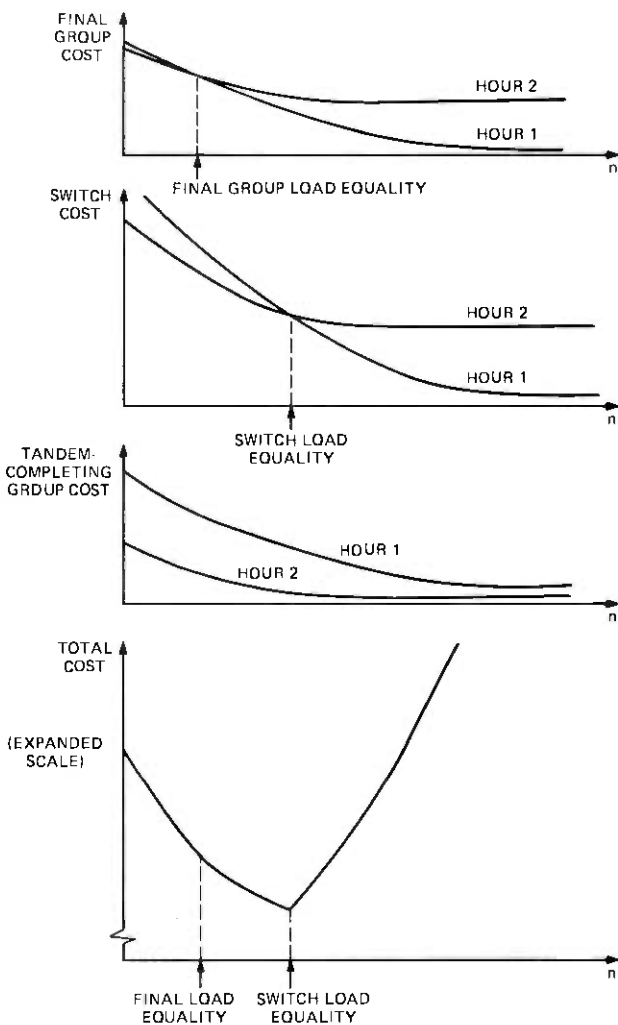


Fig. 7—Multihour trunk-group sizing for the network in Fig. 6.

where a_m ($m = i, j, k$) is the load offered to the high-usage group during Hour m and $L(a_m)$ is the load on the last trunk during that hour.* [This notation omits explicit indication that $L(a_m)$ is a function of n .] If $i = j = k$, so that all components of the alternate route are busy at the same time, then $L(a_i) = L(a_j) = L(a_k) \equiv L(a)$, and we can factor out this quantity. The equation becomes, in this case,

* More precisely, $L(a_m) = -(d/dn)[a_m B(n, a_m)]$.

$$L(a) = \frac{\gamma}{(C_A/C_D)}, \quad (7)$$

where $C_A = C_F + \gamma C_S + C_T$. This is precisely the ECCS formula. [See eq. (3)].

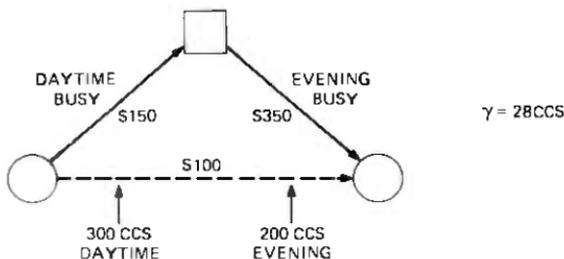
Thus we see, as expected, that the single-hour ECCS method is optimum only when all components of the alternate route have the *same* busy-hour (or when the high-usage load is the same in all hours). If this is not the case, then it is invalid to lump the various components into one alternate-route cost and to choose only a single hour's load for engineering the high-usage group. Equation (6) shows that, in general, the optimal sizing of the group involves the load on the last trunk in each of the three hours that are significant to the alternate route.

An example is given in Fig. 8 which illustrates the difference between multihour and single-hour engineering in the case where the busy hours of the alternate-route legs do not depend upon the high-usage group size. In the example, a single high-usage group with offered loads of 300 CCS in the daytime and 200 CCS in the evening overflows to a final group with a known daytime busy hour and then to a tandem-completing group with a known evening busy hour. (The tandem is neglected for simplicity.) Since the busy hours of the alternate-route legs are fixed, eq. (6) gives the multihour solution for this example. The equation yields a trunk requirement of 11. Single-hour engineering produces a trunk requirement of 13 for the daytime load and 9 for the evening load. It can be seen in the figure that the multihour network cost is significantly lower than both single-hour networks in this example. Note that daytime engineering over-sizes the high-usage group due to an overestimate of the tandem-completing cost, while evening engineering undersizes the group due to an underestimate of the final cost.

IV. THE SIGNIFICANT-HOURS ALGORITHM

An alternative procedure for engineering networks for more than one hour of traffic data, called the "significant-hours" method, has recently come into use in the Bell System. In this section, we describe this algorithm as applied to a two-level local network, and compare it to the multihour method discussed above.

The significant-hours algorithm was devised to overcome shortcomings of the cluster-busy-hour ECCS approach caused by the fact that the various legs of the alternate-route path have busy hours different from that of the originating cluster. These shortcomings can be explained by considering the network in Fig. 9. In the cluster-busy-hour approach, the originating cluster-busy hour of each office is used for sizing all the



MULTIHOURL ENGINEERING

$$150 L(300) + 350 L(200) = 28 \times 100 \quad \Rightarrow \quad n = 11$$

	OVERFLOW	INCREMENTAL COST	TOTAL COST = $11 \times 100 + 150 + 38$ = 1288
DAYTIME	28	$28 \times 150 / 28 = 150$	
EVENING	3	$3 \times 350 / 28 = 38$	

DAYTIME ENGINEERING

$$(150 + 350) L(300) = 28 \times 100 \quad \Rightarrow \quad n = 13$$

	OVERFLOW	INCREMENTAL COST	TOTAL COST = $13 \times 100 + 61 + 12$ = 1373
DAYTIME	11	$11 \times 150 / 28 = 61$	
EVENING	1	$1 \times 350 / 28 = 12$	

EVENING ENGINEERING

$$(150 + 350) L(200) = 28 \times 100 \quad \Rightarrow \quad n = 9$$

	OVERFLOW	INCREMENTAL COST	TOTAL COST = $9 \times 100 + 306 + 142$ = 1348
DAYTIME	57	$57 \times 150 / 28 = 306$	
EVENING	11	$11 \times 350 / 28 = 142$	

Fig. 8—Comparison of engineering methods for fixed alternate-route busy hours.

originating groups in each office. Thus, group A-Z is sized for its A-office cluster-busy-hour load, group B-Z for its B-office cluster-busy-hour load, and group C-Z for its C-office cluster-busy-hour load. If offices A, B, and C are business-dominated offices, the groups A-Z, B-Z, and C-Z would be sized for their daytime business loads. If office Z is a residence-dominated office, however, the loads on these groups may peak in the evening. Since the groups are sized for their smaller daytime loads, they would overflow heavily in the evening, and all this overflow would be offered to the tandem-completing group T-Z. This effect has been observed in actual networks; in some cases, extremely high loads occur on certain tandem-completing groups, requiring great quantities of trunks and switching termination equipment. The problem is clearly caused by the exclusive attention to the originating portion of the alternate-

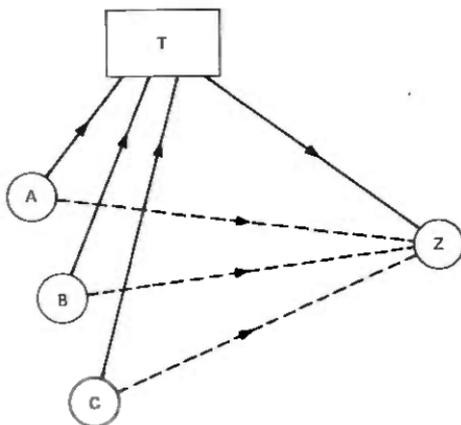


Fig. 9—Example of network.

route path and the total neglect of the terminating portion.

The significant-hours method solves this problem by giving equal treatment to both parts of the alternate-route path. For group A-Z, two significant hours are considered: the A-office originating cluster busy hour (defined above) and the Z-office terminating cluster busy hour (defined as that hour for which the total traffic terminating at office Z is maximum). Of these, the one for which the A-Z load is *larger* is chosen as the "control hour" for group A-Z. The group is then engineered for this load. By engineering the high-usage group for the larger of its significant loads, enough trunks are installed to eliminate the possibility of extremely heavy overflow in the busy hour of the tandem-completing leg.

There still remain two problems with this method, however. The first is the fact that the actual busy hours of the final and tandem-completing groups of the engineered network are not necessarily the same as those that the significant-hour calculation predicts.* The second problem is that even if the significant hours are the right ones, in the sense that the alternate-route busy hours after engineering agree with the original assumptions, this method will over-engineer the group unless either (i) the significant hours are all the same, or (ii) the offered loads on the high-usage group are the same in these hours.

* It should be emphasized that using *observed* final-group and tandem-completing-group busy hours, instead of the originating and terminating *cluster* busy hours, does not get around this problem. The observed busy hours depend on the *previous* network configuration. The point is that if a significant amount of noncoincidence of traffic loads exists, the busy hours of the newly engineered network will not agree with those assumed in the engineering, no matter how the hours are selected.

V. MULTIHOUR ENGINEERING OF A NETWORK

In the discussion of the theory of multihour engineering surrounding eqs. (4) and (5), we considered only the sizing of a single high-usage trunk group in isolation. The background loads on the alternate route were given and assumed fixed. In a network, however, these background loads consist partly of overflows from other high-usage groups—groups which themselves have to be sized during the engineering process. For a network consisting of more than one group, therefore, the use of eq. (5) alone is insufficient, since it does not account for the interdependence between the high-usage groups that arises through their mutual effect on the background loads.

The optimal sizing of a network consisting of N high-usage trunk groups in fact requires the minimization of a cost function of N dimensions, instead of the one-dimensional cost function of eq. (5). An analysis of this optimal approach has been carried out by W. B. Elsner of Bell Laboratories³. All of our initial network results, however, including those described in the remainder of the present paper, were obtained using a simple iterative approach. These initial results allowed us to demonstrate the feasibility of multihour engineering and to quantify the order of magnitude of the associated cost savings. These preliminary findings justified the effort by Elsner to develop the exact algorithm.

We begin the iterative process by choosing initial sizes for every trunk group in the network.* This allows us to compute overflows from each high-usage group and thus to determine the total background loads which are offered to all alternate-route groups. We then size each high-usage group in turn by minimizing its one-dimensional cost function. The background loads used in each case consist of the first-routed loads plus the overflow from all *other* high-usage groups, that is, all high-usage groups except the overflow from the group being sized. After sizing every group once, the background loads that appear on the alternate-route groups differ from what they are at the beginning and, hence, the engineering procedure is iterated, each pass consisting of the resizing of every high-usage group. This process continues until the iteration converges.

An essential aspect of this procedure is the fact that the background loads are updated immediately after the sizing of each group and before the sizing of the next group in sequence. The background loads play a very important part in the process of multihour engineering and it is necessary that the computed background loads be accurate if the proper sizing is to take place. If the updating is not done promptly, the back-

* In obtaining the results that follow, we initialized each group to be numerically equal to the largest load on the group measured in erlangs.

ground loads used in sizing will differ from their true values, and misengineering of the network will result. If the updating is delayed to the end of each complete pass, for example (as was done in our first attempt), the iteration could even fail to converge.

When the iteration does converge, the resulting network has the property that, if all other groups are held fixed, each individual group is sized to minimize cost. It is possible, however, that at convergence network cost could be further reduced by changing the sizes of two or more trunk groups simultaneously. This simple iterative approach also has the property that the solution to which it converges is not unique; depending upon the initial trunk values assumed, and the order in which the groups are sized, the solution network can vary. Both of these undesirable properties of the iterative method are overcome with Elsner's approach.³

VI. COMPUTER PROGRAM AND RESULTS

A computer program incorporating the above iterative multihour procedure was written to design a network with the routing structure shown in Fig. 10. In this network, a single end office has a number of one-way outgoing high-usage trunk groups connected to other end offices. All high-usage groups overflow to a common final group and traffic reaches its terminating office via a one-way tandem-completing group.

The program was run using the load data from three California end offices: Gardena, Compton, and Melrose. In each case, two hours of loads were employed. Hour 1 was a morning busy hour dominated by business traffic, and Hour 2 was an evening busy hour dominated by residential traffic. In the absence of actual trunk and switching cost data, the trunk cost of every group was assumed identical, equal to \$1000 per trunk, and

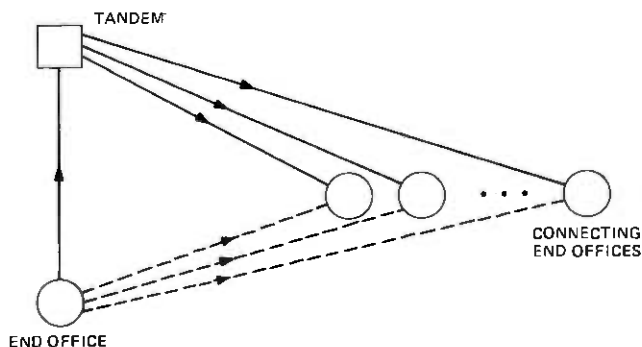


Fig. 10—Network configuration for multihour engineering program.

the switching cost was assumed to be \$62 per CCS (which yields a realistic average switching-to-trunk-cost ratio). Both the switch and the tandem-completing groups were assumed to have zero background load. (This implies that the switch loads are identical to the final loads and that the tandem-completing busy hours are the same as their corresponding high-usage group's busy hours.)

Table I contains detailed results obtained for the Gardena office. The table shows the two hourly offered loads for each high-usage trunk group; it also shows the number of trunks and the resulting hourly overflows for the cluster-busy-hour network and the multihour network.

From the totals at the bottom of the table, it can be seen that the total cluster load in Hour 1 is 6712 CCS while the total cluster load in Hour 2 is 5154 CCS; clearly, Hour 1 is the cluster busy hour. On the other hand, for the network engineered for the cluster busy hour, the total overflow (i.e., the load offered to the final group) is 975 CCS in Hour 2 and only 502 CCS in Hour 1. Here we see again the phenomenon of the final busy hour differing from the cluster busy hour.

The reason for the high side-hour overflow can be seen by looking at the Hour-1 and Hour-2 overflow columns. The overflows in Hour 1 are quite uniform over all trunk groups; the trunk sizes are "matched" to the Hour-1 loads. In Hour 2, however, there is a great mismatch. A few trunk groups have very large overflows, the rest have virtually none. Three groups alone (14, 18, and 20), in fact, account for almost 60 percent of the total overflow in this hour. As can be seen, the pattern of overflow in the multihour network is more nearly balanced between the two hours; the total overflows in Hours 1 and 2 are nearly equal in this network.

Table II compares the main characteristics of the busy-hour and multihour networks for Gardena. The numbers of final trunks shown are sufficient to guarantee a blocking probability of 0.01 for both hours. For the busy-hour network, for example, the final must be sized for the Hour-2 load since that load is larger. The total cost shown is the sum of the costs of the high-usage groups, final group, tandem switching, and tandem-completing groups. (The tandem-completing cost is an approximation based upon the use of marginal capacity to determine the trunk requirement for each group.)

With this simple model, the total cost of the multihour network is approximately 7 percent less than the cost of the single-hour network. Also significant is the fact that the switching cost is reduced 26 percent by using the multihour technique. Table III shows cost comparisons of all three of the networks studied. As can be seen, total network costs for the three cases decrease in the range of 5 to 11 percent and tandem-switching costs decrease in the range of 17 to 26 percent with the use of the multihour technique. (Trunk costs of \$1000 and switching costs of \$62/CCS were assumed in each case.)

Table I — Gardena network results

Trunk Group	Offered Load (CCS)		Cluster-Busy-Hour Engineering			Multihour Engineering		
	Hour 1	Hour 2	Trunks	Hour-1	Hour-2	Trunks	Hour-1	Hour-2
				Overflow (CCS)	Overflow (CCS)		Overflow (CCS)	Overflow (CCS)
1	60	140	3	10	62	4	4	42
2	119	9	6	8	0	3	45	0
3	82	20	4	10	0	4	10	0
4	305	76	12	20	0	6	126	1
5	30	0	2	5	0	0	30	0
6	59	7	3	9	0	1	37	1
7	102	56	5	10	1	4	19	3
8	256	161	11	13	1	8	47	8
9	366	230	15	15	0	12	46	4
10	469	310	18	20	1	18	20	1
11	115	115	5	15	15	5	15	15
12	144	34	7	9	0	7	9	0
13	206	335	9	13	80	10	7	61
14	310	650	13	13	233	16	3	154
15	284	319	12	13	25	12	14	25
16	93	152	4	15	50	5	7	33
17	17	24	1	5	10	1	5	10
18	74	325	4	8	200	6	1	143
19	102	158	5	10	37	5	10	37
20	137	322	6	14	141	8	3	92
21	222	247	9	18	28	10	11	18
22	252	390	11	12	78	12	7	59
23	445	194	17	21	0	17	21	0
24	176	86	8	11	0	8	11	0
25	83	29	4	11	0	4	11	0
26	98	21	5	9	0	5	9	0
27	158	74	7	13	0	7	13	0
28	124	36	6	10	0	6	10	0
29	54	25	3	7	1	3	7	1
30	38	1	2	8	0	2	8	0
31	31	17	2	5	1	2	5	1
32	140	46	6	15	0	6	15	0
33	96	30	5	8	0	5	8	0
34	122	62	6	9	0	6	9	0
35	163	57	7	15	0	7	15	0
36	163	72	7	15	0	7	15	0
37	296	238	12	17	5	12	17	5
38	33	28	2	6	4	2	6	4
39	240	3	10	16	0	10	16	0
40	136	7	6	14	0	6	14	0
41	54	4	3	7	0	3	7	0
42	52	35	3	7	2	3	7	2
43	206	9	9	13	0	9	13	0
Totals	6712	5154	295	502	975	287	713	720

Table II — Main characteristics of busy-hour and multihour networks for Gardena

Network Characteristics	Cluster Busy-Hour Engineering	Multihour Engineering
High-usage trunks	295	287
Final trunks	37	29
Switching cost	\$60,450	\$44,640
Total cost	\$437,106	\$405,315

Table III — Cost comparisons for three networks

Office	Network Total Costs (\$1000)			Tandem Switching Costs (\$1000)		
	Busy-Hour	Multihour	% Decrease	Busy-Hour	Multihour	% Decrease
Gardena	437	405	7	60.4	44.7	26
Compton	493	441	11	87.9	64.7	26
Melrose	303	288	5	45.2	37.6	17

VII. CONTINUING WORK

In this paper, we have described the basic theory of multihour engineering and have demonstrated, in a few simple networks, the potential savings it can bring about. A number of questions require answers for this technique to achieve acceptability for use in the field. These questions include the following: the "hours" of data used for engineering may occur in different seasons of the year as well as different times of the day. How many hours should be included in the engineering of a network and how should these hours be determined? How is multihour engineering to be accomplished in a large-scale network with more than two levels in the hierarchy? How is trunk administration to be carried out in a multihour environment? What changes are required for two-way trunk groups? These questions and others have been the subject of intensive study at Bell Laboratories, and the answers will be reported on in future papers.

VIII. CONCLUSIONS

Multihour engineering is a technique that can provide significant benefits in the design of alternate-route traffic networks. In a computerized engineering environment, especially since automated data-collection methods make it possible to collect larger amounts of (and more accurate) traffic data, this technique should prove to be a realistic and preferable alternative to the older single-hour techniques.

IX. ACKNOWLEDGMENTS

The author would like to express appreciation to the Pacific Telephone and Telegraph Company (PAC) for assistance in providing network data for use in this study. The study was initially motivated by the work of J. W. Price and L. D. Wilson of PAC, who discovered and brought to our attention the existence of heavy side-hour overflows in the Gardena, Compton, and Melrose offices.

REFERENCES

1. C. J. Truitt, "Traffic Engineering Techniques for Determining Trunk Requirements in Alternate Routing Trunk Networks," *B.S.T.J.*, 33, (March 1954), pp. 277-302.
2. Y. A. Rapp, "Planning of Junction Network with Non-coincident Busy-Hours," *Ericsson Techn.*, 27, No. 1 (1971), pp. 3-23.
3. W. B. Elsner, "A Descent Algorithm for the Sizing of Multihour Traffic Networks," (unpublished work).

Design of Quantizers for Real-Time Hadamard-Transform Coding of Pictures

By F. W. MOUNTS, A. N. NETRAVALI, and B. PRASADA

(Manuscript received June 29, 1976)

A methodology is developed to obtain subjectively optimum quantizers for Hadamard-transformed still pictures. To exploit the perceptual redundancies that depend upon the local properties of the picture, a small block ($2 \times 2 \times 2$, horizontal-vertical-temporal) is used. A series of subjective tests was carried out to determine the visibility of impairment in the reconstructed picture when noise, which simulated the quantization noise, was added to the Hadamard coefficients in the transform domain (H -noise). A design procedure for quantizers was developed using these visibility functions. These quantizers minimize the "mean-square subjective distortion" (MMSSD) due to quantization noise. The resulting picture quality and entropy were compared with that of Max-type quantizers which minimize the "mean-square error" (MMSE). This comparison indicates that the MMSSD quantizers based on subjective visibility of the quantization noise are less compressed than the MMSE quantizers. Also for the same number of quantization levels, pictures coded with MMSSD quantizers have better quality and less entropy than the pictures coded with minimum mean-square quantizers.

I. INTRODUCTION

A methodology is developed in this paper to establish fidelity criteria that characterize human observers' perception of noisy transform-coded pictures and to obtain optimum quantizers for the transform coefficients based on these fidelity criteria. The perceptual effects of impairments introduced in the transform domain are, in general, quite different from the impairments introduced in the picture domain. Our experiments, which are performed with the Hadamard transform of a stationary picture, determine the visibility of impairments in the reconstructed picture when noise (H -noise), which simulates the quantization noise, is added to a Hadamard coefficient. Functions that give the appropriate

subjective weighting of the quantization noise as a function of the quantity to be quantized are derived from these experiments. These functions, called visibility functions, are used in a systematic way to design quantizers for PCM and DPCM coding of the transform coefficients. These quantizers are compared with minimum mean-square error (MMSE) quantizers, both in terms of picture quality and bit rates.

1.1 Relationship to previous work

Considerable attention has been paid to the transform domain in the recent work on picture coding.¹⁻¹⁴ Transform domain processing has several potential advantages. It produces less correlated (but not necessarily independent) coefficients. It redistributes the image energy so that a large amount of energy is packed in a few of the coefficients. Moreover, on inverse transformation at the receiver, both noise from quantization of coefficients and the channel errors get distributed over the block in a manner given by the inverse transform of a particular coefficient.

A number of different transforms have been investigated; among them are: Karhunen-Loeve, Fourier, Hadamard, Haar, cosine, and slant transform. There have been several attempts^{5,15,16} to compare the various transforms and to find their relative merits for coding of pictures. Almost all of these comparisons have been with respect to the following three criteria: (i) the correlation between the coefficients, (ii) the mean-square approximation error caused by setting some of the coefficients to zero, and (iii) the computational complexity in obtaining transform coefficients from picture elements (pels) and vice versa. Perceptual factors and the dependence of the picture quality on the particular transform and the block size have not received the attention they deserve.

The irreversible processing of the transform coefficients, which determines the trade-off between picture quality and bit rate, has been performed in a number of ways; for example, (i) zonal sampling or masking, which drops some predetermined higher-order coefficients; (ii) threshold sampling, which drops those coefficients whose values are below a predetermined threshold (a certain amount of addressing information must be sent in using this technique); (iii) quantization of the coefficients—both amplitude (PCM) and differential amplitude (DPCM) quantization^{9,14} have been considered. Most of the work on quantization of the coefficients has centered around minimization of mean-square error as a criterion in designing the quantization characteristics. Several assumptions on the probability of the coefficients have been made, including the familiar gaussian case,¹⁵ to carry out this minimization. Exploitation of the psycho-visual properties of the viewer and the optimization of the quantizers for the best subjective quality of the picture

has often been mentioned in the literature; however, no systematic methods are available for achieving these.

Our work on obtaining the quantization characteristics may be compared with that reported by Landau and Slepian¹ and Tasto and Wintz.⁴ For this reason, we give a brief review of their reports. In both only a single frame of picture data is used despite the fact that the quantization noise is more visible when a sequence of frames of the same scene is coded.

Landau and Slepian considered both Karhunen-Loeve and Hadamard basis vectors for the linear transformation and found that the Karhunen-Loeve transformation required solution of an almost degenerate eigenvalue problem. They then used Hadamard transformation with a 4×4 block. The number of quantization levels given to each of the first ten coefficients was approximately proportional to the variance of that coefficient, and the last six coefficients (H_{11} to H_{16}) were dropped. The first coefficient was quantized by a 64-level uniform quantizer. Coefficients H_2 through H_{10} were quantized with quantizers having a companding characteristic given by a function of the form $y = k\sqrt{x}$.

Two arguments led Landau and Slepian to this quantization strategy. Firstly, since the variances of the lower coefficients are in general larger, coding them more accurately reduced the mean-square error. Secondly, the higher coefficients tend to be large in the busy regions of the pictures, where the viewers have more tolerance to amplitude errors. Thus, they used in an empirical way the consideration of a characteristic of the viewer as well as the statistics in the design of quantizers. They carried out over 100 experiments in which the decision levels and the representative levels of the quantizers were changed. However, since the number of choices is so large, their search could not be exhaustive and, therefore, their quantizers are the best only among those that they investigated.

Tasto and Wintz proposed an encoder using a 6×6 adaptive Karhunen-Loeve transform whose coefficients are quantized by what the authors call a "subjectively" optimized system of quantizers. This is done by first starting with a quantizer that minimizes the mean-square quantization error and then changing it by a trial-and-error procedure to obtain the "best" picture quality in the authors' judgment. The "best" is again from among those encountered in the trial-and-error procedure. They also conducted subjective rating experiments to compare the performance of the minimum mean-square quantizers with the "best" quantizers.

1.2 Basic objectives and approach

Our basic objectives are to obtain fidelity criteria in the transform domain which incorporate psycho-visual properties, and to develop

systematic methods for the optimum design of coders based on these fidelity criteria. As mentioned above, perceptual properties of the human viewer have not been given sufficient importance in the transform-coding literature and, consequently, good models do not exist to explain the subjective effects of the quantization errors in the coefficients when the coefficients are inverse transformed to obtain the picture element (pel).

In the pel domain, some efforts¹⁷⁻¹⁹ have been made to measure properties of human vision in psychophysical experiments and then utilize these to design coders. It is not easy to extend or utilize these techniques for the transform domain where we deal with blocks of pels instead of one pel at a time. Imperfect reproduction of coefficients of the block distributes distortion over the entire block upon inverse transformation.

To take advantage of both the perceptual and statistical properties, some of the factors one has to study are:

- (i) Spread of the quantization error by inverse transformation.
- (ii) Visibility of the quantization error in different coefficients.
- (iii) Statistical decorrelation.
- (iv) Probability distributions of the coefficients.

In this paper, we do not attempt to solve this general problem but restrict ourselves to nonadaptive coding of stationary pictures using a $2 \times 2 \times 2$ (horizontal-vertical-temporal) Hadamard transform. Although a temporal structure of the block is not relevant for still pictures, it will be used in the next phase of our work which will treat coding of a sequence of pictures. The Hadamard transformation has been chosen for its simplicity in implementation. The objective in choosing a small block is to exploit the perceptual redundancies which depend on local properties of the picture. The small block ensures that the quantization noise can be placed in parts of the picture where it is least visible. However, it does result in some loss of coding efficiency on statistical grounds. To compensate at least partially for this, we also discuss the differential coding of the first transform coefficient H_1 .

In Fig. 1 the definition of the Hadamard coefficients for the block size $2 \times 2 \times 2$ is given. H_1 is the sum of the element brightnesses within the block. H_2 is the sum of the line differences within the block. H_3 is the planar difference. H_4 is the sum of the element differences within the block. It may be noted that for stationary pictures, H_5, H_6, H_7 , and H_8 are all zero; further, any noise added to the first four coefficients gets repeated in the reconstructed signal at half the frame rate due to the block structure. As mentioned earlier, in coding frames of a single picture scene, the "nonmoving" noise patterns are, in general, less annoying than the moving noise patterns normally encountered in a television system

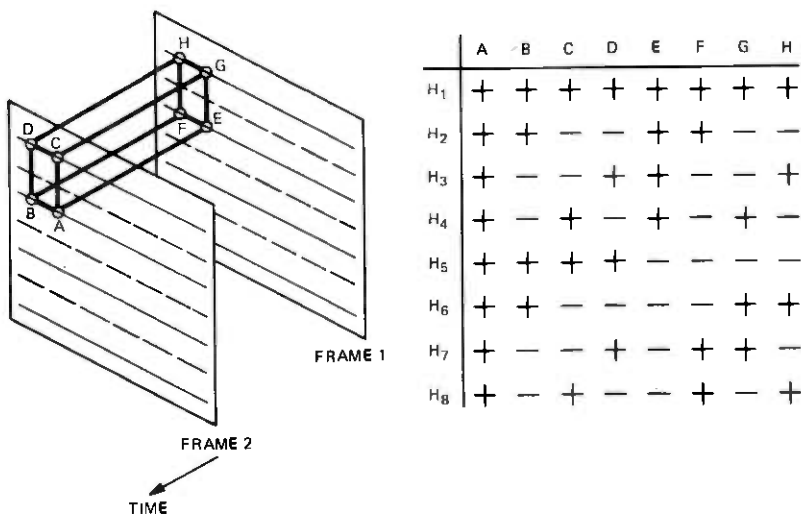


Fig. 1.—Definition of Hadamard coefficients. The pel positions are A, B, C, D, E, F, G, H. The Hadamard coefficients are $H_1, H_2, H_3, H_4, H_5, H_6, H_7, H_8$.

and, for this reason, a system was built to give a more realistic representation of television coding impairment. This system is described in Section II.

Our method for determining the visibility functions of the noise in $H_2, H_3,$ and H_4 consists of the following. We add H -noise (which simulates the quantization noise) to a coefficient whenever its magnitude exceeds a threshold. This is done because each of these coefficients consists of difference quantities of pels and, therefore, may be expected to mask the noise as some function of their amplitude. For the DPCM coding of H_1 , we add H -noise whenever the magnitude of the difference of H_1 from its previous block value is higher than a threshold. Again, this difference of H_1 can be taken as a measure of signal busyness. The effect of this H -noise impairment on the picture is then compared by the subject in an $A-B$ test with simple additive white noise impairment of the picture. This method of judging pictures is similar to the one used by Candy and Bosworth.²⁰ The experimental method is discussed in detail in Section II.

1.3 Summary of results

The visibility functions for the following conditions have been measured: H_2 -noise as a function of $|H_2|$; H_3 -noise as a function of $|H_3|$; H_4 -noise as a function of $|H_4|$; and H_1 -noise as a function of $|\Delta H_1|$, where ΔH_1 is the adjacent block difference in the horizontal direction.

The study of these visibility functions indicates that H_3 is the least

important coefficient and can be dropped entirely with little impairment. PCM quantizers with minimum mean-square subjective distortion (MMSSD) have been designed for H_2 and H_4 coefficients, and an MMSSD DPCM quantizer has been designed for H_1 using the corresponding visibility functions as the fidelity criteria. These quantizers have been implemented and have been compared in subjective tests with the corresponding quantizers optimized with respect to the minimum mean-square error criteria. Details of this approach and the results are given in the subsequent sections.

II. EXPERIMENTAL SYSTEM

The experimental system described in this section has been designed with considerable flexibility as a vehicle for future research. The system has real-time capabilities for adaptive and nonadaptive Hadamard transform coding of a $2 \times 2 \times 2$ block of pels.

2.1 System block diagram

A block diagram of the experimental system is shown in Fig. 2. The video signal is generated by a vidicon camera scanned with 271 lines interlaced 2:1. The video signal has a bandwidth of 1 MHz and is sampled at the Nyquist rate. Each picture sample is PCM encoded with amplitude accuracy of 8 bits per pel.

A frame memory is incorporated in the system to accommodate the transform block. Alternate frames of the digitized pictures, say the odd frames, are stored in the frame memory via data select switch 1. Memory 1 consists of two line delays and four small delays for linking the data from the present and previous frames. It ensures, during even frames, simultaneous presentation of all the elements from the two frames that comprise the data block to the Hadamard transform logic. It may be noted that the system is designed for spatially overlapped block processing. The output corresponding to nonoverlapping blocks is selected by memory 2 for decoding and experimentation. The spatially overlapping blocks are suitable for the study of various kinds of predictive encoders. This facility is also very useful for a flicker-free display of the Hadamard coefficients on a television screen.

The Hadamard transform circuit is a serial and parallel combination of adders and subtractors to implement the canonic forms shown in Fig. 1. In the processor circuit, the magnitudes of all the coefficients are rounded off to the eight most significant bits, which are used for further processing. This rounding off does not produce any visible impairment on inverse transformation. Capabilities exist in the processor circuit to insert eight independent quantizers, one for each coefficient.

For the subjective experiments, the processor circuit permits two

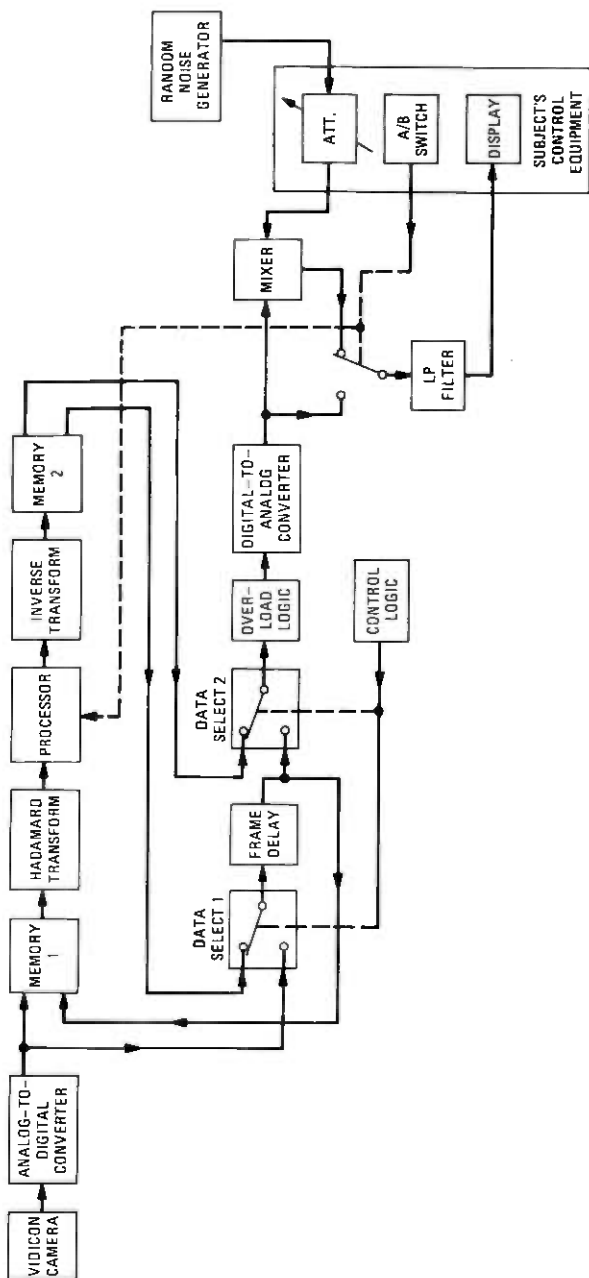


Fig. 2.—System block diagram.

modes of operation controlled by the A/B switch. The details of the subsystem are shown in Fig. 3. The A/B switch is under the control of the subject. In the A mode, unimpaired coefficients are fed to the inverse-transform circuit. This provides the original picture in the reconstructed signal domain. In the B mode, a controlled amount of pseudo-random noise is added to one of the coefficients only when the magnitude of a control signal (which is the coefficient itself in this diagram) exceeds some reference threshold. This noise, which we call the *H*-noise, is generated at the sample rate by an 8-bit pseudo-random generator having a period of 2^{15} words and which is not synchronized with the line or the frame rate of the picture. An amplitude limiter controls the magnitude of the noise to the level set by the experimenter. The sign bit for the noise word is obtained from the output of a white noise source, and has equal probability of being a "0" or a "1".

Since the addition of pseudo-random noise results in doubling of the maximum amplitude of the noisy coefficient, the sum of the coefficient and noise, and the other coefficients, are divided by 2 prior to inverse transformation to prevent overload.

The inverse transformation network is similar to the transformation network and is used to reconstruct simultaneously all of the pels of the block.

It may be recalled that the alternate frames (odd frames) of the input are stored in the frame memory via data select switch 1. The recon-

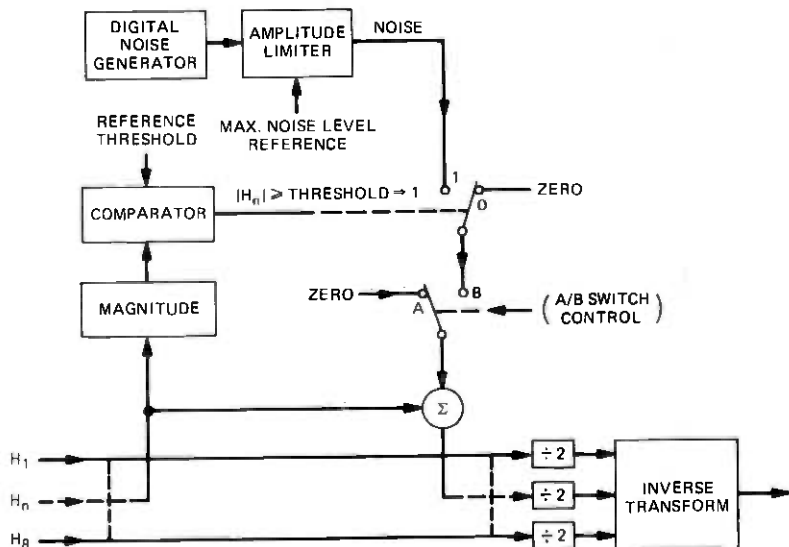


Fig. 3—Noise adding circuits. Coefficients are divided by 2 to prevent overload in the inverse transform function after noise addition.

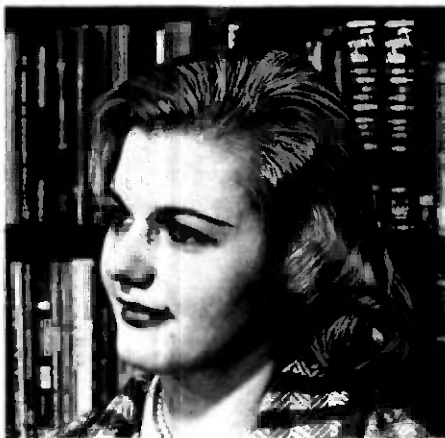


Fig. 4—Original picture used for subjective tests.

structed pels corresponding to the even frames are stored in the proper time slots in the frame memory by data select switch 1. Thus, the frame memory contains both processed and unprocessed data and is utilized fully. Data select switch 2 ensures that the reconstructed pels corresponding to the even frames that are stored in the frame memory are fed to the digital-to-analog converter in the proper time sequence.

The original picture used for the subjective tests is shown in Fig. 4. The scanned and filtered version (by a 1-MHz *Picturephone*[®] filter) is shown in Fig. 5a. Figure 6 shows the picture of the coefficients using overlapping blocks. Figure 6a shows coefficient H_1 , which is essentially a “block-low-pass-filtered” version of the picture and preserves much of the picture information. On the other hand, Figs. 6b (H_2 coefficient), 6c (H_3 coefficient), and 6d (H_4 coefficient) show a variety of edge information.

2.2 Experimental details

The experimental setup for determining a visibility function is shown in the simplified block diagram in Fig. 7. The experimenter adds H -noise to a selected coefficient whenever the absolute value of the coefficient exceeds a threshold. The amount of noise and the threshold are varied. This is presented as condition B to the subject. Condition A is the unimpaired picture plus white noise. By turning an attenuator knob, the subject can control the amount of white noise added to the unimpaired picture. He can switch between conditions A and B by the A/B switch provided. An experiment consists of the subject changing the attenuator until he finds the pictures in the switch positions A and B to be subjec-



(a)



(b)



(c)



(d)

Fig. 5—Filtered test picture and H -noise added pictures. (a) Filtered test picture (1-MHz *Picturephone*® filter). (b) Picture with noise added to H_1 . (c) Picture with noise added to H_2 . (d) Picture with noise added to H_4 .

tively equivalent. The subject can switch between A and B conditions as often as he likes and can look at the test conditions as long as he likes. When he arrives at the subjective equivalence, he gives the attenuator reading to the experimenters on an intercom. He is then given the next test condition. In one sitting, a subject makes 28 judgments of which the first four are considered as training. The remaining 24 are recorded as data. The experiment is also characterized by the following:

- (i) The picture has 271 lines, interlaced 2:1 at 30 frames per second.
- (ii) The visible portion of the picture is about 13 cm \times 12 cm.
- (iii) High light brightness is 74 foot-lamberts.
- (iv) Low light brightness is 4 foot-lamberts.
- (v) Room illumination is 57 foot-candles.

The scan lines of the Conrac monitor were broadened to correspond to the *Picturephone* display tube. Subjects were seated at a distance of



(a)



(b)



(c)



(d)

Fig. 6—Pictures of coefficients. (a) Picture of H_1 coefficient (with no output filter). (b) Picture of H_2 coefficient (with output filter). (c) Picture of H_3 coefficient (with output filter). (d) Picture of H_4 coefficient (with output filter).

about 80 cm from the monitor. All of the six subjects used had experience in judging coded television pictures.

III. TEST DATA AND ANALYSIS

Results of a typical subjective test are shown in Fig. 8. In this case, the absolute value of H_4 was compared to a threshold and the noise (H -noise) was added to H_4 . In this figure, H_4 -noise is plotted in dB on the X -axis and the "equivalent white noise" is plotted on the Y -axis. Each datapoint is an average of the readings obtained from six subjects. Under the assumption that the equivalent white noise (V_W) is proportional to the H -noise (V_H), the results for each threshold should fall on a 45-degree straight line. The lines drawn in Fig. 8 are the best unity-slope straight lines obtained by the least square fitting to the datapoints. Figures 9 and 10 show similar data for H_2 , and H_1 , respectively. In the case of H_1 , $|\Delta H_1|$ is compared to a threshold. Notice that in each case the quantity that

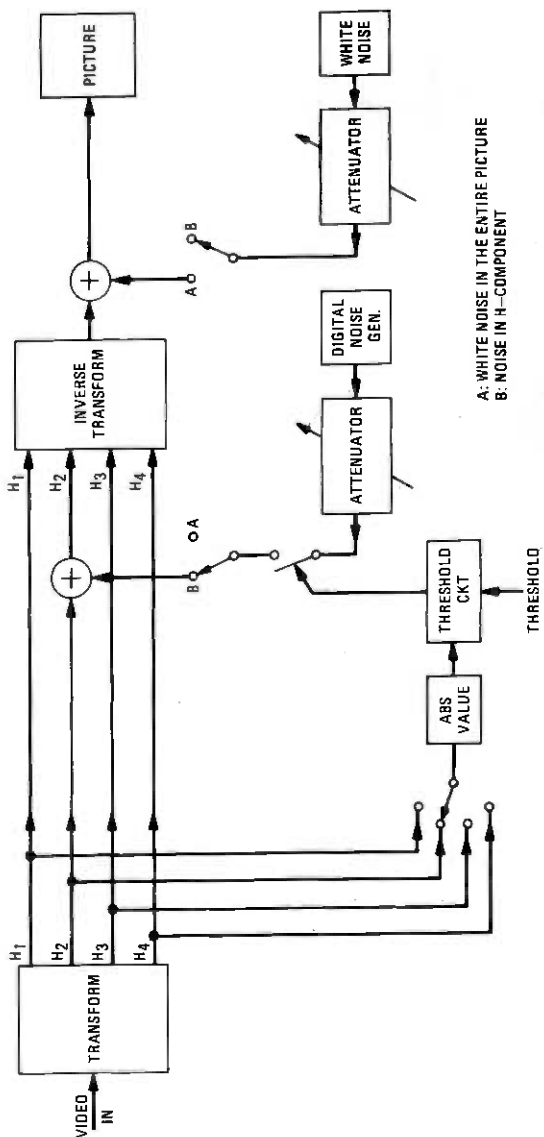


Fig. 7—Experimental setup. Noise is added to H_2 coefficient as a function of its magnitude.

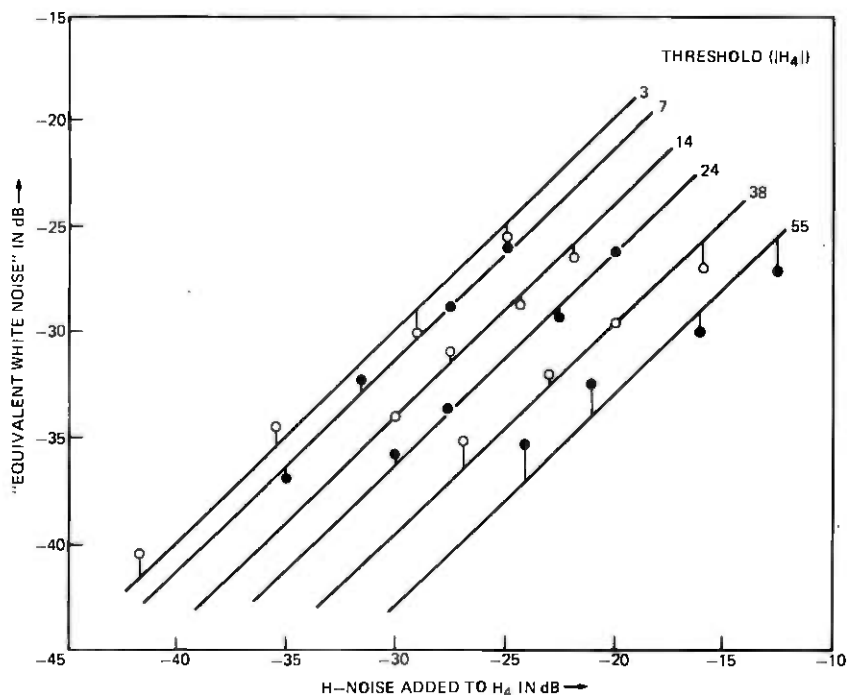


Fig. 8—Plot of "equivalent white noise" vs H_4 noise for different thresholds on $|H_4|$.

is compared to a threshold is a measure of busyness of the picture in a local area. The locations in the picture where noise is added and its appearance are dependent upon the quantity that is compared to a threshold and the coefficient to which the noise is added.

The pictures with H -noise impairments are shown in Fig. 5. The H -noise added in each of the three pictures has a peak value of 100 units* (signal range is 0 to 255 units). In Fig. 5c, noise is added to H_2 in all blocks which have $|H_2|$ more than five units, whereas in Fig. 5d, noise is added to all blocks in which $|H_4|$ is more than five units. While H_2 is the line difference, Fig. 5c has noise whenever an edge has a sufficiently large component along the horizontal direction, whereas Fig. 5d has noise whenever an edge has a sufficiently large component along the vertical direction. Also notice the difference in the appearance of the noise. H_2 -noise is much more noticeable than H_4 -noise. Figure 5b shows noise

* This is much more than the noise used for any test condition, but has been used to demonstrate the effects in a photograph.

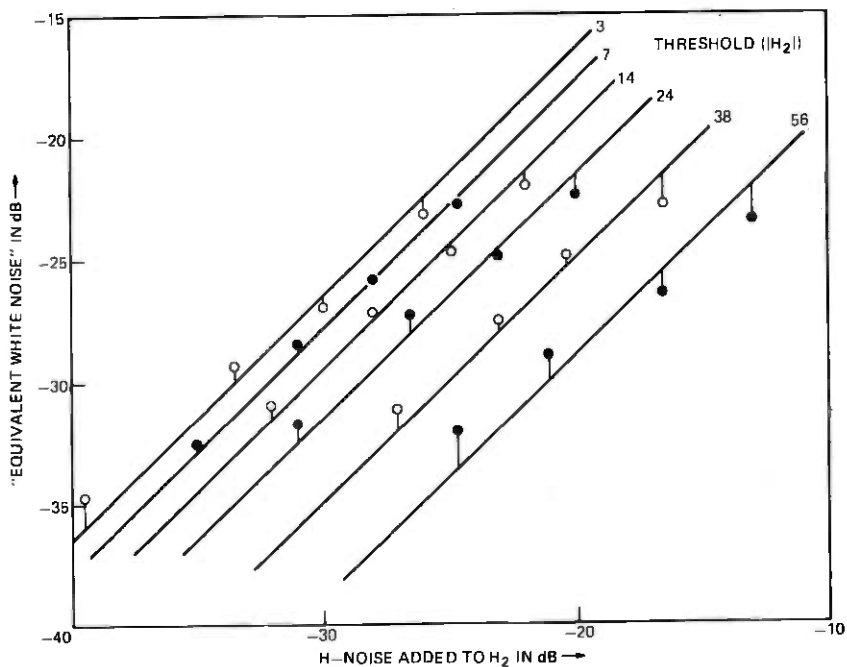


Fig. 9—Plot of "equivalent white noise" vs H_2 noise for different thresholds on $|H_2|$.

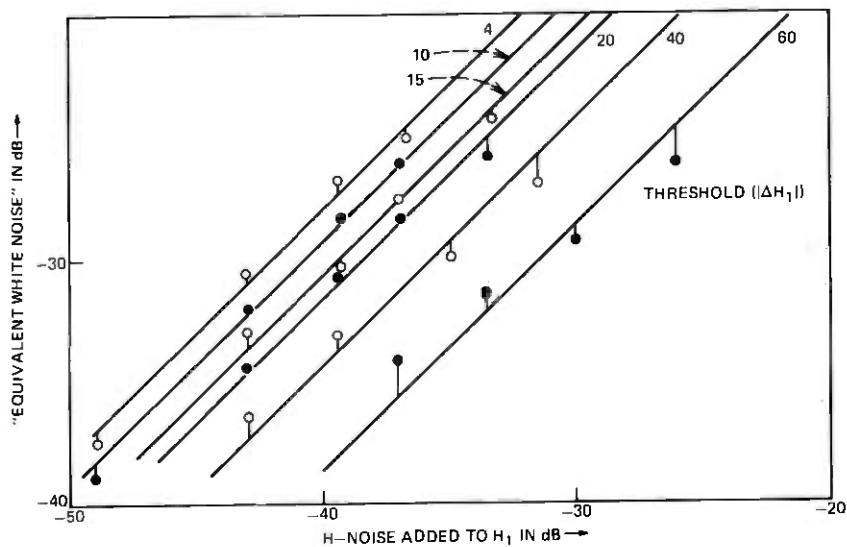


Fig. 10—Plot of "equivalent white noise" vs H_1 noise for different thresholds on $|\Delta H_1|$.

of 100 units added to H_1 whenever $|\Delta H_1|$ is more than 10 units. Here again, noise gets added to all blocks having horizontal interblock edges. Also the pattern generated by H_1 noise is much more objectionable than the pattern generated either by H_2 -noise or H_4 -noise.

The relationship of proportionality between the equivalent white noise and the H -noise for a threshold z is written in the form:

$$V_w = F(z)V_H, \quad (1)$$

where z can take on the value of $|H_2|$, $|H_3|$, $|H_4|$, or $|\Delta H_1|$. The constant of proportionality $F(z)$ is the equivalent white noise power when a unit H -noise is added to the particular coefficient for all blocks of the picture, where the magnitude of the corresponding coefficient ($|\Delta H_1|$ in the case of H_1) is greater than or equal to the threshold z . We next assume the additivity of the equivalent white noise power with respect to the coefficient value; i.e., if the equivalent white noise power when a unit of H -noise is added to H_2 and $T_1 \leq |H_2| < T_2$ is V_{w1} , and the equivalent white noise power when a unit of H -noise is added to H_2 and $T_2 \leq |H_2| < T_3$ ($T_1 < T_2 < T_3$) is V_{w2} , then the equivalent white noise power when a unit of H -noise is added to H_2 and $T_1 \leq |H_2| < T_3$ is $(V_{w1} + V_{w2})$. Under this assumption, $F(z)$ can be written as an elemental sum of the equivalent white noise powers. Thus,

$$F(z) = \int_z^{\infty} f(x)dx, \quad (2)$$

where $f(z)$ is called the visibility function.

Using this procedure, visibility functions were computed. They are shown in Fig. 11. Notice that we have assumed that the occurrences of positive and negative coefficients ($\Delta H_1, H_2, H_3, H_4$) are similar, and the noise visibility does not depend upon the sign of the coefficient. This results in the visibility functions being symmetrical about zero. The value of the visibility function shows the relative importance of the various transform coefficients. The larger the value, the more important is the coefficient. In general, the visibility functions decrease as a function of their arguments. This is a combined effect of several factors, such as (i) the decrease in the number of blocks having large coefficient values ($|\Delta H_1|$ in the case of H_1), (ii) the dependence of the perception of noise on the magnitudes of the coefficients (which correspond to the sharpness of the boundary in the pel domain), and (iii) the contextual importance of the specific regions of the picture.

Psycho-visual techniques which measure the detectability of perturbations in the neighborhood of edges,^{18,21-23} and the just noticeable differences in the amplitudes of edges have been widely applied to DPCM coding. Since these deal with over-simplified stimuli and surround and are almost always detection experiments, their use in picture coding may

not always result in better coders. In any case, these techniques cannot be easily applied in the transform domain because we are not dealing with the single pels but with blocks comprising pels from more than a single line and frame. Also, the perturbations must be introduced in the transform coefficient, whereas the annoyance to the perturbations must be judged in the pel domain.

Our approach, which obtains the visibility functions as outlined above, has the following limitations:

(i) Since the visibility functions are tied to the picture content, they admittedly vary from picture to picture, especially if the picture content is changed significantly. They also depend upon the class of viewers and the viewing conditions. Thus, any optimization based on the visibility functions is strictly applicable to a restricted situation. This is under-

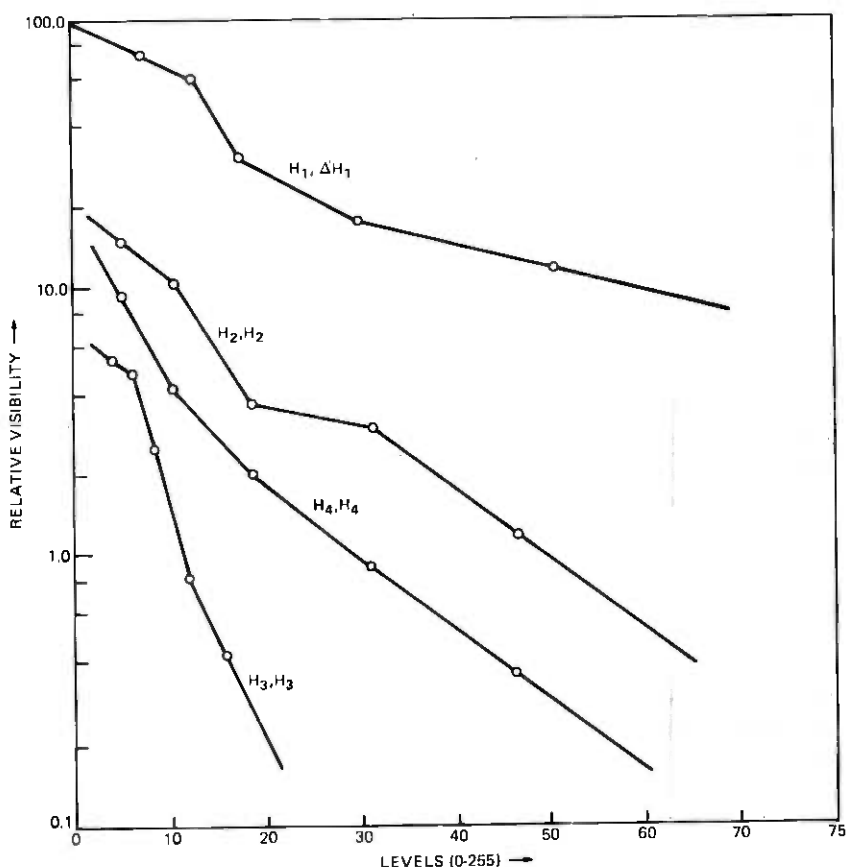


Fig. 11—Plot of visibility functions. Notation H_i, H_j indicates noise added to H_i , when H_j is thresholded. The H_j threshold level is shown on the X-axis.

standable since the human perception does indeed vary with the picture content, the viewing conditions, and the particular viewer. We demonstrate in Section IV that the results we obtained using these visibility functions are not overly sensitive to the picture content and are reasonable for a class of pictures rather than a particular picture.

(ii) The simulation of the quantization noise by the H -noise is fairly accurate for H_2 , H_3 , and H_4 . However, in the case of H_1 , DPCM techniques are used to code ΔH_1 . The changes in the appearance of noise as a function of threshold are not completely reflected in the measurements; i.e., while the noise that is added to H_1 does look like granular noise at low thresholds, it does not look like slope overload at high thresholds. Also, at high thresholds, the noise is added to fewer blocks in the picture and the appearance of such an impaired picture is different from the appearance of a white noise impaired picture. Therefore, in some cases subjective equivalence is hard to achieve.

(iii) It would be better if the perceptual, statistical, and contextual effects were explicit in the visibility function and could be controlled separately. Unfortunately, such is not the case.

(iv) It is seen from eq. (2) that the process of obtaining the visibility function involves differentiation of the data, which is known to introduce some noise. By adding H -noise to a coefficient when the quantity to be compared to a threshold is within a small range of values, it is possible to avoid this differentiation.

IV. RESULTS

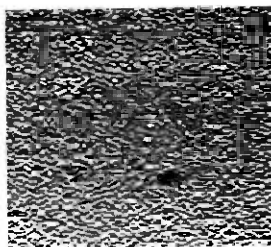
In this section, we present certain conclusions drawn from the visibility functions and then describe their application to the design of quantizers for the coefficients. Visibility functions shown in Fig. 11 clearly show the relative importance of various coefficients. H_1 is the most important, H_2 is the next, followed by H_4 , and H_3 is the least important. The visibility of H noise depends upon the patterns associated with a particular coefficient. These patterns depend upon the inverse transform and are shown in Fig. 12 for H_2 , H_3 , and H_4 , respectively. In each case, noise of a given amount is added to one of the coefficients, and the background is assumed to be flat. The higher the spatial frequency of the pattern, the lower the visibility of the noise. Thus, H_2 noise is more visible than H_4 noise because the interlace gives the H_2 noise pattern lower spatial frequency than the H_4 noise pattern.

4.1 Visibility of H_1 noise

An experiment was performed to utilize the well-known property of the human eye that the brightness discrimination decreases as the brightness level increases, called Weber's law in the psycho-visual lit-



(a)



(b)



(c)



(d)

Fig. 12—Pictures of noise patterns for coefficients. (a) Picture of noise added to H_1 on a flat background. (b) Picture of noise added to H_2 on a flat background. (c) Picture of noise added to H_3 on a flat background. (d) Picture of noise added to H_4 on a flat background.

erature²⁴⁻²⁶ (see Ref. 27 for a recent application of Weber's law for picture coding in the pel domain).

In this experiment, noise was added to H_1 as a function of H_1 , since H_1 corresponds to the average brightness in the block. The results of this subjective experiment showed large variations from observer to observer. When the data for the observers was averaged, there was no significant variation in the visibility of noise as a function of H_1 . This could be due to the following: (i) If the gamma of the display tube used was not unity, it would have partially compensated for Weber's law effects. (ii) We were working with the head and shoulders view of a person. In general, for such a picture, the highlights are on the forehead or the cheek of the person. These regions are contextually very important causing the visibility of noise to be high. (iii) The picture we used was such that the low-light areas had more spatial detail than the highlight areas; thus, the latter two effects may have compensated for the Weber's law.

Measurements of the gamma of the monitor indicate that the visibility function in this case cannot be fully explained on the basis of the compensation of Weber's law by the gamma of the display tube. It seems that at least for this class of pictures, namely the head and shoulders view of a person, the advantage that could be gained by the utilization of Weber's law is compensated for by the other effects.

4.2 "Frozen" vs "unfrozen" noise visibility

It may be recalled that the experiment on visibility was done using a block size of $2 \times 2 \times 2$. In this case, any noise added to the first four coefficients remained unchanged for two frames. The noise in the coefficients in this case may be called the "frozen" noise because it remains unchanged for two frame periods. An experiment was performed to determine the visibility functions for H_4 coefficient for a block size of 2×2 (horizontal-vertical). Since all the experiments have been carried out with a stationary picture, the only difference between the experiment with the block size of 2×2 and a block size of $2 \times 2 \times 2$ is the coefficient noise. For the block size of 2×2 , the coefficient noise changes from frame to frame and is called "unfrozen" noise. Figure 13 shows the visibility functions for H_4 with "frozen" and "unfrozen" noises. Although the visibility functions of "unfrozen" noise are generally a little lower than that of "frozen" noise, due to lower temporal frequency, the differences are small.

In Section III, it was mentioned that the visibility functions can be used as fidelity criteria for the design of quantizers. We describe below how these results are used to design quantizers.

4.3 PCM coding of H_2 , H_3 , and H_4

It is assumed that little interaction exists between the Hadamard coefficients, so that the quantization transfer characteristics for the coefficients can be obtained independent of each other. It is recalled from Fig. 11 that H_3 was the least important coefficient and, therefore, it was decided to drop the transmission of H_3 altogether.

Minimum mean-square error quantizers are obtained by minimizing the mean-squared quantization error. If N is the number of levels, and $P_{H_k}(\cdot)$ is the histogram for $|H_k|$, then we minimize the distortion D given by

$$D = \sum_{j=1}^N \int_{X_j}^{X_{j+1}} (|H_k| - Y_j)^2 P_{H_k}(|H_k|) d(|H_k|), \quad k = 2, 3, 4, \quad (3)$$

with respect to $\{X_j\}$, $j = 2, \dots, N$ and $\{Y_j\}$, $j = 1, \dots, N$. This gives us the well-known Max quantizer.²⁸ MMSE quantizers are obtained by weighting the quantization error according to the frequency of its oc-

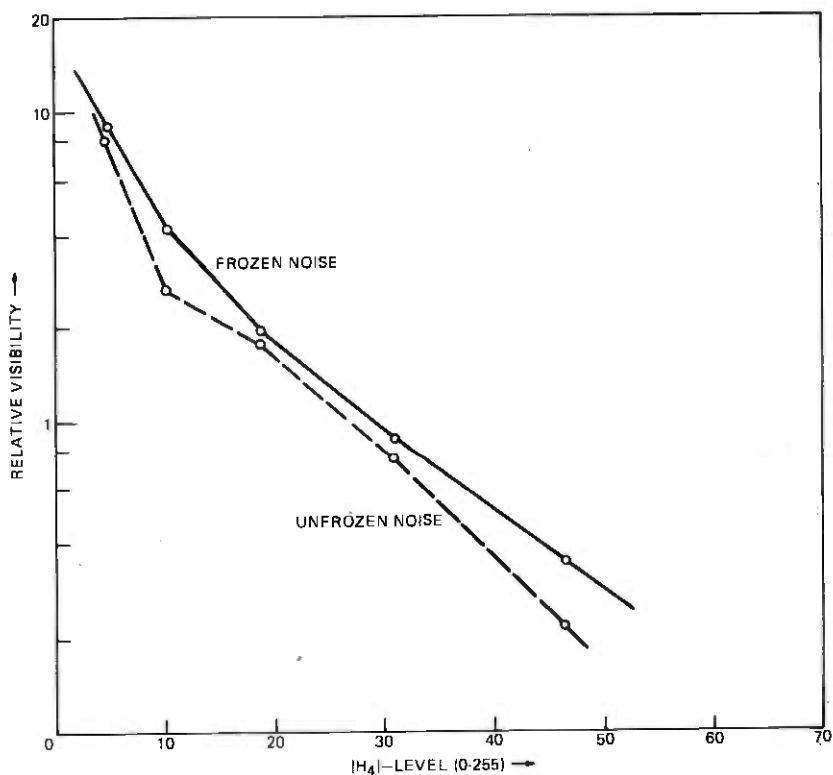


Fig. 13—Visibility function for “frozen” and “unfrozen” H_4 noise.

currence. Minimum mean-square subjective distortion quantizers, on the other hand, weight the quantization error according to its subjective visibility. This can be achieved by substituting $f_{H_k}(\cdot)$ for $P_{H_k}(\cdot)$ in the expression for the distortion. The term $f_{H_k}(\cdot)$ is the visibility function for the coefficient H_k . Standard programming techniques were used to minimize the distortion D in both cases.

The histograms for $|\Delta H_1|$, $|H_2|$, $|H_3|$, and $|H_4|$ are shown in Fig. 14. In general, these decrease faster than the visibility functions. This is exemplified in Fig. 15 in which the histogram and the visibility function for ΔH_1 are plotted with the same scale on the X-axis. We shall see later that this fact results in larger companding of the MMSE quantizers than the MMSSD quantizers and, consequently, poor reproduction of busy areas of a picture.

Typical quantizer characteristics are shown in Fig. 16. The MMSE quantizer is more companded than the MMSD quantizer. Note also that the dynamic range of the MMSE quantizer is smaller. The performance

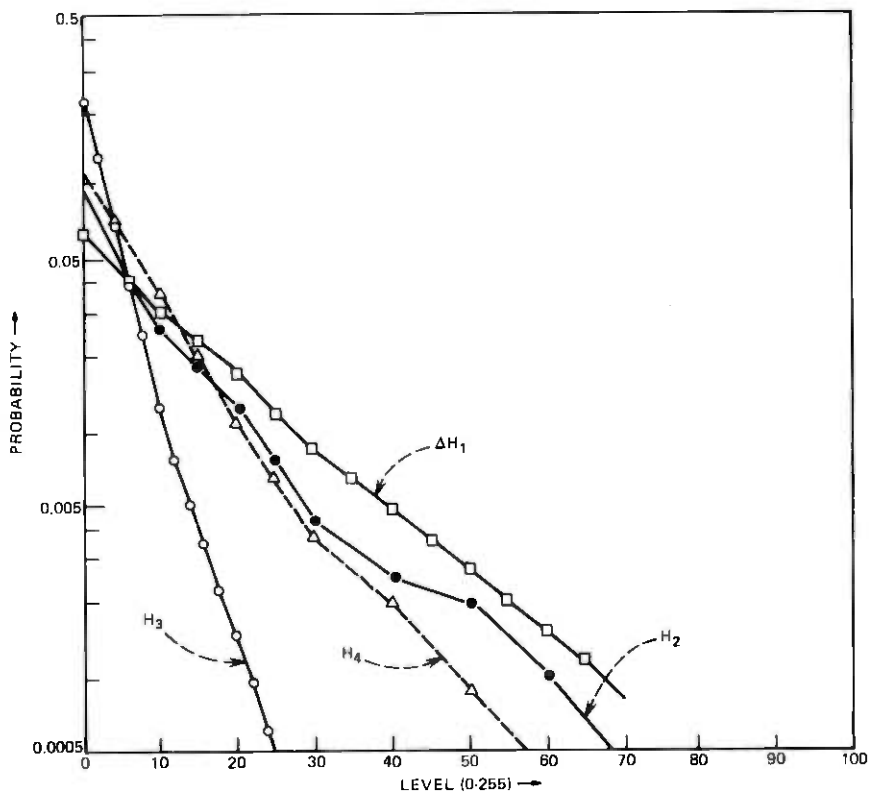


Fig. 14—Histograms of coefficients. All the histograms are assumed to be symmetric about zero.

of these two types of quantizers (MMSSD and MMSE) was compared in an A-B test with different numbers of levels. Figure 17 shows the results of such a test for the coefficient H_4 . In this test, MMSE quantizers with levels 5 to 8 were compared in terms of picture quality with MMSSD quantizers with levels 3 to 9 using a random pairing by six skilled subjects. The numbers in the table indicate the percentage of observers who preferred the MMSSD quantizers over the MMSE quantizers. The picture coded with the 5-level MMSSD quantizers was preferred by 100 percent of the subjects over the 6-level MMSE quantizer. Figure 18 shows similar comparisons for the quantization of H_2 . Here again, for the same number of levels, the picture quality using the MMSSD quantizers is always better than using MMSE quantizers. Moreover, picture quality using the 6-level MMSSD quantizer and 7-level MMSE quantizer is equivalent. Figures 19 and 20 show the entropy of the quantized output using both the MMSSD and the MMSE quantizers having levels 3 to 8 for H_4 and H_2 , respectively. In the case of H_4 , the difference between the entropies of

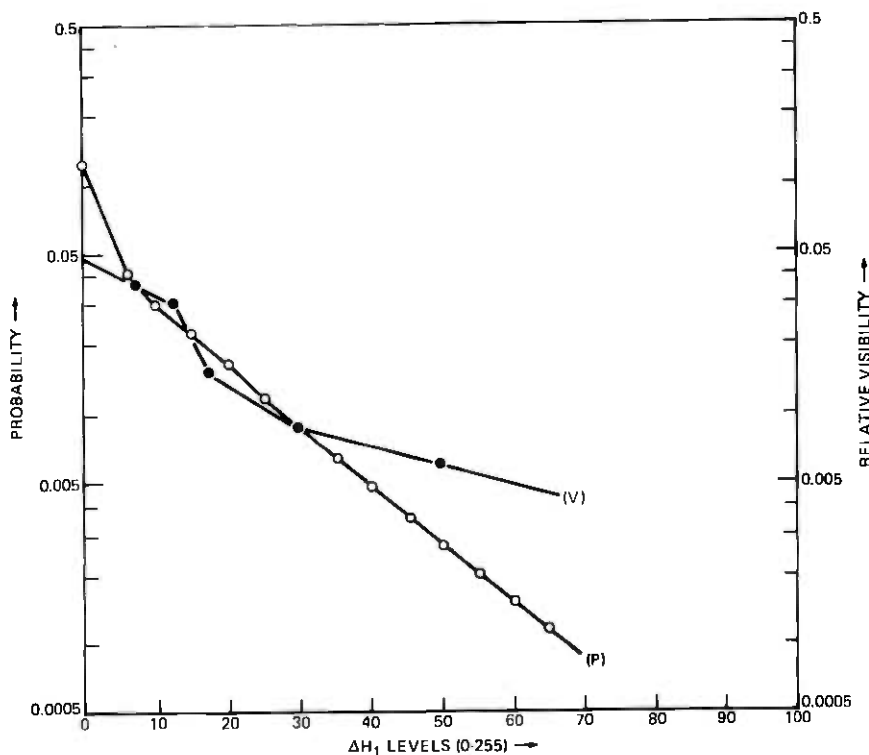
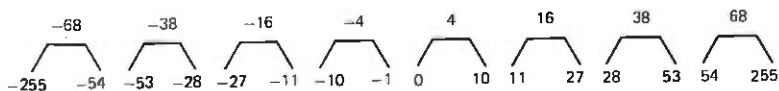


Fig. 15—Comparison of probability density (P) and visibility (V) for H_1 noise.

the output of the MMSE and the MMSSD quantizer for the same number of levels is about 0.2 bit. Since the picture quality with the 7-level visibility quantizer was better than with the 8-level MMSE quantizer, the gain by the use of the MMSSD quantizer is of the order of 0.5 to 0.6 bit for the transmission of H_4 . Similar remarks can be made about the quantization of H_2 .

MMSSD QUANTIZER (8 LEVELS)



MMSE QUANTIZER (8 LEVELS)

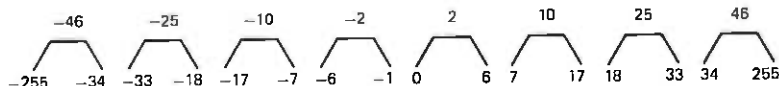


Fig. 16—Typical (MMSSD and MMSE) quantizer characteristics for H_4 coefficient. Notation $\begin{matrix} z \\ x \ y \end{matrix}$ implies that all input levels between x and y (including x,y) are represented as z .

		MMSSD QUANTIZERS							
		Number of Levels							
		3	4	5	6	7	8	9	
MMSE QUANTIZERS	Number of Levels	5	50	33	83	100	100	100	100
	6	50	33	100	100	100	100	100	
	7	33	33	33	87	100	100	100	
	8	17	17	50	33	100	100	100	

Fig. 17—Comparison of picture quality of MMSSD and MMSE quantizers of different levels for H_4 .

4.4 Coding of H_1

Unlike the H_2 , H_3 , and H_4 coefficients, the H_1 coefficient is not a difference signal. It represents the average brightness within the block and thus carries the low-frequency information which should be coded relatively precisely. Uniform PCM coding of H_1 requires 7 to 8 bits for good picture quality. As mentioned before, efforts to compand the PCM quantizer by using the Weber's law effect were not very successful. Therefore, it was decided to DPCM encode H_1 . Since the block size used is small, there is substantial correlation between the H_1 values of adjacent blocks. This was exploited by using a DPCM coding of H_1 with horizontally adjacent blocks for prediction. The quantizers for such a DPCM coder are obtained from the visibility function of H_1 under the control of $|\Delta H_1|$ in a manner similar to the above by minimizing the mean-square subjective distortion due to the quantization noise. The resulting quantizer scales are companded due to the monotonic decrease of the visibility function with respect to ΔH_1 , as shown in Fig. 11. Quantizer scales have also been obtained by minimizing the mean-square quantization error.* As noted before, MMSE quantizer scales are more companded and have less dynamic range compared to the MMSSD quantized scales. Using these two types of scales, experiments have been performed

* Although the visibility function and the histograms are obtained from the difference signal $|\Delta H_1|$, and the quantity that is quantized is the differential signal (i.e., the difference between the present H_1 and the coded value of H_1 from the previous block), it is expected that the quantizer characteristics will not change appreciably by using difference instead of the differential signal in eq. (3).

MMSE QUANTIZERS		MMSSD QUANTIZERS						
		Number of Levels						
		3	4	5	6	7	8	9
Number of Levels	5	0	17	100	100	100	100	100
	6	0	0	0	100	100	100	87
	7	0	0	0	50	100	100	100
	8	0	17	0	17	33	100	87

Fig. 18—Comparison of picture quality of MMSSD and MMSE quantizers of different levels for H_2 .

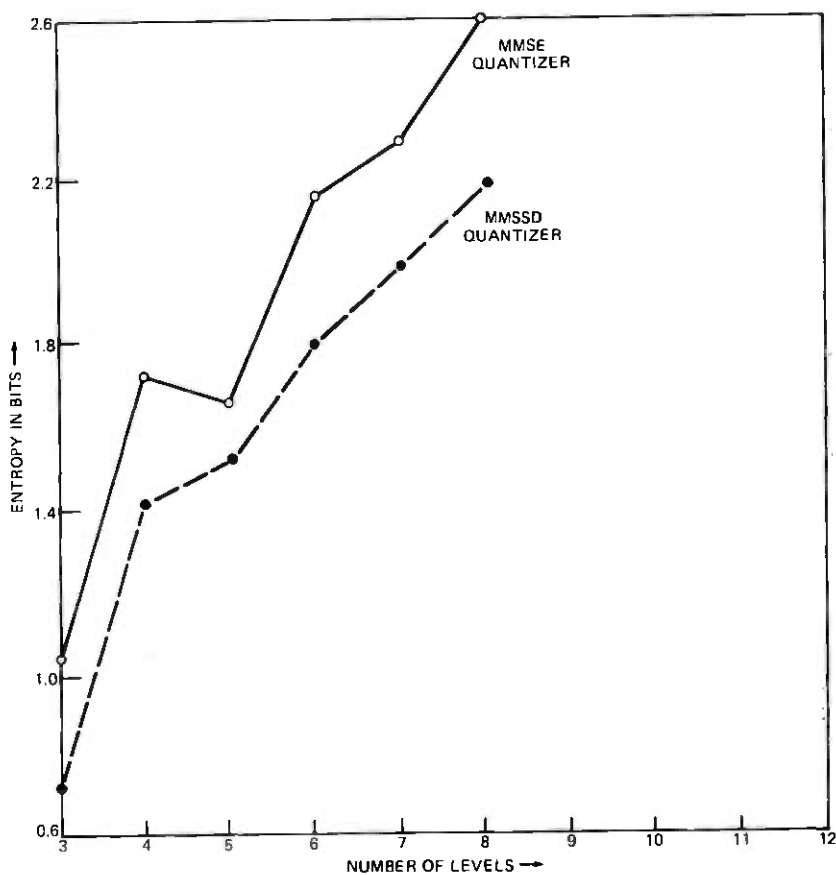


Fig. 19—Plots of entropy of outputs of MMSSD and MMSE quantizers of different levels for H_4 .

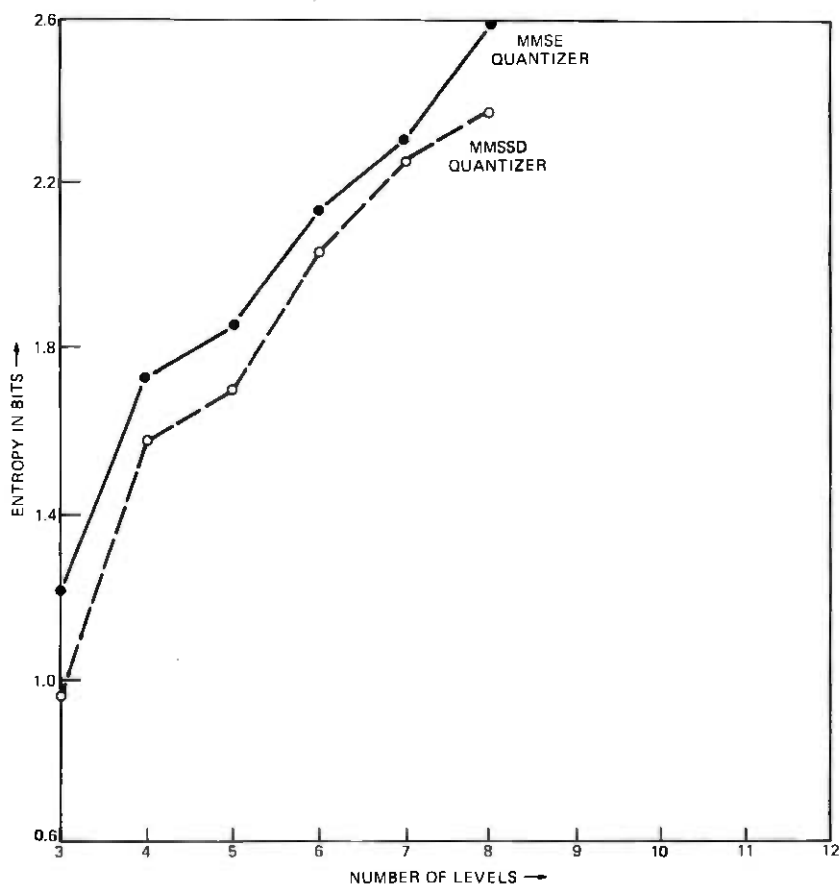


Fig. 20—Plots of entropy of outputs of MMSSD and MMSE quantizers of different levels for H_2 .

to compare the picture quality for the same number of levels. The results of such a comparison are shown in Fig. 21. It is seen that, for the same number of levels, all the subjects preferred the picture coded with the MMSSD quantizers over the picture coded with MMSE quantizers. Moreover, picture quality using a 24-level MMSSD quantizer is equivalent to the picture quality using a 30-level MMSE quantizer. Entropies of the quantized signal with MMSSD and MMSE quantizers of different levels are shown in Fig. 22. Here again, visibility quantizers perform better than MMSE quantizers by about 0.35 bit per block for the same number of levels. Picture quality using a 24-level MMSSD quantizer can be produced by an MMSE quantizer with an increase in entropy of 0.6 bit per block. It is worth noting that, due to the DPCM coding of H_1 , the bits required for H_1 could be almost halved. However, H_1 still remains more important than H_2 and H_4 and requires more bits for satisfactory transmission.

		MMSSD QUANTIZERS						
		Number of Levels						
		20	22	24	26	28	30	32
MMSE QUANTIZERS	26	50	100	100	100	100	100	100
	28	17	100	100	83	100	100	100
	30	17	50	50	67	50	100	100
	32	0	50	67	67	67	100	100

Fig. 21—Comparison of picture quality of MMSSD and MMSE quantizers of different levels for DPCM coding of H_1 .

4.5 Combined quantization of all coefficients

Combined quantization of all the coefficients requires investigation of the optimal number of quantizer levels to be given to each one of them. In the case of gaussian random vectors using Karhunen-Loeve transformation and mean-square error criterion, optimal bit allocation for the various transform coefficients is well known.^{29,30} However, in our case, none of these assumptions are strictly valid. In fact, our assumption that the optimum quantizer characteristics for different coefficients can be obtained independently is not strictly true and, for this reason, we tried to evaluate the picture quality by quantizing all the coefficients. By trial and error, a near-perfect picture was produced by using 36, 13, and 7 quantization levels for ΔH_1 , H_2 , and H_4 respectively, and by dropping H_3 . This resulted in a total entropy of about 2.17 bits per pel. In single-frame photographic reproduction, no difference could be observed between the coded picture and the low-resolution original shown in Fig. 5a. Several other "head and shoulders" type of pictures were coded using the same combination of levels. Although, in each case the picture appeared to have a reasonable quality, the visibility of the quantization and the resulting picture quality varied slightly. This implies that the quantizers we obtained by optimizing the visibility of the quantization noise for one particular picture were not overly sensitive to variation in picture content.

V. CONCLUSIONS

A systematic method for quantizing Hadamard coefficients has been given. This method gives the best quantizers in a subjective and probabilistic sense. We have compared the resulting quantizers with MMSE quantizers and found the MMSSD quantizers to be better both in terms

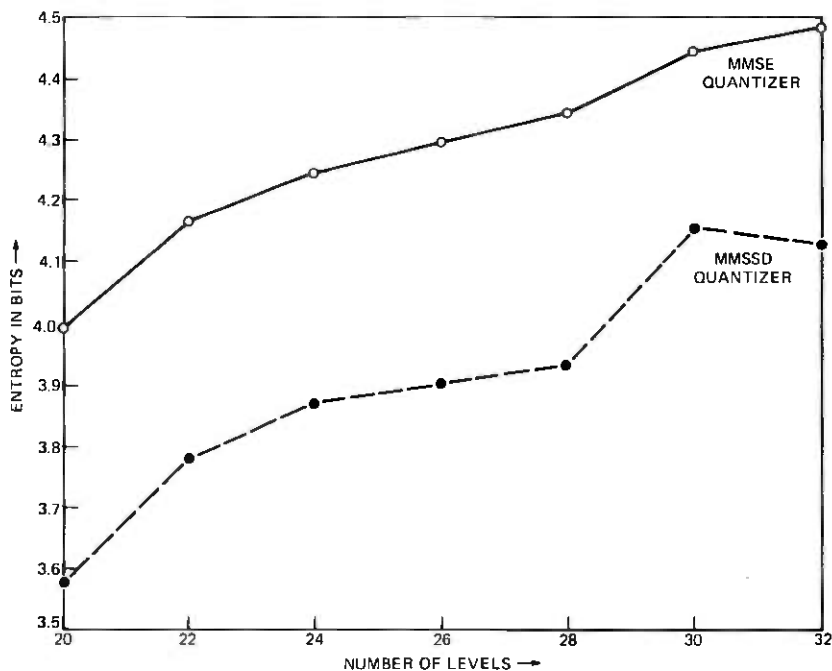


Fig. 22—Plots of entropy of outputs of MMSSD and MMSE quantizers of different levels for DPCM coding of H_1 .

of the subjective picture quality and entropy. We do not imply that there are no better quantizer than the MMSSD quantizer, since by taking many other factors into consideration, one could come up with a better quantizer. We do find that the minimum visibility quantizers are optimum with respect to our model and the approach used for weighting the quantization noise.

Investigations are in progress for adaptive and predictive coding of the coefficients; our findings will be reported in a future paper.³¹

VI. ACKNOWLEDGMENT

We would like to thank J. C. Candy, B. G. Haskell, and K. A. Walsh for help in various phases of this work. Thanks are also due to E. G. Bowen, R. H. Bosworth, R. C. Brainard, E. F. Brown, J. E. Berrang, and R. L. Schmidt for generously giving their time as subjects.

REFERENCES

1. H. J. Landau and D. Slepian, "Some Computer Experiments in Picture Processing for Bandwidth Reduction," *B.S.T.J.*, 50, No. 5 (May-June 1971), pp. 1525-1540.
2. W. K. Pratt and H. C. Andrews, "Fourier Transform Coding of Images," *Proc. Hawaii Intern. Conf. System Sciences*, January 1968.
3. W. K. Pratt, J. Kane, and H. C. Andrews, "Hadamard Transform Image Coding," *Proc. IEEE*, 57, No. 1 (January 1969), pp. 58-68.

4. M. Tasto and P. A. Wintz, *Picture Bandwidth Compression by Adaptive Block Quantization*, Technical Report TR-EE-70-14, July 1970, Purdue University, Lafayette, Indiana.
5. P. A. Wintz, "Transform Picture Coding," *Proc. IEEE*, 60, No. 7 (July 1972), pp. 809-820.
6. J. W. Woods and T. S. Huang, *Picture Bandwidth Compression by Linear Transformation and Block Quantization*, 1969 Symposium on Picture Bandwidth Compression, Massachusetts Institute of Technology, New York: Gordon and Breach, 1972.
7. G. B. Anderson and T. S. Huang, "Piecewise Fourier Transformation for Picture Bandwidth Compression," *IEEE Trans. Commun. Technol.*, COM-19 (April 1971), pp. 133-140.
8. A. Habibi and P. A. Wintz, "Image Coding by Linear Transformation and Block Quantization," *IEEE Trans. Commun. Technol.*, COM-19 (February 1971), pp. 50-60.
9. A. Habibi, "Hybrid Coding of Pictorial Data," *IEEE Trans. Commun. Technol.*, COM-22, No. 5 (May 1974), pp. 614-620.
10. S. C. Knauer, "Video Compression Algorithm for Hadamard Transform Processing," *IEEE Trans. Electromagnet. Compat.*, EMC-18, No. 1 (February 1976), pp. 28-36.
11. *Applications of Walsh Functions*, Conference Proceedings and Symposium, 1971 through 1974, IEEE Electromagnetic and Compatibility Group.
12. B. J. L. Fino, "Recursive Generation and Computation of Fast Unitary Transforms," Memo No. ERL-M-514, Electronics Research Laboratory, University of California, Berkeley, January 1974.
13. R. M. Haralick and K. Shanmugam, "Comparative Study of a Discrete Linear Basis for Image Data Compression," *IEEE Trans. Systems, Man and Cybernetics*, SMC-4, No. 1 (January 1974), p. 16.
14. M. Ishii, "Picture Bandwidth Compression by DPCM in the Hadamard Transform Domain," *Fujitsu Sci. & Tech. J.*, 10, No. 3 (September 1974), pp. 51-65.
15. H. C. Andrews, *Computer Techniques in Image Processing*, New York: Academic Press, 1970, Chapter 7.
16. J. Pearl and H. C. Andrews, "Performance Measures for Transform Data Coding," *IEEE Trans. Commun. Technol.*, COM-20 (June 1972), pp. 411-415.
17. W. F. Schreiber, "Picture Coding," *Proc. IEEE*, 55 (March 1967), pp. 320-330.
18. J. O. Limb, Ref. 17, pp. 364-379.
19. T. L. Mannos and D. J. Sakrison, "The Effects of Visual Fidelity Criterion on the Encoding of Images," *IEEE Trans. Inform. Theory*, IT-20, No. 4 (July 1974), pp. 525-536.
20. J. C. Candy and R. H. Bosworth, "Methods for Designing Differential Quantizers Based on Subjective Evaluations of Edge Busyness," *B.S.T.J.*, 51, No. 7 (September 1972), pp. 1495-1516.
21. G. F. Newell and W. K. E. Geddes, "The Visibility of Small Perturbations in Television Displays," BBC Engineering Division, Research Department, Report T-106, 1963.
22. H. Harms and E. Aulhorn, "Studien Über den Grenzkontrast. I Mitteilung. Ein neues Grenzphänomen," *Grafes Arch. Ophthalm.*, 157, 1955, pp. 3-23.
23. D. Teller, "The Influence of Borders on Increment Thresholds," Ph.D. Thesis, Department of Psychology, University of California, Berkeley, 1965.
24. S. S. Stevens, *Handbook of Experimental Psychology*, New York: Wiley, 1951.
25. K. Hacking, "The Relative Visibility of Random Noise Over the Grey-Scale," *J. Brit. Inst. Radio Eng.*, 23, No. 4 (April 1962), pp. 307-310.
26. T. G. Stockham, "Image Processing in the Context of a Visual Model," *Proc. IEEE*, 60, No. 7 (July 1972), pp. 828-842.
27. F. Kretz, "Subjectively Optimal Quantization of Pictures," *IEEE Trans. Commun.*, COM-23 (November 1975), pp. 1288-1292.
28. J. Max, "Quantizing for Minimum Distortion," *IEEE Trans. Inform. Theory*, IT-6 (March 1960), pp. 7-12.
29. J. Y. Huang and P. M. Schultheiss, "Block Quantization of Correlated Gaussian Random Variables," *IEEE Trans. Commun. Syst.*, CS-11 (September 1963), pp. 289-296.
30. A. Segall, "Bit Allocation and Encoding for Vector Sources," *IEEE Trans. Inform. Theory*, IT-22 (March 1976), pp. 162-169.
31. F. W. Mounts, A. N. Netravali, and B. Prasada, "Some Experiments in Adaptive and Predictive Hadamard Transform Coding of Pictures," unpublished work.

Modal Dispersion in Optical Fibers With Arbitrary Numerical Aperture and Profile Dispersion

By E. A. J. MARCATILI

(Manuscript received April 28, 1976)

Design criteria to minimize modal dispersion have been found for a broad class of practical, multimode, circular-symmetric, isotropic, optical fibers having any numerical aperture and any profile dispersion (which is a function of the derivative of the index with respect to the wavelength). The impulse-response width of these fibers, the rms width of the impulse response, the optimum profiles to minimize those widths, and the sensitivity to profile departures from ideal are found to be surprisingly simple closed-form generalizations of previous results that are mostly applicable to fibers with small numerical aperture and constant profile dispersion. The minimum impulse-response width of the optimized fiber is a function only of its numerical aperture and consequently is independent of the index profile and of the profile dispersion.

I. INTRODUCTION

Circular-symmetric, multimode, optical fibers intended for large communication capacity must have low modal dispersion and this is achievable by the quasi-complete equalization of the group velocities of all modes¹ (or rays). This equalization depends critically both on the refractive-index profile and on the profile dispersion of the fiber. The profile dispersion is defined in Section II, but here it is enough to know that it is related to the derivative of the index with respect to the wavelength.

To understand better the objectives of this paper, let us first review some recent evolution of thoughts linking the index profile and the profile dispersion of a fiber to the pulse broadening caused by modal dispersion.

Gloge and Marcatili² showed that if the numerical aperture (NA) of the fiber is arbitrary but the profile dispersion is negligible, there is a family of fibers—for which the dielectric constant profiles decrease radially according to power laws—that is important for two reasons. The first reason is that the family encompasses a wide variety of easy-to-make fibers (step-index, quasi-parabolic, etc.) possessing the unique property that the group velocity of each mode is a function only of its propagation constant; this drastically simplifies the analysis. The second and more important point is that for an almost parabolic power law of the dielectric profile, a fiber with small NA has the very narrow impulse response needed for high-speed communication.

Olshansky and Keck³ extended these results in a very important way by showing that if the profile dispersion is constant across the core, narrow impulse response is achievable in small NA fibers by a simple modification of the exponent of the dielectric-constant profile's power law.

In many cases, though, the two requirements—smallness of NA and constancy of profile dispersion—are not satisfied. For example, to increase the coupling efficiency to incoherent sources and to decrease microbending losses,⁴ fibers with large NAs⁵ are being made. They are heavily doped and, particularly if the doping element is boron, the profile dispersion may not be a constant^{6,7} as a function of the radius. Similar lack of constancy may occur in fibers that are doped with several materials for the purpose of improving optical or mechanical properties.⁸ Arnaud and Flemming^{9,10} have calculated the impulse response for these fibers, treating the variable portions of the profile dispersion as a perturbation. Using a numerical method Arnaud¹¹ has also calculated the pulse spreading in a multimode planar fiber with arbitrary index profile and profile dispersion.

In this paper, we extend the previous results by finding, within the WKB approximation, a surprisingly simple closed-form description of the modal dispersion in a broad class of circular-symmetric isotropic fibers which have arbitrarily large NA and arbitrary profile dispersion.

The gist of our paper is in Sections II and III. In Section II, the profiles of the fibers belonging to the group are defined and their impulse-response widths are calculated. In Section III, the optimum index profile required to minimize the impulse-response width is determined together with the sensitivity of this response to departures of the index from optimum. The rms of the impulse response is the subject of Section IV. In Section V, some approximate results about the influence of index profiles on the minimization of the rms width of the impulse response are derived and conclusions are drawn in Section VI.

II. FIBER PROFILE AND WIDTH OF ITS IMPULSE RESPONSE

We start by looking for the dielectric-constant profile of a circular symmetric isotropic fiber such that, as in Ref. 2, the group velocity of each mode is only a function of its propagation constant. In the process, we will also find the width of the impulse response of that fiber.

The initial point is a WKB approximation² that relates the propagation constant $\beta(\lambda)$ of a mode characterized by the radial and azimuthal wave numbers μ and ν to the free-space propagation constant $k = 2\pi/\lambda$, the refractive index $n(r, \lambda)$ of the fiber and the radial coordinate r , via the integral

$$\mu = \frac{1}{\pi} \int_{r_1}^{r_2} \rho \frac{dr}{r}, \quad (1)$$

where

$$\rho(r, \lambda) = \sqrt{(k^2 n^2 - \beta^2) r^2 - \nu^2} \quad (2)$$

and r_1 and r_2 are two neighboring turning points that make the radical zero and between which most of the field of the mode is concentrated. It is useful to redefine

$$n^2 = n_1^2(1 - F) \quad (3)$$

$$\beta^2 = k^2 n_1^2(1 - B), \quad (4)$$

where n_1 is the index on axis and the profile function $F(r, \lambda)$ is zero on axis, is an arbitrary function of r and λ within the core ($r \leq a$), and is $2\Delta(\lambda)$, a function only of λ in the cladding ($r \geq a$). Similarly, the mode parameter B varies between zero for the lowest-order mode and $2\Delta(\lambda)$ for the modes whose phase velocities coincide with that of a plane wave in the cladding.* With these definitions, the radical (2) becomes

$$\rho = \sqrt{(kn_1r)^2(B - F) - \nu^2}. \quad (5)$$

The group velocity of a mode (or ray) is introduced by taking the derivative of both sides of (1) with respect to the free-space wavelength λ ,

$$\int_{r_1}^{r_2} \left[B \left(1 - \frac{n_1}{2N_1} \frac{\lambda}{B} \frac{dB}{d\lambda} \right) - F \left(1 - \frac{F}{2} \right) \right] \frac{r}{\rho} dr = 0, \quad (6)$$

where

$$N_1 = n_1 \left(1 - \frac{\lambda}{n_1} \frac{dn_1}{d\lambda} \right) \quad (7)$$

* Similar but not identical profile function and mode parameter have been introduced previously in the literature.¹²

is the group index on axis and

$$p(r, \lambda) = \frac{n_1 \lambda}{N_1 F} \frac{\partial F}{\partial \lambda} \quad (8)$$

is a generalized version of the profile dispersion parameter introduced in Ref. 12.

The derivative $dB/d\lambda$ in (6) can be expressed in terms of the group delay t of the mode by taking square roots and derivatives on both sides of (4). The result is

$$\frac{d\beta}{dkn_1} = \frac{t}{T} = \sqrt{1-B} + \frac{n_1}{2N_1} \frac{\lambda}{\sqrt{1-B}} \frac{dB}{d\lambda} \quad (9)$$

in which T , the flight time on axis, that is, the delay of a plane wave in a medium of group index N_1 and length L , is related to the velocity of the light in free space c via

$$T = \frac{LN_1}{c}. \quad (10)$$

The substitution of $dB/d\lambda$ from (9) into (6) yields the integral

$$\int_{r_1}^{r_2} \left[1 - \sqrt{1-B} \frac{t}{T} - F \left(1 - \frac{p}{2} \right) \right] \frac{r}{\rho} dr = 0. \quad (11)$$

This integral was solved in Refs. (2) and (3) by assuming p constant and $F = 2\Delta(r/a)^\alpha$, a power law, with α an arbitrary constant. To lift these restrictions and still solve (11) exactly, the following self-evident expression is introduced:

$$\int_{r_1}^{r_2} \frac{\partial \rho}{\partial r} dr = \rho(r_2, \lambda) - \rho(r_1, \lambda) = 0. \quad (12)$$

This integral becomes less obvious and very useful when the derivative $\partial \rho / \partial r$ is performed with the help of (5), yielding

$$\int_{r_1}^{r_2} \left[B - F - \frac{r}{2} \frac{\partial F}{\partial r} \right] \frac{dr}{\rho} = 0. \quad (13)$$

Combining (13) with (11), we arrive at a general expression

$$\frac{1 - \sqrt{1-B} \frac{t}{T}}{B} = \frac{\int_{r_1}^{r_2} \left(1 - \frac{p}{2} \right) \frac{Fr}{\rho} dr}{\int_{r_1}^{r_2} \left(1 + \frac{r}{2F} \frac{\partial F}{\partial r} \right) \frac{Fr}{\rho} dr}, \quad (14)$$

that like (11), relates the group delay t of a mode characterized by its mode parameter B (or propagation constant β), and its azimuthal mode number ν (hidden in ρ) to the profile function F and profile dispersion p . This expression is valid for any circular-symmetric fiber with isotropic dielectric and, in general, still cannot be solved exactly. However, if a particular family of fibers is considered that satisfies the condition

$$\frac{1 + \frac{r}{2F} \frac{\partial F}{\partial r}}{1 - \frac{p}{2}} = D(\lambda), \quad (15)$$

D being an arbitrary function of λ , the seemingly formidable right-hand side of (14) is reduced to $1/D$ and the group delay of the mode characterized by the mode parameter B is

$$t = T \frac{1 - \frac{B}{D}}{\sqrt{1 - B}}. \quad (16)$$

These last two equations are the basic results of the paper. Equation (16) says that t , the group delay of a mode (or ray) is only a function of the mode parameter B and the dispersion parameter D . More important, the group delay is independent of the mode number (which means that modes with the same propagation constant have the same delay), it is independent of the profile function F , and it is independent of the profile dispersion p . Equation (16) is used in the following sections to study the impulse response of the fiber.

On the other hand, eq. (15) is the recipe for the design of the fiber whose time response is given by (16). It can be solved in several ways depending on the control that the fiber designer has over F and its derivatives with respect to λ . The least demands on these functions occur if the fiber is designed to operate at one wavelength only. Then, in (15), D becomes a constant, p is only a function of r , and the partial derivative of F is reduced to an ordinary one. Without introducing new symbols for D , F , and p , the simplified design formula is

$$\frac{1 + \frac{r}{2F} \frac{dF}{dr}}{1 - \frac{p}{2}} = D. \quad (17)$$

This equation in turn can be solved in two ways. One way consists in prescribing the profile function F to satisfy, perhaps, requirements

different from modal dispersion. Then, the profile dispersion p must be tailored to satisfy (17).

For example, assume the dielectric profile depicted in Fig. 1a. The profile function is

$$F = \begin{cases} 2\Delta \left(\frac{r}{a_1}\right)^{\alpha_1} & \text{for } 0 < r < a_0 \\ 2\Delta \left(\frac{r}{a}\right)^{\alpha_2} & \text{for } a_0 < r < a, \end{cases} \quad (18)$$

where

$$a_0 = a_1 \left(\frac{a_1}{a}\right)^{\alpha_2/(\alpha_1 - \alpha_2)} \quad (19)$$

and the inequalities

$$\begin{aligned} a_1 &< a \\ \alpha_1 &> \alpha_2 > 0 \end{aligned} \quad (20)$$

guarantee that the profile looks indeed like that in Fig. 1a.

Substituting (18) in (17) and assuming for the dispersion parameter D a value D_0 that optimizes in some sense the impulse response of the fiber, the required profile dispersion turns out to be

$$p = \begin{cases} 2 - \frac{2 + \alpha_1}{D_0} & \text{for } r < a_0 \\ 2 - \frac{2 + \alpha_2}{D_0} & \text{for } a_0 < r < a \end{cases} \quad (21)$$

and is shown in Fig. 1b.

This is an interesting example not only because it clearly illustrates the power of the theory even to design optimized fibers in which the profile function and dispersion are discontinuous, but also because it may be of practical interest. For example, by using an index-increasing dopant for $r < a_0$ and an index-decreasing dopant for $r > a_0$ the NA of the fiber can be increased, keeping at the same time its optimum modal dispersion.

In the other way of solving (17), the profile dispersion p as a function F is assumed to be known, from experiment, and the index profile must be found from the integration of (17) that yields

$$r = a \exp \int_F^{2\Delta} \frac{dF}{[2 - D(2 - p)]F} \quad (22)$$

This result will be used in a more general way later, but if for the time being we prescribe p to be a constant P_0 , the profile function results:

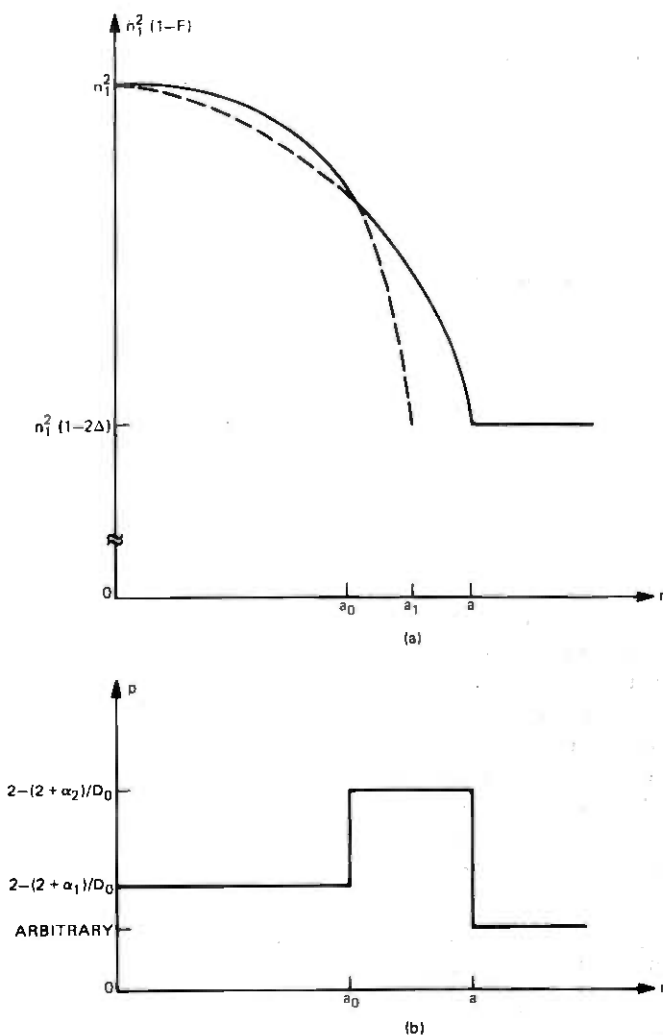


Fig. 1—(a) Dielectric profile (solid line). (b) Profile dispersion.

$$F = 2\Delta \left(\frac{r}{a}\right)^\alpha, \quad (23)$$

where

$$\alpha = D(2 - P_0) - 2. \quad (24)$$

This last equation establishes the relation between the dispersion parameter D of the fiber introduced in this paper and the α value so widely used in the literature^{2,3} for fibers with constant profile dispersion P_0 . It follows from (17) that only if p is a constant, is the profile function F a power law (23).

The two solutions described require only the control over the profile function F and its first derivative with respect to λ . But suppose that the fiber designer has also control over the second derivative. Then, to increase the range of wavelengths over which the fiber operates with low modal dispersion, he could demand, for example, that at a wavelength not only

$$D = D_0$$

but also, as proposed by Kaminow and Presby,¹³

$$\frac{dD}{d\lambda} = 0. \quad (25)$$

This requires the simultaneous satisfaction of (17) and

$$\frac{\frac{\partial}{\partial \lambda} \left(\frac{r}{F} \frac{\partial F}{\partial r} \right)}{\frac{\partial p}{\partial \lambda}} = -D_0 \quad (26)$$

derived from (15) and (25). It is this last equation that implies the control over the second derivative of F with respect to λ .

It can easily be extrapolated that control over higher derivatives permits even further demands on D . In fact, if all the higher derivatives were controllable, $D(\lambda)$ could be chosen arbitrarily and the profile F would be the solution of the linear partial differential equation of first order (15) subject to the conditions of being zero at $r = 0$ and $2\Delta(\lambda)$ at $r = a$; the result is well known¹⁴ from a mathematical point of view, but of limited importance from a practical point of view.

III. MINIMIZATION OF THE IMPULSE-RESPONSE WIDTH AND ITS SENSITIVITY TO ERRORS IN THE PROFILE

The impulse-response width is determined from (16) by finding the difference between flight times of the slowest and the fastest modes (or rays) for any given value of the dispersion parameter D . It is simple to find that the minimum time spread, τ_{\min} , between those modes occurs if D is chosen

$$D_0 = 1 + \sqrt{1 - 2\Delta}. \quad (27)$$

In fact, the modes characterized by $B = 0$ and $B = 2\Delta$ are the slowest and arrive at the end of the fiber at

$$t_{\max} = T, \quad (28)$$

while the modes characterized by $B = 1 - \sqrt{1 - 2\Delta}$ are the fastest and arrive at

$$t_{\min} = T \frac{2(1 - 2\Delta)^{1/4}}{1 + \sqrt{1 - 2\Delta}} \quad (29)$$

The time spread between them is the minimum impulse-response width

$$\tau_{\min} = t_{\max} - t_{\min} = T \frac{[1 - (1 - 2\Delta)^{1/4}]^2}{1 + \sqrt{1 - 2\Delta}} \quad (30)$$

Therefore, fibers with the same Δ have the same minimum impulse-response width τ_{\min} , independently of their index profiles and profile dispersions, provided that they satisfy the design equation (17) with D substituted by the optimum value D_0 (27).

If

$$\Delta \ll 1,$$

(27) and (30) become

$$D_0 \cong 2 - \Delta \quad (31)$$

$$\tau_{\min} \cong \frac{\Delta^2}{8} T = 0.61 \Delta^2 \mu\text{s/km} \quad (32)$$

for $N_1 = 1.46$.

To find the sensitivity of the impulse-response width to departures of the index profile from optimum, we calculate the ratio τ/τ_{\min} between the response width τ for

$$D = (1 + \delta)D_0, \quad (33)$$

where

$$\delta \ll 1$$

and the minimum response width τ_{\min} occurring for $D = D_0$. After some straightforward calculations,

$$\frac{\tau}{\tau_{\min}} = \left\{ 1 + \frac{|\delta|}{8\Delta} (1 + \sqrt{1 - 2\Delta})^2 [1 + (1 - 2\Delta)^{1/4}]^2 \right\}^2 \quad (34)$$

and for

$$\frac{\tau}{\tau_{\min}} = \left(1 + \frac{2|\delta|}{\Delta} \right)^2 \quad (35)$$

It is known that the impulse-response width is indeed very sensitive to the choice of profile and more so for smaller Δ . If δ , the fractional departure of D from its optimum value, is equal to Δ , then the pulse width is nine times larger than τ_{\min} .

The main results in the last two sections have been extended by Ar-

naud to optimize modal dispersion in fibers with noncircularly symmetric profiles.¹⁵

IV. THE RMS OF THE IMPULSE RESPONSE

From the point of view of the maximum information-carrying capacity of a fiber, more significant than the impulse response width is its rms width σ ,¹⁶ since $1/4\sigma$ is the repetition rate at which pulses can be transmitted with a reasonable loss penalty at the receiving end.¹

Let us calculate first the impulse response $W(t)$ and then its rms width σ assuming that:

- (i) The energy of the infinitely narrow impulse fed at one end of the fiber is equipartitioned among all modes.
- (ii) All modes attenuate equally.
- (iii) The number of modes is so large that the discrete pulses arriving at the receiving end can be replaced by a continuum.

The impulse response, then, is the rate of change of the number of modes reaching the end of the fiber,

$$W(t) = \frac{d}{dt} \int_0^{r_{\max}} \mu(\nu, t) d\nu, \quad (36)$$

and its rms width is, by definition,

$$\sigma = \left(\frac{\frac{1}{2} \int_0^{\infty} \int_0^{\infty} W(t_1) W(t_2) (t_1 - t_2)^2 dt_1 dt_2}{\int_0^{\infty} \int_0^{\infty} W(t_1) W(t_2) dt_1 dt_2} \right)^{1/2}. \quad (37)$$

To calculate $W(t)$, the value of μ given in (1) is substituted in (36) and the integration along ν is carried through yielding

$$W(t) = \frac{k^2 n_1^2}{4} \frac{d}{dt} \int_0^{r_B} (B - F) r dr. \quad (38)$$

The integral measures the energy arriving at the end of the fiber as a function of time and, since each contribution must be positive, the largest value that F can reach is B . Therefore, the upper limit r_B is the value of r that makes

$$F(r, \lambda) = B(\lambda). \quad (39)$$

The explicit value of r_B depends on the choice of fiber design. If the profile function F is prescribed, then r_B is obtained by solving (39). If, on the other hand, the profile dispersion is prescribed, then

$$r_B = a \exp \int_B^{2\Delta} \frac{dF}{[2 - D(2 - p)]F} \quad (40)$$

follows from (22).

Now the derivative with respect to time in (38) is carried out. The derivative of the integral is equal to the integral of the derivative since the terms that should contain the integrand times the derivatives of the limits are zero. Consequently,

$$W(t) = \frac{(kn_1 r_B)^2}{8} \frac{dB}{dt}. \quad (41)$$

The reader interested in the explicit impulse response must substitute B in this expression with its time-dependent value obtained from (16).

Replacing $W(t)$ in (37) and also substituting the explicit value of t from (16), the rms width of the impulse response results in

$$\sigma = \frac{T}{\sqrt{2}} \left(\frac{\int \int_0^{2\Delta} \left(\frac{1-x/D}{\sqrt{1-x}} - \frac{1-y/D}{\sqrt{1-y}} \right)^2 r_x^2 r_y^2 dx dy}{\int \int_0^{2\Delta} r_x^2 r_y^2 dx dy} \right)^{1/2}, \quad (42)$$

where x and y are dummy variables and r_x and r_y are given by (40) once B is substituted either by x or by y . It is easy to recognize in (42) that if $\Delta \ll 1$ and $D \cong 2$, the parenthesis is of the order of Δ^2 and σ is proportional to $\Delta^2 T$.

Unlike the simple impulse-response width, the rms width σ and the optimum value of D that minimizes it are dependent on the profile dispersion ρ and the profile function F . In general, the exact value of σ and its minimizations must be found numerically, but we push the analysis a little further in the next section where some simplifying assumptions are made.

V. APPROXIMATE RESULTS FOR RMS WIDTH OF THE IMPULSE RESPONSE, ITS MINIMIZATION, AND ITS SENSITIVITY TO PROFILE ERRORS

Within the family of fibers described in the previous sections there is a large group of particular importance that encompasses many of the available fibers today. This group has small NA and its profile dispersion is almost constant with respect to r . To introduce these properties, we assume

$$\Delta \ll 1, \quad (43)$$

then the profile dispersion is expanded in power series of the profile function F ,

$$\rho = \sum_{s=0}^{\infty} P_s \left(\frac{F}{2\Delta} \right)^s, \quad (44)$$

and since F is a function of r , the near invariance of p with r implies

$$\sum_{s=1}^{\infty} P_s \left(\frac{F}{2\Delta} \right)^s \ll 1. \quad (45)$$

5.1 Profile function

Carrying this simplifying assumption to (22) by keeping only first powers of P_s ($s > 0$), the profile function results:

$$F = 2\Delta \left(\frac{r}{a} \right)^\alpha \left\{ 1 + \frac{2}{\alpha} \sum_{s=1}^{\infty} \frac{P_s}{s} \left[1 - \left(\frac{r}{a} \right)^{s\alpha} \right] \right\}, \quad (46)$$

where

$$\alpha = D(2 - P_0) - 2 \quad (47)$$

and D is still an arbitrary number.

If the profile dispersion is constant, the summation in (46) disappears; then, and only then, will the profile function follow a pure power law.

5.2 Minimization of the rms width of the impulse response and its sensitivity to profile errors

We want to find σ_{\min} , the minimum rms width of the impulse response possible, and D_1 , the optimum dispersion parameter for which σ_{\min} is achieved. The optimum profile is obtained by substituting D with D_1 in (46). We are interested also in finding the sensitivity of σ to small errors in the profile.

To achieve these purposes σ^2 is expanded in a power series about D_1 , and only the first three terms are kept,

$$\sigma^2 = \sigma_{\min}^2 + (D - D_1) \frac{d\sigma^2}{dD} + \frac{(D - D_1)^2}{2} \frac{d^2\sigma^2}{dD^2}. \quad (48)$$

The derivatives are to be taken at $D = D_1$. Since by definition σ^2 passes through a minimum of $D = D_1$, the equation

$$\frac{d\sigma^2}{dD} = 0 \quad \text{at} \quad D = D_1 \quad (49)$$

serves to determine the optimum dispersion parameter D_1 .

From (42), (48), and (49), we obtain with the help of (43) and (45)

$$D_1 = 2 \left[1 - \frac{\Delta}{2} \frac{1 + 2H}{1 + 4H} (1 + \Sigma) \right] \quad (50)$$

$$\sigma_{\min} = T(\Delta H)^2 \frac{(1 + H)^{1/2}}{(1 + 3H)(1 + 4H)(1 + 5H)^{1/2}} \quad (51)$$

$$\frac{\sigma}{\sigma_{\min}} = \sqrt{1 + \left(\frac{D - D_1}{D_1 \Delta H} \frac{1 + 4H}{1 + 2H} \right)^2 (1 + 3H)(1 + 5H)}, \quad (52)$$

where

$$\Sigma = 2 \sum_{s=1}^{\infty} P_s \frac{(s^2 + s + 6)H^2 + 8H + 2}{\{[(s + 2)H + 1]^2 - H^2\} \{[(s + 3)H + 1]^2 - H^2\}} \quad (53)$$

and

$$H = 1 - P_0. \quad (54)$$

The optimum value of the dispersion parameter D_1 is close to 2. The profile function that maximizes the information-carrying capacity of the fiber is obtained by substituting D with D_1 in (46). The dispersion-profile terms of order higher than zero appear in (50) only in the summation Σ and are multiplied by Δ . Therefore, their contribution is small indeed and is neglected in (51) and (52). It is kept in (50) because, as will be seen later, small errors in the profile affect substantially the value of σ . For $\Sigma = 0$, the substitution of (50) in (47) yields the same optimum α of Ref. 3.

Consider now σ_{\min} , the minimum rms width of the impulse response. From (51), we might be tempted to conclude that $H = 1 - P_0$ should be made small to decrease σ_{\min} . However, the number of modes of the guide derived from (38) with the help of (46) is

$$N = \left(\frac{kn_1 a}{2} \right)^2 \frac{\Delta H}{1 + H}. \quad (55)$$

Therefore, if the number of modes of the fiber is to be kept constant, σ_{\min} can be decreased by making

$$\frac{(1 + H)^{5/2}}{(1 + 3H)(1 + 4H)(1 + 5H)^{1/2}}$$

small and this is achieved by choosing H large, not small.

The following table contains the minimum rms per unit length of fiber, σ_{\min}/L , and the concomitant pulse repetition rate $L/4\sigma_{\min}$ for different values of H as derived from (58), assuming $N_1 = 1.46$.

H	σ_{\min}/L $\mu\text{s}/\text{km}$	$\text{PRR} = \frac{L}{4\sigma_{\min}}$ $\text{Mb} \cdot \text{km}/\text{s}$
1	$0.14\Delta^2$	$1.79/\Delta^2$
2	$0.16\Delta^2$	$1.56/\Delta^2$
∞	$0.18\Delta^2$	$1.38/\Delta^2$

For $H > 1$, the pulse repetition rate is fairly insensitive to the value of H . For $H = 1$ and $\Delta = 0.01$, the pulse repetition rate is ~ 18 Gb/km/s. This information-carrying capacity is only 33 percent smaller than that of the "ideal profile" reported by Cook.¹⁷

Let us turn now to the sensitivity of the rms width to errors in profile (52). Again, for $H > 1$, this result is insensitive to the value of H ; indeed

$$\frac{\sigma}{\sigma_{\min}} = \begin{cases} \sqrt{1 + 66.7 \left(\frac{D - D_1}{D_1 \Delta} \right)^2} & \text{for } H = 1 \\ \sqrt{1 + 60 \left(\frac{D - D_1}{D_1 \Delta} \right)^2} & \text{for } H = \infty. \end{cases} \quad (56)$$

For $H = 1$ and $(D - D_1)/D_1$, the fractional departure of D with respect to the optimum D_1 equal to Δ , the rms width σ is about 8.4 times wider than σ_{\min} . As in the case of the pulse width, the rms width is very sensitive to profile errors.

A fiber designed to minimize the rms width ($D = D_1$) has only 30 percent more information-carrying capacity than a fiber with the same Δ designed to minimize the impulse-response width ($D = D_0$).

VI. CONCLUSIONS

For a vast class of circular-symmetric fibers made of isotropic dielectrics, simple and fundamental design criteria that minimize the impulse-response width due to modal dispersion at one wavelength have been found. This minimum width (30) is only a function of the NA and the time of flight along the axis. Therefore, if properly designed, a fiber with arbitrary profile dispersion has the same minimum impulse-response width as another fiber with the same NA and no profile dispersion. Their information-carrying capacity is about $1.4/\Delta^2$ Mb · km/s. The fiber engineer has a substantial freedom of choice to reach that optimum design: the profile dispersion may be arbitrarily chosen but then the index profile is uniquely determined by (22); or symmetrically, the index profile may be arbitrarily chosen and then the profile dispersion must satisfy (17). Only if the profile dispersion is a constant does the optimum dielectric profile that minimizes the impulse response follow a power law.

The profile dispersion entails the first derivative of the index with respect to the wavelength. If the second derivative can be controlled, then the minimization of the impulse-response width can be achieved at two neighboring wavelengths. This broadbanding of the fiber response can be expanded even further if higher derivatives are under control.

The width of the impulse response is very sensitive to errors in the fiber design. A fractional error of Δ in the dispersion parameter of the fiber makes the response about nine times wider than the minimum as seen from (35).

Only a marginal increase of about 25 percent in the information-carrying capacity of the fiber is achieved if the rms width of the impulse response is minimized instead of minimizing the impulse-response width.

REFERENCES

1. S. E. Miller, E. A. J. Marcatili, and T. Li, "Research Toward Optical-Fiber Transmission Systems," Proc. IEEE, *61* (December 1973), pp. 1703-1751.
2. D. Gloge and E. A. J. Marcatili, "Multimode Theory of Graded-Core Fibers," B.S.T.J., *52* (November 1973), pp. 1563-1577.
3. R. Olshansky and D. B. Keck, "Pulse Broadening in Graded-Index Optical Fibers," Appl. Opt., *15* (February 1976), pp. 483-491.
4. D. Gloge, "Optical-Fiber Packaging and Its Influence on Fiber Straightness and Loss," B.S.T.J., *54* (February 1975), pp. 245-263.
5. P. B. O'Connor, P. Kaiser, J. B. MacChesney, C. A. Burrus, H. M. Presby, L. G. Cohen, and F. V. DiMarcello, "Large-Numerical-Aperture, Germanium Doped Fibers for LED Application," Second European Conference on Optical Fibre Communication, (September 1976) Paris.
6. J. W. Fleming, "Measurements of Dispersion in GeO_2 , B_2O_3 , SiO_2 Glasses," J. Amer. Ceram. Soc., *59*, No. 11-12, pp. 503-507.
7. H. M. Presby and I. P. Kaminow, "Refractive Index and Profile Dispersion Measurements in Binary Silica Optical Fibers," Appl. Opt., (December 1976).
8. J. B. MacChesney, P. B. O'Connor, and H. M. Presby, "A New Technique for the Preparation of Low-Loss and Graded-Index Optical Fibers," Proc. IEEE, *62* (September 1974), pp. 1280-1281.
9. J. A. Arnaud, "Pulse Broadening in Multimode Optical Fibers," B.S.T.J., *54* (September 1975), pp. 1179-1207.
10. J. A. Arnaud and J. W. Fleming, "Pulse Broadening in Multimode Optical Fibers With Large $\Delta n/n$, Numerical Results," Elect. Lett. (January 1977).
11. J. A. Arnaud, "Pulse Spreading in Multimode, Planar, Optical Fibers," B.S.T.J., *53* (October 1974), pp. 1599-1618.
12. D. Gloge, I. P. Kaminow, and H. M. Presby, "Profile Dispersion in Multimode Fibers: Measurement and Analysis," Elect. Lett., *11* (September 1975), pp. 469-471.
13. I. P. Kaminow and H. M. Presby, "Profile Synthesis in Multicomponent Glass Optical Fibers," Appl. Opt., *16* (January 1977).
14. P. B. Hildebrand, *Advanced Calculus for Engineers*, New York: Prentice-Hall, 1949.
15. J. A. Arnaud, "Optimum Profiles for Dispersive Multimode Fibers," Elect. Lett., (January 1977).
16. S. D. Personick, "Receiver Design for Digital Fiber Optic Communication Systems, Parts I and II," B.S.T.J., *42* (July-August 1973), pp. 843-886.
17. J. S. Cook, "Minimum Impulse Response in Ideal Graded-Index Fibers," private communication.

An Experimental Optical-Fiber Link for Low-Bit-Rate Applications

By W. M. MUSKA

(Manuscript received July 15, 1976)

The design, construction, and performance of a practical optical link with interface circuits for coding and decoding 1.5-Mb/s, bipolar, digital signals are described. The optical devices used are light-emitting diodes and PIN photodiodes. A feedback or "transimpedance" preamplifier that incorporates a silicon junction-field-effect transistor is used in the receiver, which has a sensitivity of -57.2 dBm average optical power for a 10^{-9} bit-error-rate. The receiver demonstrates an optical power dynamic range of about 28 dB without requiring automatic gain control. Timing recovery is accomplished by a simple, conventional technique.

I. INTRODUCTION

Experimental repeaters for regenerating digital signals from a few Mb/s to a few hundred Mb/s for optical-fiber transmission have been reported.¹⁻⁷ In this paper, we report the results of an experiment in which a practical optical repeater of simple design and high performance with interface circuits for coding and decoding 1.5-Mb/s bipolar signals was constructed and evaluated. Such a low bit rate, bipolar, digital format (DS1) is presently used in telephone systems for the transmission of multiplexed, digitally encoded voice signals over copper twisted pairs. The optical system was designed to be transparent to the bipolar format of these electrical signals. It utilizes a directly modulated light-emitting-diode (LED) source and a PIN photodiode, incorporates a simple timing recovery circuit, and demonstrates receiver sensitivity that approaches theory.

The bipolar format consists of "zeros" and 50-percent duty cycle alternating positive and negatives "ones"; it, therefore, has three levels with a zero dc component. A straightforward scheme to translate the bipolar format to a unipolar format without increasing the bit rate might involve simple full-wave rectification. However, this is unacceptable in

practice because violation of the bipolar format is used in system maintenance functions as an indication of system performance.

If the bipolar signal is transmitted as a three-level optical signal rather than a binary signal at the bipolar bit rate, 3 dB more average optical power would be required at the receiver detector for a given error-rate (assuming a thermal-noise dominated receiver). Implementing the three-level system would be more difficult, due to the nonlinearity of the LED. The three-level system also requires separate regenerators in the receiver for +1 and -1 pulse regeneration. If the bipolar signal is coded in a two-bit-for-one-bit manner (twice the bit rate), the receiver sensitivity would suffer a degradation of about 4.5 dB (PIN photodiode with FET amplifier input device)⁸ compared to a binary format system at the bipolar bit rate. Although this system is about 1.5 dB less sensitive than the three-level system, repeater circuitry is simplified since the effects of LED nonlinearity are not important and only one pulse regenerator is required.

More efficient coding schemes are possible (e.g., 3-bit for 2-bit)⁹ that allow the bipolar information to be transmitted at less than twice the information bit rate; however, the circuitry required to implement these schemes is substantially more complicated.

The simple coding format^{9,10} used in our experiment is shown in Fig. 1. A positive one is coded into two consecutive 3-Mb/s ones (non-return-to-zero in this case) within a coding frame, a zero is coded as a one followed by a zero within a coding frame (this assignment is arbitrary; it could be 0, 1, instead), and a -1 is coded as two consecutive zeros. This coding format maintains desirable features of the bipolar signal, such as dc balance and substantial redundancy for error correction or monitoring. In addition, the code allows a receiver that is ac-coupled to have a constant threshold level at zero volts for a large range in received power level without automatic gain control. The pulse-transition density of the coded signal is very high, thus allowing a timing-recovery circuit in the receiver that is less critical than those encountered in more conventional binary systems.

The optical system is designed around an LED light source and a PIN photodiode. These devices are expected to be less expensive and require less control circuitry than lasers or avalanche detectors.

II. DESCRIPTION

A unidirectional optical-fiber link is shown in Fig. 2. The coder-transmitter converts the 1.5-Mb/s incoming bipolar signal into a 3-Mb/s unipolar optical signal for transmission via optical fibers. At the receiving terminal, the optical signal is regenerated and decoded back to the 1.5-Mb/s bipolar format. Depending upon the distance between terminals, one or more line repeaters may be needed. A line repeater might

CODING TABLE		
BIPOLAR	ENCODED	UNIPOLAR
	τ_1	τ_2
+1	1	1
0	1	0
-1	0	0

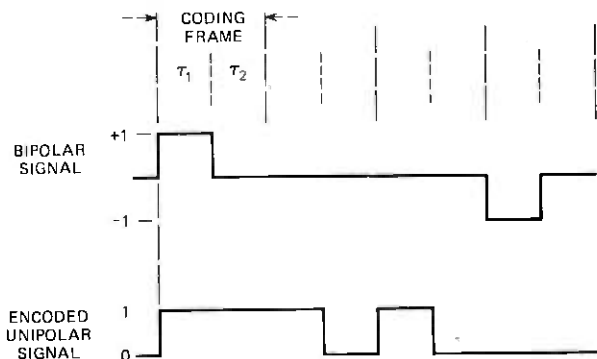


Fig. 1—Coding format.

include the receiver and driver shown in Fig. 2. and a simple regenerator since there is no need to decode or encode the unipolar signal.

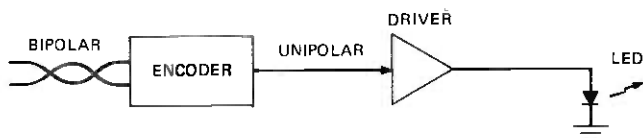
2.1 Coder-transmitter

The circuits between the incoming electrical bipolar signal and the optical fiber consist of a bipolar-to-unipolar converter, a driver for the LED, and the LED. The bipolar signal is coupled to the converter by a transformer with a center-tapped secondary. Each half of the secondary is half-wave rectified; one rectifier generates a pulse when a "plus-one" appears at the input and the other generates a pulse when a "minus-one" appears at the input.

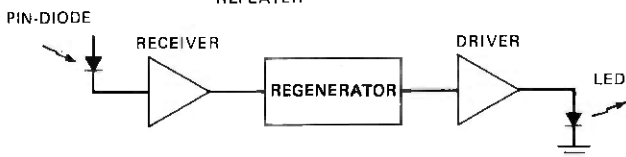
These outputs are then encoded into the 3-Mb/s format by TTL circuitry realized in two dual-in-line packages. The encoding process requires a clock signal, which is obtained from a timing-recovery circuit similar to that used in conventional digital repeaters.¹¹

The digital output voltage of the converter is converted into 220-mA peak current pulses, which directly modulate the Burrus-type, diffused junction LED. A non-return-to-zero format is used since these LEDs are basically peak-power limited and the tolerable repeater span increases with average power when fiber-delay distortion is negligible.⁸ The bandwidth of these devices is more than adequate for this bit rate.

CODER-TRANSMITTER



REPEATER



RECEIVER-DECODER

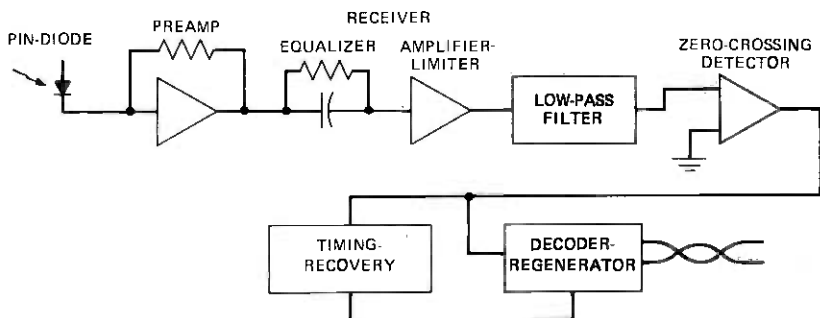


Fig. 2—Electronics of the optical-fiber link.

2.2 Receiver-decoder

The receiver and decoder-regenerator converts the unipolar signal on the optical fiber to a bipolar electrical signal. The input fiber is coupled to a PIN photodiode, which converts the optical pulses to electrical pulses which are then amplified sufficiently to be processed. The sensitivity of the receiver is determined by the thermal and shot noise generated in the "front-end" amplifier and the quantum efficiency and shot noise of the PIN photodiode. It has been shown that the total noise of the amplifier and diode may be referred to the input of the amplifier as a shunt current generator.¹² In the receiver described, the dominant source of noise is the silicon junction-field-effect transistor (Si JFET) input device since the leakage-current shot noise for most PIN photodiodes with active-area diameters less than 1.25 mm is small enough to be neglected. The mean-square current of the effective input noise current generator has been shown to be¹²

$$n_i = 4kTf_b \left[\left(\frac{1}{R_r} + \frac{\Gamma}{g_m R_r^2} \right) I_0 + \frac{(2\pi f_b C_T)^2 \Gamma}{g_m} I_2 \right],$$

where

k = Boltzmann's constant

T = absolute temperature

f_b = bit rate = 3 MHz

g_m = transconductance of the FET ≈ 5 mA/V

$C_T = C_{\text{diode}} + C_{\text{stray}} + C_{\text{in FET}} \approx 8$ pF

R_r = parallel equivalent resistance at the input to the FET
(diode bias return, FET bias, etc.)

$\Gamma \approx 0.7$ for typical Si JFETs.

The parameters I_0 and I_2 are weighting factors, which are determined by optical input and amplifier output pulse shapes;¹² in this case the input pulse is NRZ and rectangular and the output pulse NRZ and raised cosine; therefore,

$$I_0 = 0.55$$

$$I_2 = 0.085.$$

If the amplifier input device is an FET, it is possible to choose a value for R_r , such that the term associated with I_0 is negligible compared to the term associated with I_2 , in which case an FET should be chosen to maximize $\sqrt{g_m}/C_T$.

The above analysis is for a non-feedback amplifier, which has an input time constant much larger than the signal period, $1/f_b$. In the present work, a "transimpedance" or feedback amplifier is used. Here, the output voltage is

$$e_o = -I_s Z_f \left(\frac{A\beta}{A\beta + 1} \right),$$

where

I_s = photodiode signal current

Z_f = feedback impedance = $1/(1/R_f + j\omega C_f)$

C_f = total shunting capacitance across R_f

R_f = feedback resistance

A = open-loop amplifier voltage gain

$\beta = Z_{in}/(Z_{in} + Z_f)$

Z_{in} = total impedance at the input of the open-loop amplifier

It can be shown that the feedback resistor R_f plays the same role as R_r in relation to noise.

Since, in this case, C_f is about $(1/80)C_t$, the time constant $R_f C_f$ is $1/80$ that of $R_r C_t$ in the non-feedback design, and the signal is integrated over far fewer signal periods. There must be sufficient linear gain before pulse shape restoration, so that the amplifier following equalization does not affect the signal-to-noise ratio. In the case of the non-feedback amplifier, the integrated peak output voltage excursion may be many times that for a single pulse, in which case the optical power dynamic range of the amplifier is limited. The transimpedance amplifier, on the other hand, does not experience this problem, thus allowing a substantially greater dynamic range.

Following the pulse equalizer, the signal is further amplified by an amplifier that is linear at very low input power levels but acts as a symmetrical limiter at higher received optical power levels without degrading the performance. This feature eliminates the need for an automatic gain control.

The signal is bandlimited by a third-order Butterworth filter to reduce high-frequency, out-of-band noise, and then threshold detected by a zero-crossing detector.

Due to the coding format, the dc component of the received electrical signal voltage is always one-half the peak, thus the proper threshold level at the threshold detector is always zero when ac coupling is used at the input of the threshold detector.

The signal at the output of the zero-crossing detector, which has been quantized into two discrete voltage levels, has timing-jitter due to the presence of noise. This jitter is removed, as shown in Fig. 3, by sampling the signal at times which are determined by a 1.5-MHz, low-noise clock signal, which is recovered from the received signal by a high-Q, parallel-resonant circuit. This circuit is sustained in oscillation by 3.3-microsecond pulses, which are generated by a monostable multivibrator whenever a zero-one transition occurs in the received signal (Fig. 3, waveforms A-C). Since a zero-one sequence in the encoded signal only occurs at the beginning of a coding frame, the clock is synchronized with the frames. The 3-Mb/s received signal is demultiplexed into two 1.5-Mb/s signals by two sample and store circuits, one of which samples the first bit in a coding frame on positive-going clock transistions (Fig. 3, waveform D), and the other samples the second bit in a frame on negative-going clock transistions (Fig. 3, waveform E). These two 1.5-Mb/s signals are then reconstituted into the original DS1 (1.5-Mb/s, 50-percent duty-cycle, bipolar) signal by comparing the states of the two demultiplexed signals at the end of each coding frame (Fig. 3, waveform F). Pulse regeneration and decoding to bipolar is accomplished with TTL circuits.

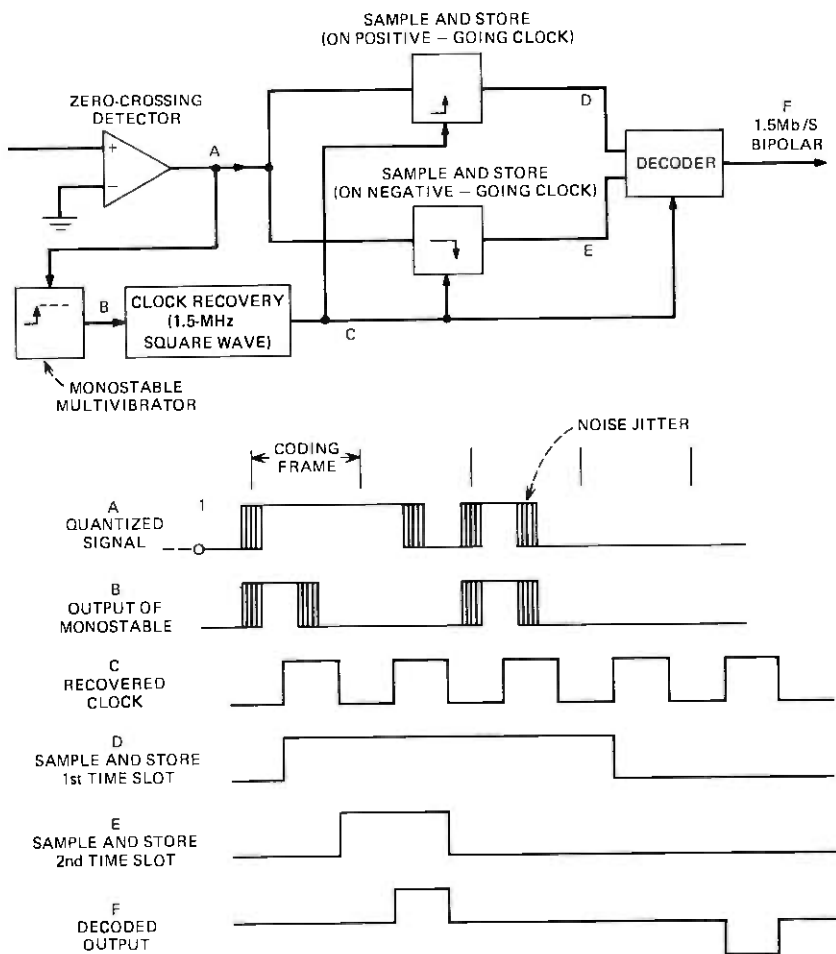


Fig. 3—Decoding process.

consisting of 3 D-type flip-flops, 3-2 input NAND gates, and an inverter. The output of the decoder is coupled to a twisted pair line.

III. SYSTEM PERFORMANCE

3.1 Evaluation procedure

To evaluate the system error performance, dynamic range, and timing jitter, the coder-transmitter and the receiver-decoder were physically separated and optically coupled through an air path into which the required amount of attenuation was placed. The two sections were then packaged in a plug-in module of dimensions, $1\frac{5}{16}$ inches \times $8\frac{1}{2}$ inches \times

9 inches, and optically coupled via an optical-fiber path into which a controlled amount of attenuation was placed. No degradation in performance was observed.

3.2 Error performance

The theoretical average optical power required for a given error probability is¹²

$$P = \frac{h\nu}{\eta e} Q n_t^{1/2},$$

where

P = average optical power required to produce an error probability of P_e

h = Planck's constant

ν = optical frequency

η = photodiode quantum efficiency

e = electron charge

$Q = \sqrt{2} \operatorname{erfc}^{-1}(2P_e)$

P_e = probability of error.

The photodiode used in the error probability measurements had a quantum efficiency of about 65 percent.

The theoretical and experimental error probability curves are presented in Fig. 4. The 0.5-dB discrepancy is due to noise contributions of amplifier stages following the FET input stage and measurement errors. The data point at the 1.4×10^{-9} rate was obtained by counting the errors that occurred in 12 time periods of 10^9 time slots each (≈ 5 min.). During one of these periods, a burst of 30 errors occurred due to electromagnetic interference and the data obtained during this period were omitted.

The curves in Fig. 4 indicate the error probability at the coded 3-Mb/s rate, the error probability at the 1.5-Mb/s rate would be about a factor of two higher (some error correction takes place in the decoder); however, this increase could be compensated for with about a 0.2 dB increase in optical power.

3.3 Dynamic range

Optical power dynamic range is described as

$$P_d(\text{dB}) = P_{\max}(\text{dB}) - P_{\min}(\text{dB}),$$

where

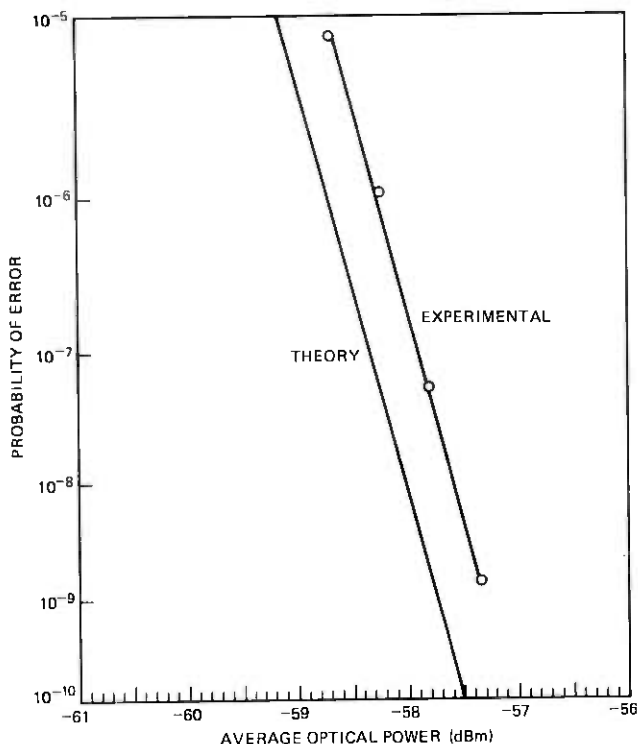


Fig. 4—Experimental and theoretical error vs. received average optical power.

P_{max} = maximum received optical power level before nonlinear effects degrade performance.

P_{min} = optical power required to maintain a 10^{-9} error probability.

The optical power dynamic range for the receiver described here is about 28 dB.

3.4 Timing jitter

The phase jitter in the decoded pulse stream was observed to be about 10 degrees RMS at a received optical power level of about -57.8 dBm.

3.5 Waveforms

The oscilloscope pictures in Fig. 5(a-e) show waveforms at several points in the system at various input power levels. The "eye diagram" in Fig. 5(a) is taken at the output of the "front-end" amplifier and illustrates the signal integration due to the capacitance across the feedback resistor. Fig. 5(b) and (c) were taken at the input to the filter, Fig. 5(b)

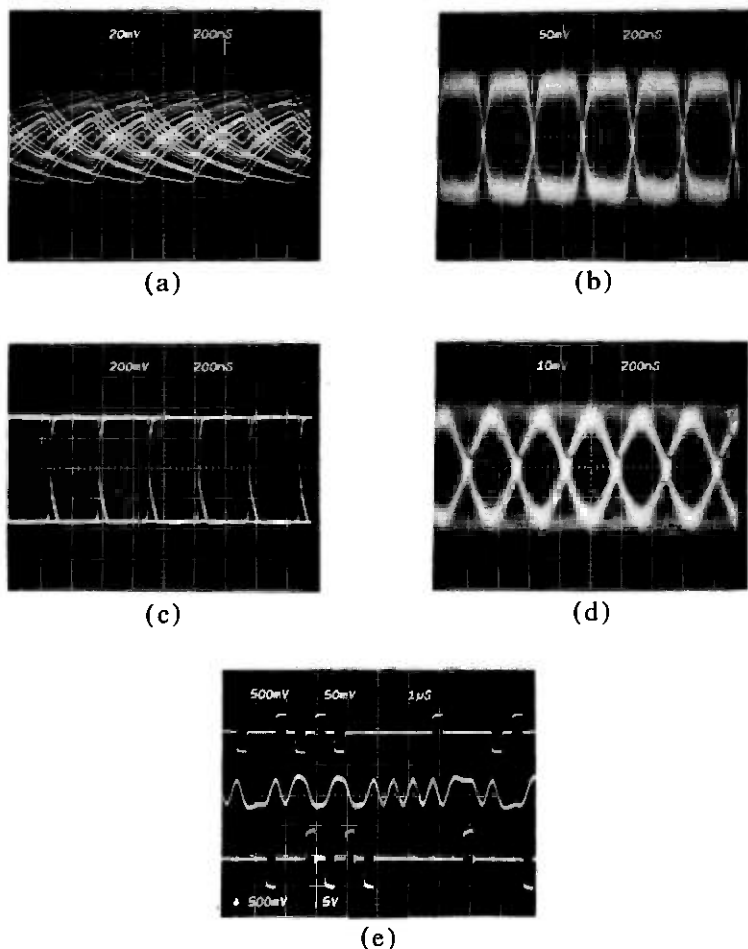


Fig. 5—Receiver waveforms (voltages: $0.1 \times$ actual value)

was taken at a received optical power level of -47 dBm, and Fig. 5(c) was taken at an optical power level of -28 dBm when the second amplifier acts as a limiter.

Figure 5(d) demonstrates the “eye,” after filtering, at a -57.2 dBm optical power level. The waveforms from top to bottom in Fig. 5(e) are: the bipolar signal at the input to the coder-transmitter, the 3-Mb/s received signal at the output of the filter, and the regenerated and decoded bipolar signal.

Power consumption

Total power consumption for the transmitter and receiver was about 1.75 watts.

IV. SUMMARY

A practical optical-fiber link of simple design for faithful transmission of 1.5-Mb/s bipolar, digital signals has been built and tested. High performance is achieved through the use of a transimpedance preamplifier that affords receiver sensitivity that approaches the theoretical limits imposed by commercially available silicon junction-field-effect transistors.

REFERENCES

1. J. E. Goell, "An Optical Repeater with High-Impedance Input Amplifiers," *B.S.T.J.*, 53, No. 4 (April 1974), pp. 629-643.
2. P. K. Runge, "A 50 Mb/s Repeater for a Fiber Optic PCM Experiment," *Proceedings of ICC*, 1974, 17B-1-3.
3. J. E. Goell, "A 274 Mb/s Optical-Repeater Experiment Employing a GaAs Laser," *Proc. IEEE*, (October 1973), pp. 1504-1505.
4. Y. Ueno and Y. Ohgushi, "A 40 Mb/s and a 400 Mb/s Repeater for Fiber Optic Communications," *IEEE J. Quantum Electron.*, QE-11, (September 1975), pp. 78D and 79D.
5. R. W. Blackmore and P. H. Fell, "8.448 Mbits Optical Fibre System," *IEE Conf. Pub. No. 132, First European Conference on Optical Fibre Communication* (September 16-18, 1975), pp. 182-183.
6. K. Kurokawa, T. Sekizawa, T. Kudo, T. Toge, and Y. Nagai, "A 400 Mb/s Experimental Transmission System Using a Graded Index Fiber," *IEE Conf. Pub. No. 132, First European Conference on Optical Fibre Communication* (September 16-18, 1975) pp. 159-161.
7. J. Yamagata, S. Senmoto, Y. Inamura, H. Kaneko and T. Takahashi, "A 32 Mb/s Regenerative Repeater for Fibre Cable Transmission," *IEE Conf. Pub. No. 132, First European Conference on Optical Fibre Communication* (September 16-18, 1975), pp. 144-146.
8. S. D. Personick, "Receiver Design for Digital Fiber Optic Communication Systems, I and II," *BSTJ*, 52, No. 6, (July-August, 1973), pp. 843-875.
9. J. S. Cook, S. D. Personick, and D. D. Sell, private communication.
10. Y. Takasaki, M. Tanaka, N. Maeda, K. Yamashita, and K. Nagano, "Optical Pulse Formats for Fiber Optic Digital Communications," *IEEE Trans. on Commun.*, COM-24, No. 4 (April 1976), pp. 404-413.
11. J. S. Mayo, "A Bipolar Repeater for Pulse Code Modulation Signals," *BSTJ*, 41, No. 1, (January 1962) pp. 59-66.
12. J. E. Goell, "Input Amplifier for Optical PCM Repeaters," *BSTJ*, 53, No. 9, (November 1974), pp. 1771-1793.

Propagation of High-Frequency Elastic Surface Waves Along Cylinders With Various Cross-Sectional Shapes

By J. A. MORRISON, J. B. SEERY, and L. O. WILSON

(Manuscript received March 24, 1976)

Elastic surface waves, or Rayleigh waves, are disturbances that travel over the stress-free surface of an elastic solid, and whose amplitudes decay rapidly with depth into the solid. Earlier mathematical results are used to study numerically the properties of these waves on specific cylindrical objects that might be used as acoustic topographic waveguides. The lowest-order mode is investigated for cylinders with strictly nonconstant curvature. Mode confinement and its dependence on such things as cylinder shape and the value of the frequency parameter are studied. Phase and group velocities are also computed. Mode behavior is studied in the transition region between the case of cross-sectional boundary curves of nonconstant (and not "almost" constant) curvature, for which the modes are localized, and the case of constant curvature, for which they are not localized. Some higher-order modes are investigated for the rounded wedge.

I. INTRODUCTION

Elastic surface waves, or Rayleigh waves, are disturbances that travel over the stress-free surface of an elastic solid, and whose amplitudes decay rapidly with depth into the solid. In a series of earlier papers,¹⁻³ we developed and applied some mathematical techniques to describe the propagation of high-frequency elastic surface waves along cylinders of general cross section. Our intent was to learn more about the properties of such waves traveling down cylindrical objects that might be used as acoustic topographic waveguides. In this paper, we use our earlier mathematical results to study numerically the properties of elastic surface waves on certain specific cylindrical objects of interest. We treat

cylinders roughly corresponding to an elliptical bore, an elliptical rod, a wedge with a rounded tip, and a flat plane with a rounded ridge on it. The elastic medium is assumed to be homogeneous and isotropic.

The earlier papers discussed two approximate high-frequency descriptions of the surface-wave behavior: an asymptotic approximation and one which we termed a surface-wave approximation. The analysis involved a scalar wave equation, a vector wave equation, and rather complicated boundary conditions. Since the analysis was cumbersome, a simpler scalar "model problem" was first investigated by Morrison.¹ The techniques he developed had counterparts in the full elastic problem, which was treated by Wilson and Morrison² in the high-frequency asymptotic approximation, designated by A (as depicted in Fig. 1). The lowest-order surface-wave mode was investigated in almost as much detail as that for the scalar problem, but because of the algebraic complexities, the higher-order modes were less completely analyzed.

For the scalar problem,¹ Morrison had also obtained a surface-wave approximation describing the high-frequency behavior of the surface-wave modes. He then derived the analogous approximate equations for the high-frequency behavior of the elastic surface-wave modes.³ Unlike

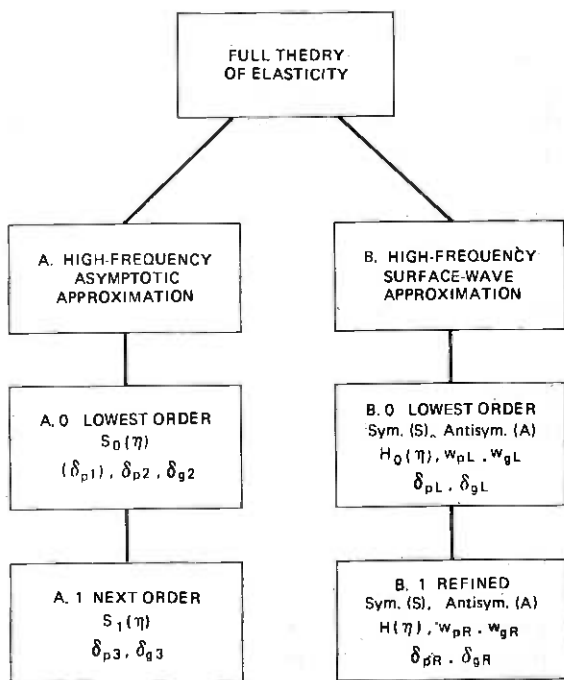


Fig. 1—High-frequency approximation chart.

the asymptotic approximation, A in Fig. 1, the surface-wave approximation, designated by B in Fig. 1, was capable of describing the mode behavior at high frequencies in the transition region between the case of cross-sectional boundary curves of nonconstant (and not "almost" constant) curvature, for which the modes are localized, and the case of constant curvature, for which they are not localized. (The asymptotic approximations had required boundary curves with strictly nonconstant curvature.) Also, this description gave a more complete analysis of the higher-order modes.

In Section II, we exhibit the cross-sectional boundary curvature functions used in our numerical investigations and explain why we chose those specific functions.

Section III is devoted to a numerical treatment of the high-frequency asymptotic results. The lowest-order mode is investigated for cylinders with strictly nonconstant curvature. We learn about the phenomenon of mode confinement, and its dependence upon such things as the shape of the cylinder and the value of the high-frequency parameter χ used in the asymptotic expansions, A in Fig. 1. We also compute the phase and group velocities.

In Section IV we make a similar investigation using the surface-wave approximation, B in Fig. 1. When possible, the results are compared with the asymptotic results. Particular attention is paid to the mode behavior in the transition region described earlier, and to the behavior of higher-order modes. We also compare our results with exact theoretical results for the circular bore.⁴

In Section V, we summarize our findings.

II. THE BOUNDARY CURVES

We wished to investigate numerically the properties of disturbances propagating along the surfaces of various cylindrical objects. The motivation for our particular choices of cross-sectional boundary curves came from our earlier high-frequency asymptotic results,² which could be applied to a cylinder with an open boundary curve whose curvature attains its algebraic maximum at a single point, and which could also be applied to a cylinder that has a closed boundary curve which is symmetric and whose curvature attains its algebraic maximum at two points. We decided to consider disturbances propagating along objects roughly corresponding to an elliptical bore, an elliptical rod, a wedge with a rounded tip, and a flat plane with a rounded ridge on it.

The exact forms of the chosen boundary curvature functions were suggested by the analytical form of the displacement function obtained in our high-frequency asymptotic results.² The high-frequency behavior of the disturbance can be determined in the vicinity of the cylinder

surface. As is shown in Appendix A, the disturbance corresponding to the zeroth-order mode, when evaluated at the surface of the cylinder, can be expressed as

$$\frac{c_T e^{i(\beta z - \omega t)}}{\omega b^{(0)}(0)} \mathbf{u}(\Xi, \eta) |_{\Xi=0} = F(\eta) \exp[-(P\chi)^{1/2} G(\eta)] \left(\left[\frac{(b^2 + a_T^2)}{2a_T} - a_L \right] \left[1 + \frac{C(\eta)}{2(P\chi)^{1/2}} \right] \mathbf{n} - \left[1 - \frac{(b^2 + a_T^2)}{2b^2} \right] \left\{ \left(\frac{P}{\chi} \right)^{1/2} I(\eta) \mathbf{t} + ib \left[1 + \frac{C(\eta)}{2(P\chi)^{1/2}} \right] \mathbf{k} \right\} \right). \quad (1)$$

Here u is the displacement, β is the propagation constant, z measures distance along the generators of the cylinder, ω is the frequency, and t is the time. A right-handed coordinate system is used, with unit vectors \mathbf{n} , \mathbf{t} , and \mathbf{k} in the directions of the inward normal, tangent to the cross-sectional boundary curve, and along the generators of the cylinder, respectively. Here $\Xi = n/\ell$, where n represents distance from the surface along the inward normal and ℓ is a characteristic length; also $\eta = s/\ell$, where s is signed arc length along the boundary curve. The normalized unit of length, corresponding to the characteristic length ℓ , is depicted in Figs. 2, 3, and 4 for the particular cross-sectional boundary curves considered. The quantities b , a_T , a_L , and P are constants defined in Appendix A, and $b^{(0)}(0)$ is a normalization constant. We have

$$\chi = \omega\ell/c_T \gg 1, \quad (2)$$

where c_T is a constant representing the transverse wave velocity of the medium. Thus, the parameter χ is proportional to the frequency ω and is assumed to be large. The functions $C(\eta)$, $F(\eta)$, $G(\eta)$, and $I(\eta)$ all involve the curvature function $K(\eta) = \ell\kappa(s)$; as is shown in Appendix A, $C(\eta)$, $F(\eta)$, and $G(\eta)$ are defined as integrals of certain functions of the curvature function. It was to evaluate these integrals and the integral of the curvature function analytically that we chose the specific curvature functions.

The boundary curves are then given by the functions $X(\eta)$ and $Y(\eta)$ defined by⁵

$$\begin{aligned} \frac{dX}{d\eta} &= \cos \int_0^\eta K(\zeta) d\zeta, \\ \frac{dY}{d\eta} &= -\sin \int_0^\eta K(\zeta) d\zeta. \end{aligned} \quad (3)$$

To describe an ellipse-like bore, we set

$$K_1(\eta) = -1 + 2k \cos 2\eta, \quad 0 \leq k \leq 1/2, \quad (4)$$

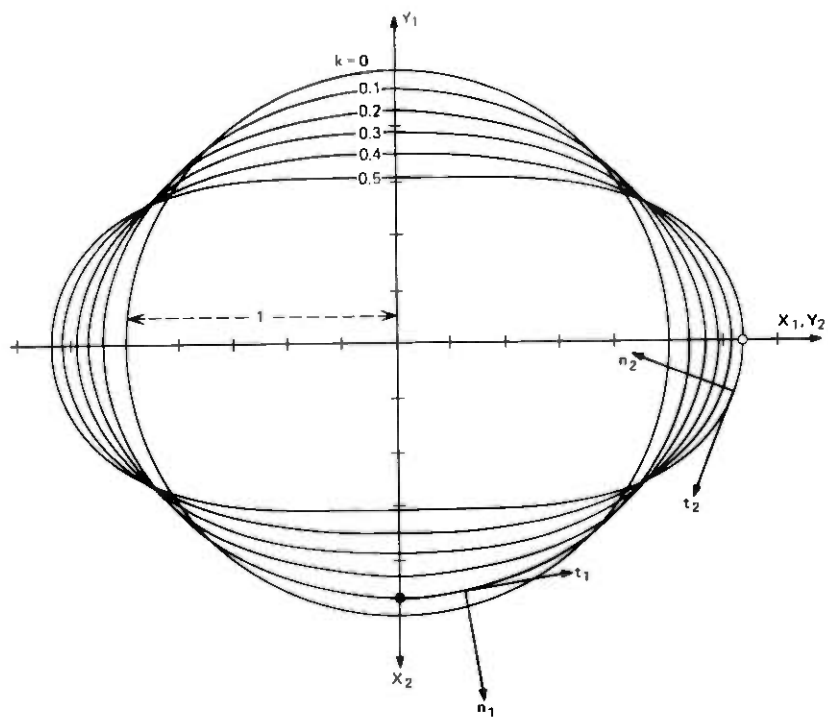


Fig. 2—Boundary curves corresponding to the ellipse-like bore and rod for various values of k .

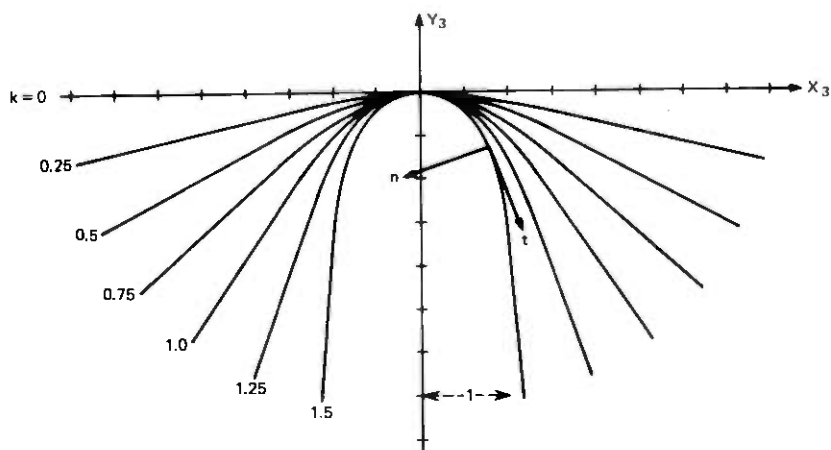


Fig. 3—Boundary curves corresponding to the rounded wedge for various values of k .

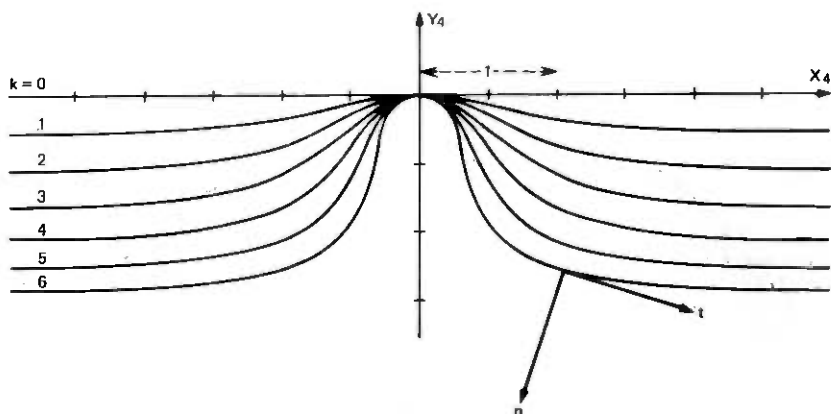


Fig. 4—Boundary curves corresponding to the ridged plane for various values of k .

while

$$K_2(\eta) = 1 + 2k \cos 2\eta, \quad 0 \leq k \leq \frac{1}{2} \quad (5)$$

corresponds to an ellipse-like rod. Equations (4) and (5) actually describe the same boundary curve with circumference $2\pi\ell$. Notice that in both instances $\eta = 0$ corresponds to a point of maximum algebraic curvature. Also, the curvature is negative for the bore, because of our convention that \mathbf{n} is directed into the region. The curvature function

$$K_3(\eta) = k \operatorname{sech}^2 \eta, \quad 0 \leq k \leq \pi/2 \quad (6)$$

corresponds to a wedge-like object similar to a hyperbolic cylinder. Finally,

$$K_4(\eta) = k[\epsilon^2 - \tanh^2 \eta (\operatorname{sech}^2 \eta + \epsilon^2)], \quad \epsilon = \frac{1}{3} \left(1 + \sqrt{\frac{11}{5}} \right) \quad (7)$$

describes a rounded ridge on a plane. The value for ϵ is found from the condition $\int_0^\pi K(\eta) d\eta = 0$. As with the other cases, there is also a restriction on k . It is complicated so we do not write it here. In each case, k is a parameter that can be varied.

The boundary curves corresponding to the curvature functions in (4) to (7) were obtained numerically. In Fig. 2, we show the boundary curves corresponding to the ellipse-like bore and rod for various values of k . The unit of length is indicated in the figure. Notice that $k = 0$ corresponds to a circular bore or rod. The dot represents the point $\eta = 0$ for the bore corresponding to $k = 0.1$, indicating that the points of maximum curvature lie on the Y_1 axis. For the bore, the vectors \mathbf{n}_1 and \mathbf{t}_1 indicate the directions of the normal into the region and the tangent to the curve.

Similarly, the circle represents the point $\eta = 0$ for the rod corresponding to $k = 0.5$, indicating that the points of maximum curvature lie on the Y_2 axis. Note that the axes for the rod have been rotated by 90 degrees from those for the bore. For the rod, the vectors \mathbf{n}_2 and \mathbf{t}_2 indicate the directions of the inward normal and the tangent to the curve. In Figs. 3 and 4, we show the boundary curves for the rounded wedge and ridged plane, respectively, for various values of k . The unit of length is indicated, as are the unit vectors \mathbf{n} and \mathbf{t} .

At high frequencies, the asymptotic result (1) does not hold in the transition region between the case of cross-sectional boundary curves of nonconstant (and not "almost" constant) curvature, for which the modes are localized, and the case of constant curvature, for which they are not localized. However, a refined surface-wave approximation equation, to be discussed in Section IV, does give results in this transition region.

III. ASYMPTOTIC RESULTS

In this section, we present high-frequency asymptotic results based on evaluation of (1) for the bore, rod, wedge, and plane with a ridge. In each case, the results are for the fundamental, or zeroth-order, mode. The bore and the rod have closed boundary curves which are symmetric, and for which the curvature attains its algebraic maximum at two points. For such cylinders, the expansion (1) corresponds to two modes, the zeroth-order symmetric one and the zeroth-order antisymmetric one, for which the values of the propagation constant β differ by only an exponentially small amount.^{1,2} This expansion is about the point of maximum algebraic curvature at $\eta = 0$ and is valid for $|\eta| < \pi/2$. There is an analogous expansion about the point of maximum algebraic curvature at $\eta = \pi$ which is valid for $|\eta - \pi| < \pi/2$. Each expansion is not expected to be precise in regions where the disturbance is very small and the two modes differ. It is necessary to ensure that the disturbance is confined to regions near points of maximum algebraic curvature so that it is indeed small where the two modes are known to differ. From (1), (29), (33), and (35), this can be viewed as a requirement that the frequency parameter χ be sufficiently large and that the deviation of the curvature from a constant value not be small.

Equation (1), which is valid on the surface of the cylinder, was obtained from (39) in Appendix A, which holds also near the surface. In the derivation of the latter equation, it was necessary to assume that if the center of curvature for a point on the cross-sectional boundary curve lies *within* the region defining the cylinder, then the disturbance must be negligible at that point. This means that for the rod, wedge, and ridged plane, the results are applicable only if the frequency is high enough that the disturbance is confined close to the surface of the cylinder. Mathe-

matically, this means that each exponential term in (39) must be very small when evaluated at the value of Ξ corresponding to the minimum radius of curvature. These conditions result in an approximate lower bound on the frequency parameter χ , namely that

$$\chi \geq 10 K(0)/a_T. \quad (8)$$

The constant a_T depends upon the Poisson ratio σ . For values of σ between 0 and $1/2$, it turns out that a_T ranges between 0.56 and 0.31, respectively. Most of our numerical results were obtained with $\sigma = 0.16974$, which was taken as the Poisson ratio for fused silica.⁶ For this value of σ , we have $a_T = 0.47$.

As can be seen from (1), the \mathbf{n} and \mathbf{k} components of the displacement $u_n(0, \eta)$ and $u_k(0, \eta)$ each contain a factor $[1 + \frac{1}{2}C(\eta)(P\chi)^{-1/2}]$, whereas the \mathbf{t} component $u_t(0, \eta)$ contains a factor $I(\eta)(P\chi)^{1/2}$. Then, in the lowest-order asymptotic approximation, A.0 in Fig. 1, the \mathbf{t} component of the displacement does not even appear. To this order, the solution is like that for Rayleigh waves traveling on the surface of a plane infinite half space except that it is multiplied by a factor that describes the confinement of the disturbance due to the cylinder curvature. In the next-order asymptotic approximation, A.1 in Fig. 1, the effect is to multiply this solution by an additional factor and to add a \mathbf{t} component of displacement. Since it turns out computationally that u_t is a few percent of the size of u_n or u_k , we shall concentrate our attention on u_n and u_k . Since these two components are proportional to each other, it suffices to treat the quantities

$$S_0(\eta) = F(\eta) \exp[-(P\chi)^{1/2}G(\eta)], \quad (9)$$

$$S_1(\eta) = S_0(\eta)[1 + \frac{1}{2}C(\eta)(P\chi)^{-1/2}], \quad (10)$$

which are proportional to the \mathbf{n} and \mathbf{k} displacement components in the lowest-order and next-higher-order asymptotic approximations, A.0 and A.1, respectively, and which are normalized to unity at $\eta = 0$. We shall mostly discuss the more accurate approximation $S_1(\eta)$.

Figures 5 and 6 illustrate some results obtained for the ellipse-like bore whose cross-sectional curvature function is given by (4). Because of the symmetries of the boundary curve, it is only necessary to consider values of η between 0, which corresponds to a point of maximum algebraic curvature, and $\pi/2$, which corresponds to a point one quarter of the way around the curve. In both figures, we plot the first-order asymptotic approximation $S_1(\eta)$ from $\eta = 0$ to a value of η less than $\pi/2$ for which the disturbance is relatively small.

In Fig. 5, we show $S_1(\eta)$ for several values of the frequency parameter χ . The constant k in (4) was chosen to be 0.5; the Poisson ratio was chosen to be 0.16974, corresponding to fused silica. If we take the transverse wave

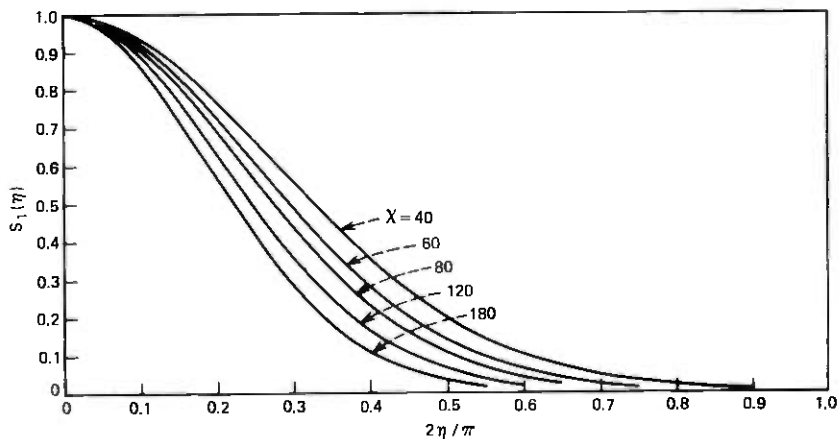


Fig. 5—First-order asymptotic approximation $S_1(\eta)$ for the bore, with $k = 0.5$, plotted as a function of η for various values of the frequency parameter χ and Poisson ratio $\sigma = 0.16974$.

velocity for fused silica to be 3764 m/s, then for $\ell = 3 \times 10^{-4}$ m the frequency corresponding to $\chi = 40$ is approximately 80 MHz. It is strikingly apparent that the disturbance is indeed confined to a region near the point of maximum algebraic curvature $\eta = 0$. There is, of course, similar confinement to the region near $\eta = \pi$. Such confinement near a point of maximum algebraic curvature shows up in a similar manner in the computations for rods, wedges, and ridges on planes. We also see that the confinement becomes even more pronounced as the frequency parameter χ increases.

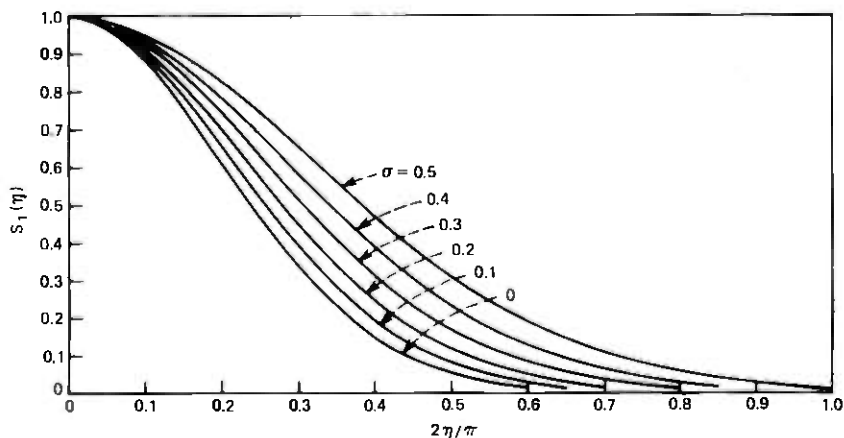


Fig. 6—First-order asymptotic approximation $S_1(\eta)$ for the bore, with $k = 0.5$, plotted as a function of η for frequency parameter $\chi = 80$ and various values of the Poisson ratio σ .

As the ellipse-like bore becomes more like a circular bore (k decreases), the confinement near points of maximum algebraic curvature decreases. This is to be expected since in the limiting case of a perfectly circular bore, there is no such confinement at all. We do not include a figure here to exhibit the way the confinement changes with k , as the effect will be vividly demonstrated later in Section IV where surface waves on "almost" circular bores are discussed.

In Fig. 6, we fix $\chi = 80$ and $k = 0.5$, and show $S_1(\eta)$ for various values of the Poisson ratio σ . The confinement increases as σ decreases.

These results are quite representative of all those we obtained for the bore, rod, wedge, and plane with a ridge. Other curves for $S_1(\eta)$ are qualitatively very similar. For example, in Fig. 7, we show $S_1(\eta)$ for a plane with a ridge on it. In this case, the curvature function is given by (7), with $k = 3$. We fixed $\sigma = 0.16974$ and varied the frequency parameter χ . Because other results are so similar, we do not show any specific curves for the rod or wedge.

We next compare the lowest-order asymptotic approximation $S_0(\eta)$ with the first-order asymptotic approximation $S_1(\eta)$. Here, some distinctions do arise in our computations for the various cylinders. In considering the ellipse-like bore, we find that for values of the parameters in the ranges previously discussed, the curves $S_0(\eta)$ are hardly distinguishable from the curves $S_1(\eta)$. This is not always the case for the rod, wedge, and ridge on a plane. To give an example for which the first-order correction term is significant, we show in Fig. 8 the functions $S_0(\eta)$ and $S_1(\eta)$ corresponding to a rounded wedge, with $\chi = 40$, $k = 1.0$, and $\sigma = 0.16974$. Similar results can be obtained for the rod and the plane with a ridge on it when the frequency parameter χ is in the lower part of the range being considered. In all cases, the first-order correction becomes noticeably smaller as χ is increased. We expect the second-order correction to be negligible.

The normalized phase and group velocities are

$$w_p = \frac{\omega}{\beta c_T}, \quad w_g = \left(c_T \frac{d\beta}{d\omega} \right)^{-1}, \quad (11)$$

where c_T is the transverse-wave velocity. From the asymptotic results,² it is found that

$$w_p = \frac{1}{b} - \frac{d_0 P}{2b^3 \chi} + \frac{(-d_2 P)^{1/2}}{2b^3 \chi^{3/2}} + \frac{(d_0^2 P^2 - 2b^2 Q^2)}{4b^5 \chi^2} + \dots \quad (12)$$

and

$$w_g = \frac{1}{b} - \frac{(-d_2 P)^{1/2}}{4b^3 \chi^{3/2}} + \frac{Q}{2b^3 \chi^2} + \dots, \quad (13)$$

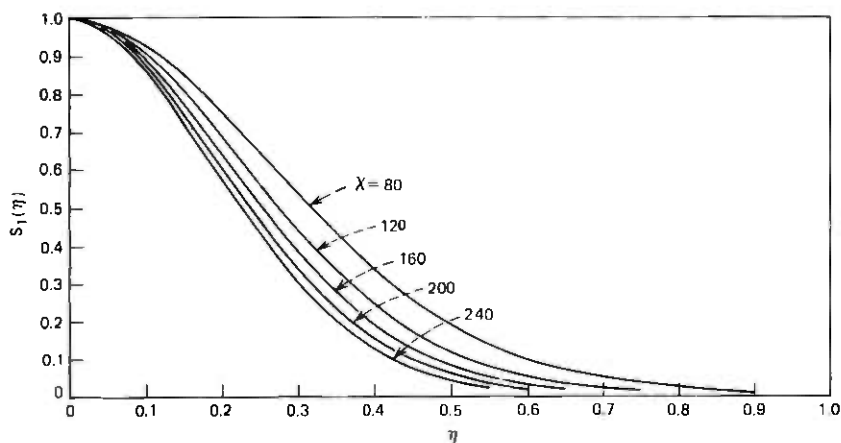


Fig. 7—First-order asymptotic approximation $S_1(\eta)$ for the ridged plane, with $k = 3$, plotted as a function of η for various values of the frequency parameter χ and Poisson ratio $\sigma = 0.16974$.

where the constants b , d_0 , d_2 , P , and Q are defined in Appendix A. In particular, $1/b = c_R/c_T = w_R$ is the normalized Rayleigh wave velocity, and w_R is the solution of equation (24) which satisfies $0 < w_R < 1$. Both the phase and the group velocity asymptotically approach the Rayleigh wave velocity and, consequently, we define the normalized differential phase and group velocities by

$$\delta_p = w_p - 1/b, \quad \delta_g = w_g - 1/b. \quad (14)$$

The asymptotic approximations δ_{p1} , δ_{p2} , and δ_{p3} to δ_p are obtained by retaining terms through orders χ^{-1} , $\chi^{-3/2}$, and χ^{-2} respectively in the

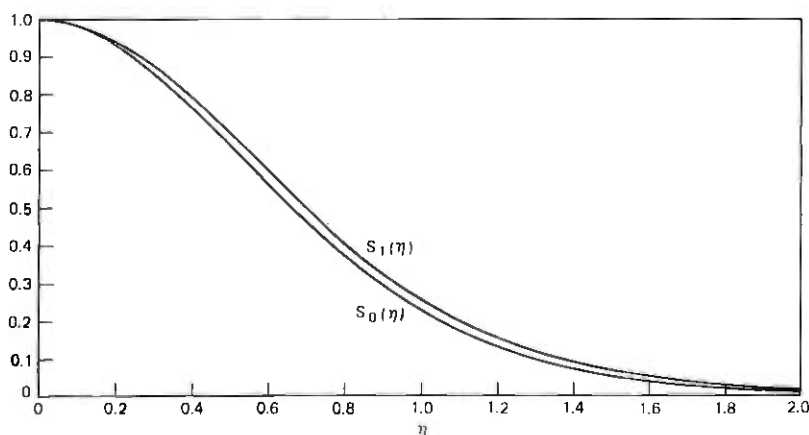


Fig. 8—Comparison of lowest- and first-order asymptotic approximations $S_0(\eta)$ and $S_1(\eta)$ for the rounded wedge, with $k = 1.0$, plotted as functions of η for frequency parameter $\chi = 40$ and Poisson ratio $\sigma = 0.16974$.

expansion (12). Similarly, the approximations δ_{g2} and δ_{g3} to δ_g are obtained by retaining terms through orders $\chi^{-3/2}$ and χ^{-2} respectively in the expansion (13).

In Fig. 9, we show the approximations δ_{p2} and δ_{p3} to the normalized differential phase velocity as a function of the frequency parameter χ for the ellipse-like bore, with $k = 0.5$ and $\sigma = 0.16974$. We do not plot δ_{p1} , as it can be shown to be identically equal to zero for this case. Notice that the convergence is quite good. This is also true for the approximations δ_{g2} and δ_{g3} to the normalized differential group velocity, which are shown in Fig. 10.

For cylinders of other cross-sectional shapes, the convergence is not always so good, particularly for the differential group velocities. In Tables I(a) and I(b), we show δ_{p1} , δ_{p2} , δ_{p3} , and δ_{g2} , δ_{g3} , respectively, for the bore, rod, wedge, and ridged plane; here $\chi = 80$, $\sigma = 0.16974$, and k varies. The convergence improves as χ increases.

In Figs. 11 and 12, we show one additional set of approximations to the differential phase and group velocities, respectively, as a function of χ . Here, the curves are for the wedge, with $k = 1.0$ and $\sigma = 0.16974$.

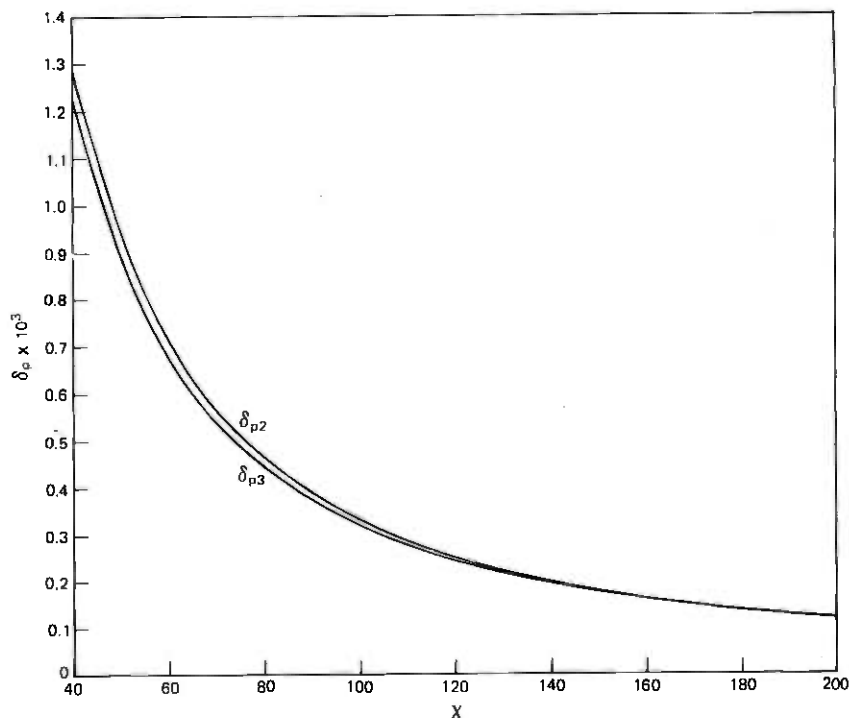


Fig. 9—Asymptotic approximations δ_{p2} and δ_{p3} to the normalized differential phase velocity as a function of the frequency parameter χ for the bore; $k = 0.5$ and Poisson ratio $\sigma = 0.16974$.

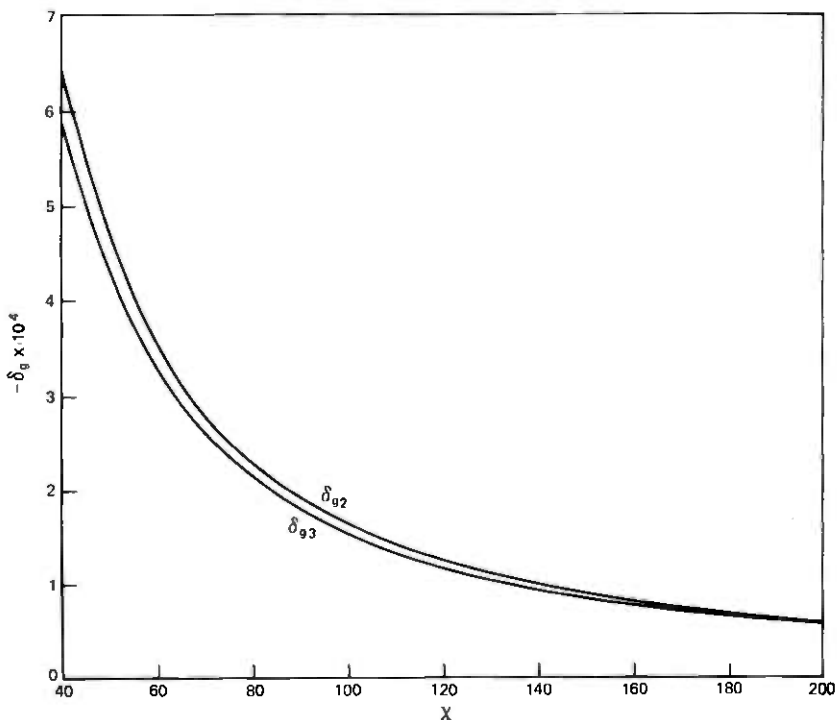


Fig. 10—Asymptotic approximations δ_{g2} and δ_{g3} to the normalized differential group velocity as a function of the frequency parameter χ for the bore; $k = 0.5$ and Poisson ratio $\sigma = 0.16974$.

IV. SURFACE-WAVE APPROXIMATIONS

In this section, we consider two related equations that describe the high-frequency behavior of the surface-wave modes. We call these equations the lowest-order approximate equation and the refined approximate equation. They are subject to the same restrictions about the disturbances being confined near the surface as are the asymptotic equations of Section III which describe the zeroth-order mode. The surface-wave approximations B.0 and B.1 (see Fig. 1) permit a more complete analysis of the higher-order modes. The refined approximation B.1 also describes the behavior of the modes in the transition region, at high frequencies, between the case of cross-sectional boundary curves of nonconstant (and not "almost" constant) curvature, for which the modes are localized, and the case of constant curvature, for which they are not localized.

In the refined surface-wave approximation³ the displacement, when evaluated at the surface of the cylinder, can be expressed in the form

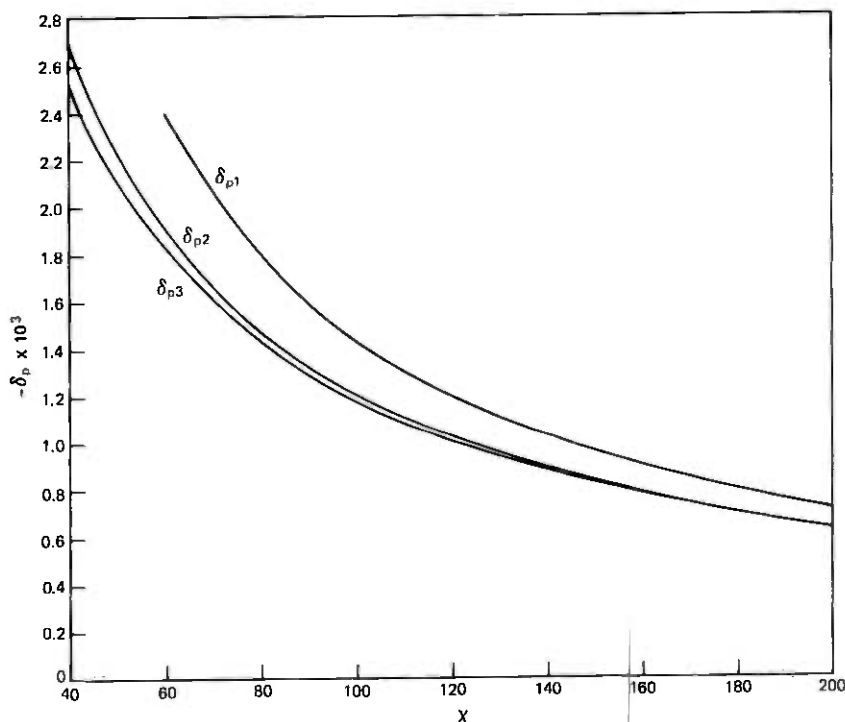


Fig. 11—Asymptotic approximations δ_{p1} , δ_{p2} , and δ_{p3} to the normalized differential phase velocity as a function of the frequency parameter χ for the wedge; $k = 1.0$ and Poisson ratio $\sigma = 0.16974$.

$$\frac{c_T}{\omega} e^{i(\beta z - \omega t)} \mathbf{u}|_{n=0} = \left[\frac{(b^2 + a_T^2)}{2a_T} - a_L \right] H \mathbf{n} + \left[1 - \frac{(b^2 + a_T^2)}{2b^2} \right] \left(\frac{1}{\chi} \frac{dH}{d\eta} \mathbf{t} - ibH \mathbf{k} \right), \quad (15)$$

where H satisfies the refined approximate equation

$$\frac{d^2 H}{d\eta^2} + \{ \chi [PK(\eta) - 2b\nu] - \nu^2 + \nu SK(\eta) - \tau [K(\eta)]^2 \} H = 0. \quad (16)$$

Here the frequency parameter χ is as defined in (2), $K(\eta)$ is the curvature function, $\eta = s/\ell$ as before, and P , S , and τ are constants. The parameter ν is an eigenvalue, which is to be determined from a periodicity condition in the case of a closed boundary curve, and from an appropriate condition at infinity in the case of an open boundary curve. The propagation constant β is given by

$$\beta \ell = b\chi + \nu, \quad (17)$$

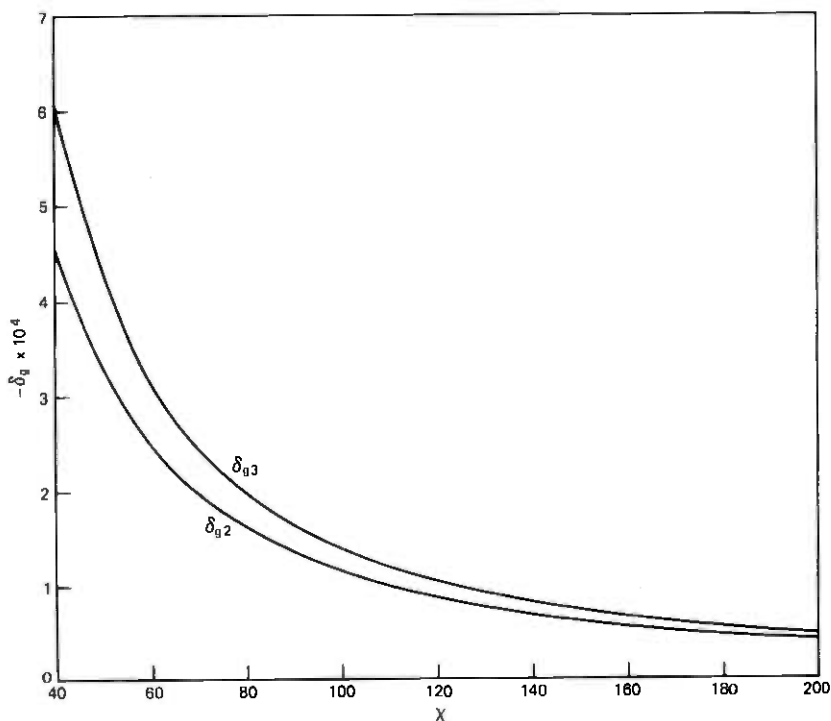


Fig. 12—Asymptotic approximations δ_{g2} and δ_{g3} to the normalized differential group velocity as a function of the frequency parameter χ for the wedge; $k = 1.0$ and Poisson ratio $\sigma = 0.16974$.

and the normalized phase and group velocities are

$$w_p = (b + \nu/\chi)^{-1}, \quad w_g = (b + d\nu/d\chi)^{-1}. \quad (18)$$

In this refined approximation, correction terms³ of order $1/\chi$ could be included in the \mathbf{n} and \mathbf{k} components of the surface displacement given by (15). However, for the numerical cases considered in this paper, it turns out that these corrections, which differ for the two components, are of at most a few percent, so we do not write out these terms here.

The lowest-order approximation B.0 (see Fig. 1) is obtained by omitting those terms multiplying H in (16) which are independent of χ . Having done this, we replace H by H_0 in (15) and ν by ν_0 in (17) and (18), where H_0 satisfies the lowest-order approximate equation

$$\frac{d^2 H_0}{d\eta^2} + \chi [PK(\eta) - 2b\nu_0] H_0 = 0. \quad (19)$$

It was shown³ that the asymptotic approximation (1) for the surface displacement of the zeroth-order mode may be derived from (15) and

Table I(a) — Asymptotic approximations to the normalized differential phase velocity of the zeroth-order mode for various cross-sectional shapes; frequency parameter $\chi = 80$ and Poisson ratio $\sigma = 0.16974$

Shape	h	$-\delta_{p1} \times 10^3$	$-\delta_{p2} \times 10^3$	$-\delta_{p3} \times 10^3$
Bore	0.3	-0.718	-1.072	-1.068
	0.4	-0.359	-0.767	-0.756
	0.5	0	-0.457	-0.442
Rod	0.1	2.15	1.95	1.86
	0.2	2.51	2.22	2.10
	0.3	2.87	2.52	2.35
	0.4	3.23	2.82	2.61
	0.5	3.59	3.13	2.87
Wedge	0.5	0.898	0.669	0.681
	1.0	1.80	1.47	1.43
	1.5	2.69	2.30	2.17
Ridged Plane	2	2.46	1.63	1.57
	3	3.69	2.67	2.45
	4	4.92	3.74	3.29
	5	6.15	4.83	4.09

Table I(b) — Asymptotic approximations to the normalized differential group velocity of the zeroth-order mode for various cross-sectional shapes; frequency parameter $\chi = 80$ and Poisson ratio $\sigma = 0.16974$

Shape	h	$-\delta_{g2} \times 10^4$	$-\delta_{g3} \times 10^4$
Bore	0.3	1.77	1.73
	0.4	2.04	1.92
	0.5	2.28	2.14
Rod	0.1	1.02	1.83
	0.2	1.44	2.60
	0.3	1.77	3.32
	0.4	2.04	4.04
	0.5	2.28	4.78
Wedge	0.5	1.14	1.02
	1.0	1.61	1.99
	1.5	1.98	3.18
Ridged Plane	2	4.17	4.65
	3	5.11	7.14
	4	5.90	10.10
	5	6.60	13.60

the refined approximate equation (16). Also, the lowest-order asymptotic approximation, in which the terms involving $C(\eta)[2(P\chi)^{1/2}]^{-1}$ do not appear in (1), may be derived from (19). However, in the transition region between the cases of nonconstant (and not "almost" constant) curvature and constant curvature, where the asymptotic results are not valid, eqs.

(16) and (19) have to be solved numerically, in general; it was shown,³ though, that (19) may be solved analytically in the case of the curvature function $K_3(\eta)$ given by (6). We will see later how the results obtained from the numerical solution of (16) and (19) compare with the asymptotic results A.0 and A.1 (Fig. 1) in their common region of validity.

As we will see, the lowest-order approximate eq. (19) is generally not sufficiently accurate in the transition region, when the curvature is "almost" constant. An exception is the case of the curvature function $K_3(\eta)$ given by (6), the reason being that the curvature is small in this case, tending to zero as $k \rightarrow 0$, so that the terms involving S and τ in (16) are small.

4.1 Circular bore

We first consider the case of a circular bore of radius ℓ , with $K(\eta) \equiv -1$, corresponding to $k = 0$ in (4). We compare our results from the lowest-order and refined approximate equations with the exact theoretical results⁴ for the fundamental mode in a circular bore.

For the lowest-order surface mode, with $K(\eta) \equiv -1$ in (16) and (19), both H_0 and H are constant, and the corresponding eigenvalues are

$$\nu_0 = -\frac{P}{2b}, \quad \nu = -\left(b\chi + \frac{S}{2}\right) \pm \left[\left(b\chi + \frac{S}{2}\right)^2 - (P\chi + \tau)\right]^{1/2}. \quad (20)$$

Note that $d\nu_0/d\chi = 0$, so that in the lowest-order approximation, from (18), the group velocity is equal to the Rayleigh wave velocity.

The exact theoretical dispersion relation for the fundamental mode in a circular bore was solved numerically for the normalized phase velocity w_p by Rosenberg, Schmidt, and Coldren⁶ for Poisson ratio $\sigma = 0.16974$, corresponding to fused silica. They also calculated the corresponding value of the normalized group velocity w_g . In Table II(a), we compare their values of w_p as a function of the frequency parameter χ with those calculated from (18) and (20). We add the subscripts L and R to w_p to denote the lowest-order and refined approximate values of the phase velocity, respectively. Similarly, in Table II(b), we compare the exact theoretical and refined approximate values of w_g . The normalized value of the Rayleigh wave velocity is $1/b = 0.905727$.

Notice that the lowest-order surface-wave approximation w_{pL} is reasonably close to w_p and that the refined surface-wave approximations w_{pR} and w_{gR} are remarkably close to w_p and w_g , respectively. The agreement improves as the frequency parameter χ increases.

Rosenberg, Schmidt, and Coldren⁶ plotted normalized differential phase and group velocities versus χ . In Fig. 13, for purposes of comparison, the normalized quantities $(bw - 1)/(b - 1)$ are plotted against χ for $w = w_{pL}, w_{pR}, w_p, w_{gR}$, and w_g . The dots are for values corresponding

Table II(a) — Comparison of lowest-order and refined approximate and exact theoretical values of the normalized phase velocity of the fundamental mode in a circular bore; frequency parameter χ has various values and Poisson ratio $\sigma = 0.16974$

χ	w_{pL}	w_{pR}	w_p
6	0.930315	0.938221	0.937969
8	0.924044	0.928858	0.928829
10	0.920321	0.923570	0.923583
12	0.917856	0.920199	0.920219
14	0.916104	0.917874	0.917893
16	0.914794	0.916179	0.916195
18	0.913777	0.914892	0.914905
20	0.912966	0.913882	0.913893
22	0.912303	0.913069	0.913078

Table II(b) — Comparison of refined approximate and exact theoretical values of the normalized group velocity of the fundamental mode in a circular bore; frequency parameter χ has various values and Poisson ratio $\sigma = 0.16974$

χ	w_{gR}	w_g
6	0.901046	0.902112
8	0.902532	0.902825
10	0.903408	0.903522
12	0.903968	0.903962
14	0.904347	0.904390
16	0.904615	0.904644
18	0.904812	0.904873
20	0.904961	0.904967
22	0.905077	0.905134

to w_p and w_g . Note that the normalized values of w_g do not lie precisely on a smooth curve. The values of w_g were obtained through numerical differentiation once the values of w_p had been calculated from the exact theoretical dispersion relation.⁶ We suspect that the discrepancy is due to numerical difficulties in their computations.

4.2 Ellipse-like bore and rod

We now consider the ellipse-like bore and rod corresponding to the curvature functions $K_1(\eta)$ and $K_2(\eta)$ given by (4) and (5). The eigenvalue problems for the refined and lowest-order approximate equations (16) and (19) were solved numerically. It suffices to consider the interval $0 \leq \eta \leq \pi/2$, because the modes are either symmetric or antisymmetric about $\eta = 0$, and about $\eta = \pi/2$, so that $H'(0) = 0$ or $H(0) = 0$, and $H'(\pi/2) = 0$ or $H(\pi/2) = 0$.

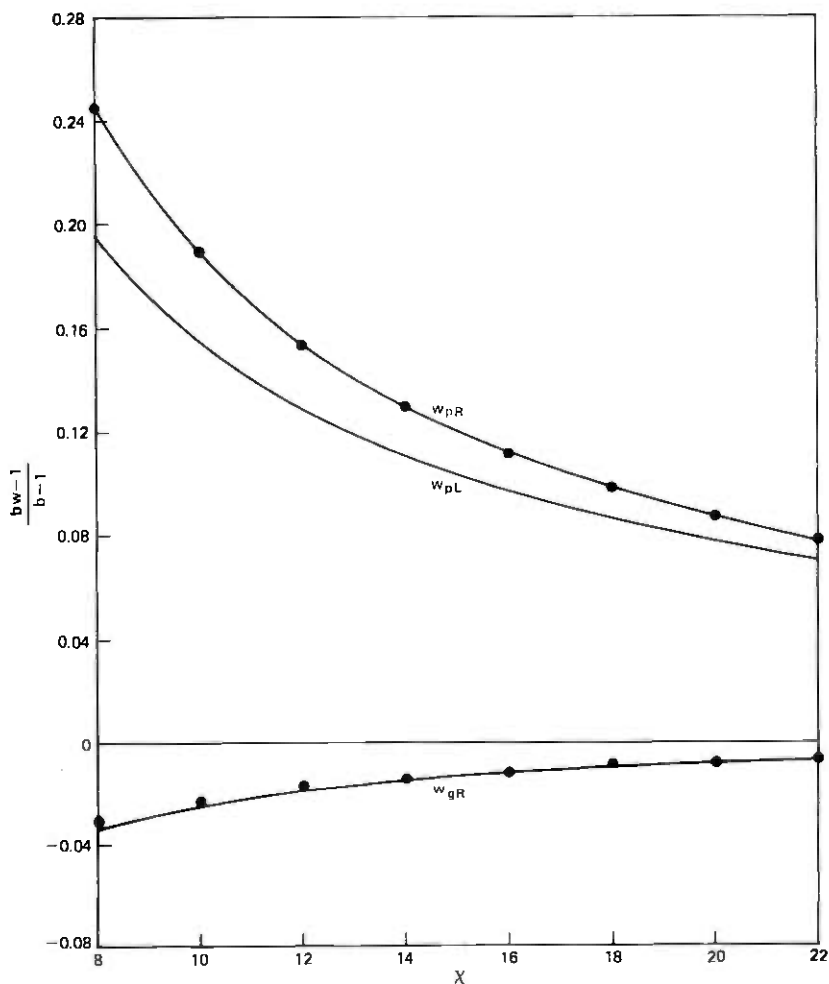


Fig. 13—Normalized differential phase and group velocities $(bw - 1)/(b - 1)$ as a function of the frequency parameter χ for the circular bore, with Poisson ratio $\sigma = 0.16974$. The curves correspond to the surface-wave approximations w_{pL} , w_{pR} , and w_{gR} and the dots correspond to the exact theoretical results w_p and w_g .

A "shooting" method was used, which involves making an initial guess for the eigenvalue ν , and numerically integrating the differential equation for $H(\eta)$ from $\eta = \pi/2$ to $\eta = 0$. The value of ν was adjusted iteratively, in the manner described in Appendix B, until the boundary condition at $\eta = 0$ was satisfied with sufficient accuracy. The initial iterations were done in single precision, and the final ones in double precision, and only a few iterations were required to obtain the desired accuracy. The numerical integrations were done from $\eta = \pi/2$ to $\eta = 0$, since in the asymptotic region the mode decays exponentially away from $\eta = 0$, and

integration from $\eta = 0$ toward $\eta = \pi/2$ would lead to numerical instabilities in this case.

To calculate both the phase and group velocities from (18), it is necessary to know the values of both ν and $d\nu/d\chi$. Once the eigenvalue ν , and the corresponding eigenfunction $H(\eta)$ had been obtained, the value of $d\nu/d\chi$ was obtained by quadratures, using the expression (46) derived in Appendix B. The analogous expression for $d\nu_0/d\chi$ is given by (47).

4.2.1 Rod

We first compare the results of the numerical solution of (16) and (19) for the rod [$k = 0.3$ in (5)] with the asymptotic results A.0 and A.1 for $\chi = 40$. Here, and subsequently, the value of Poisson's ratio is taken to be $\sigma = 0.16974$. In Fig. 14, we plot the refined and lowest-order surface-wave approximations $H(\eta)$ and $H_0(\eta)$ for the zeroth-order symmetric mode, normalized to unity at $\eta = 0$. The dots and circles correspond to the first and lowest-order asymptotic approximations $S_1(\eta)$ and $S_0(\eta)$, respectively, as defined in (10) and (9). It is seen that the asymptotic approximations agree quite well with the numerical solution, except, as expected, near $\eta = \pi/2$. As the value of χ increases, the agreement becomes better near $\eta = \pi/2$, since the disturbance becomes exponentially small there.

When the value of $S_1(\eta)$ is sufficiently small near $\eta = \pi/2$, the zeroth-order mode which is antisymmetric about $\eta = \pi/2$, as well as that mode which is symmetric about $\eta = \pi/2$, is approximated by $S_1(\eta)$, as was argued in an earlier paper.² In Fig. 15, we plot $H(\eta)$ for the lowest-order symmetric and antisymmetric modes. The dots, as before, corre-

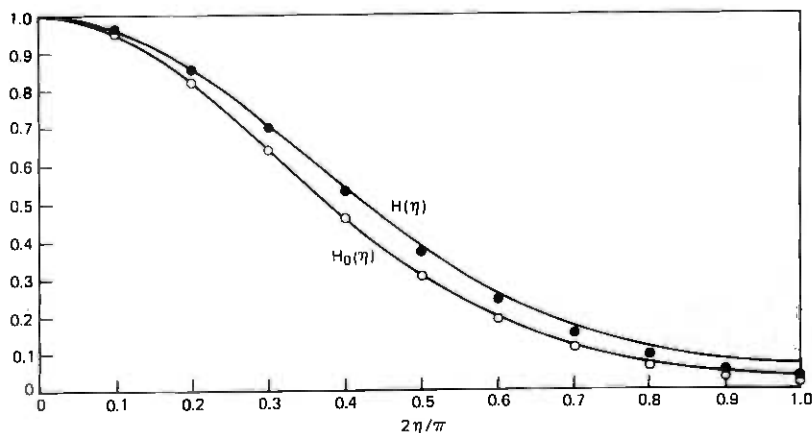


Fig. 14—Comparison of refined and lowest-order surface-wave approximations $H(\eta)$ and $H_0(\eta)$ for the zeroth-order symmetric mode, and corresponding asymptotic approximations $S_1(\eta)$ (dots) and $S_0(\eta)$ (circles) for the rod; $k = 0.3$, frequency parameter $\chi = 40$, and Poisson ratio $\sigma = 0.16974$.

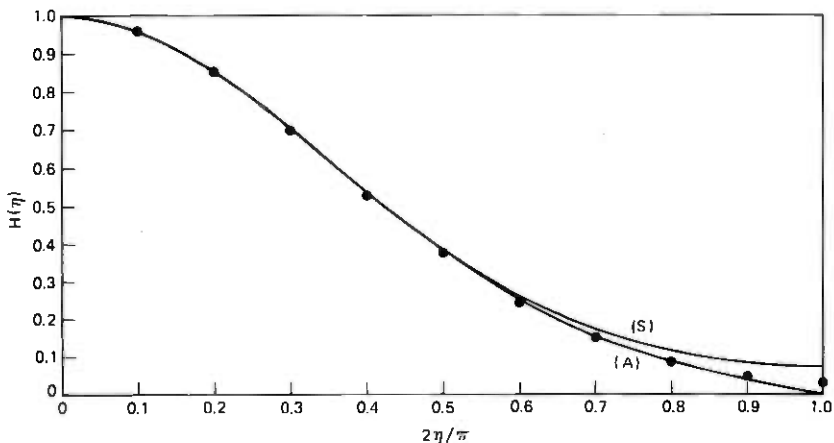


Fig. 15—Comparison of the refined surface-wave approximation $H(\eta)$ for the lowest-order symmetric (S) and antisymmetric (A) modes, and the first-order asymptotic approximation $S_1(\eta)$ (dots), for the rod; $k = 0.3$, frequency parameter $\chi = 40$, and Poisson ratio $\sigma = 0.16974$.

spond to the values of $S_1(\eta)$. To complete the comparison, in Table III we compare the asymptotic values of the differential phase and group velocities with the values obtained from (18).

Trends to notice are that the asymptotic approximations δ_{p2} and δ_{g2} to the differential phase and group velocities agree roughly with the lowest-order surface-wave approximations δ_{pL} and δ_{gL} . The correspondence between the next-order asymptotic approximations δ_{p3} and δ_{g3} and the refined surface-wave approximations δ_{pR} and δ_{gR} is somewhat better. The agreement is better for the differential phase velocities than it is for the differential group velocities. In all cases, the agreement improves as the frequency parameter χ increases.

As before, the t component of the displacement turns out to be a few percent of the n and k components of displacement.

Higher-order modes may be investigated also by solving the eigenvalue problem (16) numerically.

4.2.2 Bore

The agreement between the asymptotic and the numerical results is even better for the bore. We have already discussed the circular bore and we now consider the transition from this to a noncircular bore for which the asymptotic results are good, by letting k vary from 0 to $\frac{1}{2}$ in (4). The results of the numerical solution of the refined and lowest-order approximate equations (16) and (19) for $\chi = 40$ and $\sigma = 0.16974$ are depicted in Figs. 16 and 17 for the lowest-order symmetric and antisymmetric modes, respectively. The full curves give the values of $H(\eta)$ (re-

Table III — Comparison of asymptotic and approximate values of the normalized differential phase and group velocities of the lowest-order symmetric (S) and antisymmetric (A) modes for the rod; $k = 0.3$, frequency parameter χ has various values, and Poisson ratio $\sigma = 0.16974$

	χ		
	40	60	80
$-\delta_p \times 10^3$			
δ_{p1}	5.745	3.830	2.873
δ_{p2}	4.745	3.286	2.519
δ_{pL} (S)	4.783	3.3010	2.5271
(A)	4.780	3.3007	2.5271
δ_{p3}	4.089	2.9942	2.3550
δ_{pR} (S)	4.075	2.9925	2.3555
(A)	4.066	2.9919	2.3554
$-\delta_\mu \times 10^3$			
$\delta_{\mu2}$	0.500	0.2722	0.1768
$\delta_{\mu L}$ (S)	0.428	0.2433	0.1611
(A)	0.442	0.2448	0.1613
$\delta_{\mu3}$	1.120	0.5475	0.3317
$\delta_{\mu R}$ (S)	1.188	0.5693	0.3401
(A)	1.231	0.5730	0.3406

fined approximation) and the broken curves the values of $H_0(\eta)$ (lowest-order approximation); both curves are normalized to unity at $\eta = 0$ for the specified values of k .

For the symmetric mode, Fig. 16, $H_0(\eta) \equiv 1$ and $H(\eta) \equiv 1$ for $k = 0$, which agrees with the exact result for the circular bore. As k increases, the values of $H_0(\pi/2)$ and $H(\pi/2)$ decrease, becoming exponentially small for $k = 0.5$. It is seen that there is a significant difference between $H_0(\eta)$ and $H(\eta)$ for intermediate values of k . The lowest- and first-order asymptotic results agree very well with the numerical results obtained from (19) and (16) for $k = 0.5$. In Table IV we compare the lowest-order and refined approximations to the normalized differential phase and group velocities. We see that δ_{pL} and δ_{pR} differ by only a few percent; the agreement improves as k increases. The lowest-order approximation $\delta_{\mu L}$ for the normalized differential group velocity, however, is not very good, especially for the smaller values of k .

For the antisymmetric mode, Fig. 17, $H_0(\eta) = \cos \eta = H(\eta)$ for $k = 0$, which agrees with the exact result for the circular bore. The differences between $H_0(\eta)$ and $H(\eta)$, for intermediate values of k , are not as large as they are for the symmetric mode. It is noted that for $k = 0.5$, the curves of $H_0(\eta)$ and $H(\eta)$ are barely distinguishable from the corresponding ones

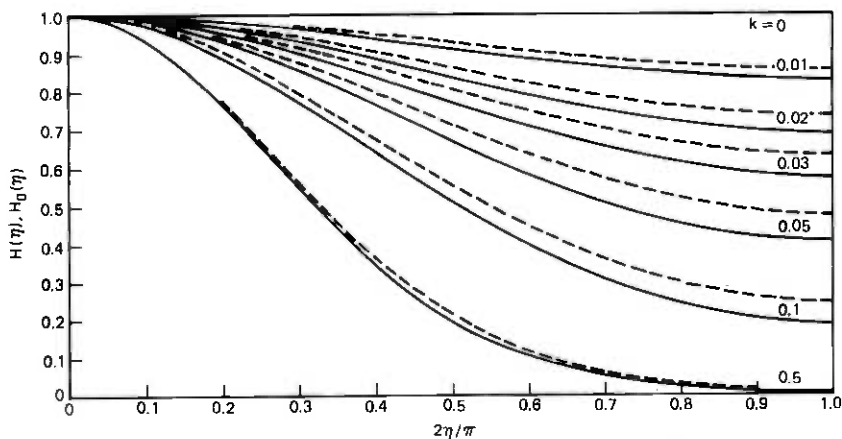


Fig. 16—Refined and lowest-order surface-wave approximations $H(\eta)$ (full curves) and $H_0(\eta)$ (broken curves) for the lowest-order symmetric mode for the bore; k has various values, frequency parameter $\chi = 40$, and Poisson ratio $\sigma = 0.16974$.

for the symmetric mode, as expected from the asymptotic results. The most significant difference is that $H_0(\pi/2) = 0 = H(\pi/2)$ for the antisymmetric mode, whereas $H_0(\pi/2) = 0 = H'(\pi/2)$ for the symmetric mode. In Table V, we compare the lowest-order and refined approximations to the normalized differential phase and group velocities. As was the case for the symmetric mode, δ_{pL} and δ_{pR} differ by a few percent and the agreement generally improves as k increases. The lowest-order approximation δ_{gL} for the normalized differential group velocity, although not very good quantitatively, is qualitatively better than for the symmetric mode.

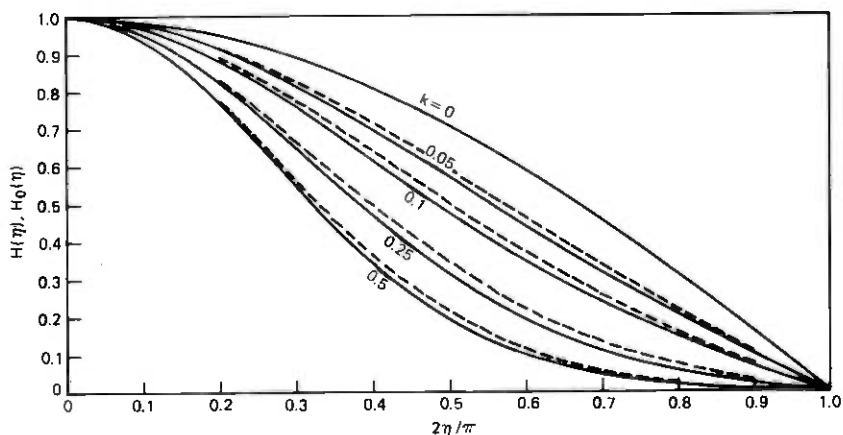


Fig. 17—Refined and lowest-order surface-wave approximations $H(\eta)$ (full curves) and $H_0(\eta)$ (broken curves) for the lowest-order antisymmetric mode for the bore; k has various values, frequency parameter $\chi = 40$, and Poisson ratio $\sigma = 0.16974$.

Table IV — Comparison of lowest-order and refined approximations to the normalized differential phase and group velocities of the lowest-order symmetric mode for the bore; k has various values, frequency parameter $\chi = 40$, and Poisson ratio $\sigma = 0.16974$

k	δ_{pL}	δ_{pR}	δ_{gL}	δ_{gR}
0	0.003605	0.003850	0	-0.224×10^{-3}
0.01	0.003602	0.003847	-0.275×10^{-5}	-0.226×10^{-3}
0.02	0.003594	0.003835	-0.108×10^{-4}	-0.234×10^{-3}
0.03	0.003580	0.003817	-0.234×10^{-4}	-0.247×10^{-3}
0.04	0.003562	0.003793	-0.396×10^{-4}	-0.262×10^{-3}
0.05	0.003539	0.003764	-0.583×10^{-4}	-0.279×10^{-3}
0.1	0.003374	0.003560	-0.162×10^{-3}	-0.358×10^{-3}
0.5	0.001232	0.001262	-0.581×10^{-3}	-0.636×10^{-3}

Table V — Comparison of lowest-order and refined approximations to the normalized differential phase and group velocities of the lowest-order antisymmetric mode for the bore; k has various values, frequency parameter $\chi = 40$, and Poisson ratio $\sigma = 0.16974$

k	δ_{pL}	δ_{pR}	δ_{gL}	δ_{gR}
0	0.003839	0.004066	-0.232×10^{-3}	-0.420×10^{-3}
0.01	0.003802	0.004024	-0.233×10^{-3}	-0.417×10^{-3}
0.02	0.003764	0.003981	-0.235×10^{-3}	-0.415×10^{-3}
0.03	0.003725	0.003936	-0.238×10^{-3}	-0.414×10^{-3}
0.04	0.003684	0.003890	-0.242×10^{-3}	-0.415×10^{-3}
0.05	0.003642	0.003842	-0.246×10^{-3}	-0.416×10^{-3}
0.1	0.003419	0.003590	-0.279×10^{-3}	-0.430×10^{-3}
0.5	0.001232	0.001262	-0.583×10^{-3}	-0.637×10^{-3}

4.3 Wedge

We now turn our attention to the wedge with a rounded tip, corresponding to the curvature function $K_3(\eta)$ given by (6). In this case, the lowest-order approximate equation (19) may be solved analytically.^{3,7} The eigenfunctions are

$$H_0(\eta) \propto (\operatorname{sech} \eta)^{a_m} F[2a_m + m + 1, -m; a_m + 1; \frac{1}{2}(1 - \tanh \eta)], \quad (21)$$

where

$$a_m = (P\chi k + \frac{1}{4})^{1/2} - m - \frac{1}{2} > 0, \quad m = 0, \dots, M, \quad (22)$$

and the corresponding eigenfunctions are given by

$$\nu_0 = a_m^2 / (2b\chi). \quad (23)$$

The hypergeometric function⁸ in (21) terminates, and is a polynomial of degree m in its argument. There is a finite number of modes, because of the requirement that $a_m > 0$, which ensures that $H_0(\eta) \rightarrow 0$ as $|\eta| \rightarrow \infty$. The even-order modes are symmetric about $\eta = 0$, and the odd-order modes are antisymmetric, so it suffices to consider $\eta \geq 0$.

According to (22), the zeroth-order mode, corresponding to $m = 0$, always exists for $k > 0$. For $m = 0$, the hypergeometric function in (21) is identically equal to 1. If $P\chi k < 2$, in this approximation, then only the zeroth-order mode exists. In the limiting case, $k \rightarrow 0$, corresponding to a planar boundary; $a_0 \rightarrow 0$ and $H_0 \rightarrow 1$, for fixed η . That is, the zeroth-order mode tends to a Rayleigh wave on a plane infinite half space as $k \rightarrow 0$.

The eigenvalue problem for the refined approximate equation (16), with $K(\eta)$ given by (6), was solved numerically by a shooting method after a transformation of the independent variable had been made to reduce the interval of integration to a finite one. The details are given in Appendix C. For the symmetric modes, $H'(0) = 0$, and for the antisymmetric modes, $H(0) = 0$. Once the eigenvalue ν , and the corresponding eigenfunction $H(\eta)$ had been obtained, the value of $d\nu/d\chi$ was obtained by quadratures, using the expression (53) derived in Appendix C. The values of ν and $d\nu/d\chi$ were used in (18) to obtain the normalized phase and group velocities.

In Fig. 18, we plot the refined and lowest-order surface-wave approximations $H(\eta)$ and $H_0(\eta)$, normalized to unity at $\eta = 0$, for the zeroth-order mode for the wedge for $k = 1$, $\chi = 40$, and $\sigma = 0.16974$. We also make a comparison with the asymptotic results, A.0 and A.1 (Fig.

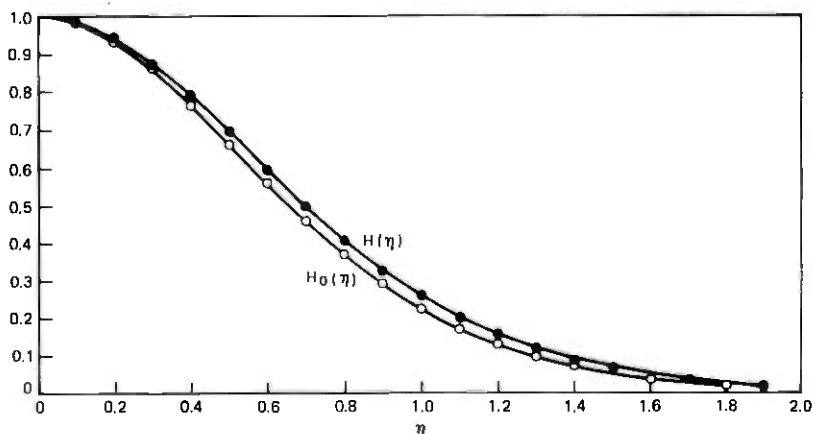


Fig. 18—Comparison of refined and lowest-order surface-wave approximations $H(\eta)$ and $H_0(\eta)$ for the zeroth-order mode, and corresponding asymptotic approximations $S_1(\eta)$ (dots) and $S_0(\eta)$ (circles) for the wedge; $k = 1.0$, frequency parameter $\chi = 40$, and Poisson ratio $\sigma = 0.16974$.

1), the dots and circles corresponding to the first- and lowest-order asymptotic approximations $S_1(\eta)$ and $S_0(\eta)$, respectively, as defined by (10) and (9). In Table VI, we compare the asymptotic values of the differential phase and group velocities with the values obtained from (18). The trends are similar to those we have noticed for the other cases. The asymptotic approximations δ_{p2} and δ_{g2} agree roughly with the lowest-order surface-wave approximations δ_{pL} and δ_{gL} . The higher-order asymptotic approximations δ_{p3} and δ_{g3} agree better with the refined surface-wave approximations δ_{pR} and δ_{gR} . The convergence is better for the differential phase velocities than it is for the differential group velocities; also, the agreement between the asymptotic and the surface-wave approximations is better.

In Figs. 19 and 20 we plot $H(\eta)$ and $H_0(\eta)$ for the remaining three modes. The odd-order, antisymmetric modes are normalized so that $H'(0) = 1$ and $H'_0(0) = 1$. In Table VII, we compare the corresponding values of the differential phase and group velocities.

Finally, we consider the transition region, between the case of non-constant (and not "almost" constant) curvature and constant curvature for the wedge, with $\chi = 40$ and $\sigma = 0.16974$. In Fig. 21, we plot $H(\eta)$ for the zeroth-order mode for several values of k between 0.01 and 1. We have not plotted $H_0(\eta)$ in this figure, since we compared $H_0(\eta)$ with $H(\eta)$ in Fig. 18 for $k = 1$ and found differences to be quite small for the smaller values of k . This is because the curvature is small when k is small, tending to zero as $k \rightarrow 0$, so that the terms involving S and τ in (16) are small. In Table VIII, we compare the lowest and refined approximations to the differential phase and group velocities as obtained from (18). In the transition region the agreement is good, both for the differential phase velocity and for the differential group velocity. As k increases and the lowest-order approximate equation becomes less accurate, discrepancies appear.

Table VI — Comparison of asymptotic and approximate values of the normalized differential phase and group velocities of the zeroth-order mode for the wedge; $k = 1.0$, frequency parameter $\chi = 40$, and Poisson ratio $\sigma = 0.16974$

$-\delta_p \times 10^3$	$\chi = 40$	$-\delta_g \times 10^3$	$\chi = 40$
δ_{p1}	3.591	—	—
δ_{p2}	2.678	δ_{g2}	0.457
δ_{pL}	2.778	δ_{gL}	0.351
δ_{p3}	2.515	δ_{g3}	0.605
δ_{pR}	2.521	δ_{gR}	0.614

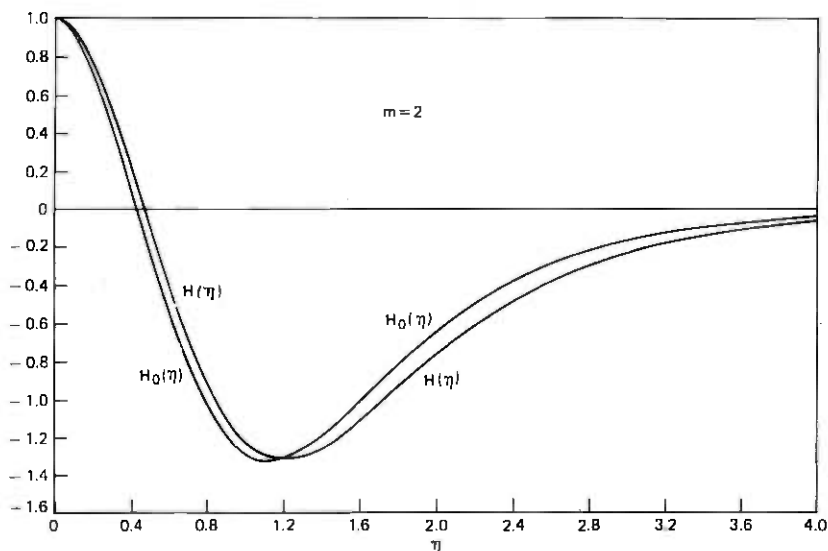


Fig. 19.—Refined and lowest-order surface-wave approximations $H(\eta)$ and $H_0(\eta)$ for the second-order mode for the wedge; $k = 1.0$, frequency parameter $\chi = 40$, and Poisson ratio $\sigma = 0.16974$.

V. SUMMARY

We made numerical computations to learn about the propagation of elastic surface waves along cylindrical objects roughly corresponding to an elliptical bore, an elliptical rod, a wedge with a rounded tip, and a flat plane with a rounded ridge. The cross-sectional curvature functions describing these objects are given by eqs. (4) to (7). In earlier papers,^{2,3} we had derived two approximate analytical descriptions of the surface-wave behavior: a high-frequency asymptotic approximation A, and one that we termed a surface-wave approximation B, as depicted in Fig. 1. Each of these approximations, in turn, was available in two forms: a lowest-order one and a higher-order or refined one. Here, we evaluated these approximations numerically.

We first performed a high-frequency asymptotic analysis of the disturbance in the vicinity of the cylinder surface and obtained the lowest-order, A.0, and next-higher-order, A.1, asymptotic approximations.² We used these approximations in the form shown in eq. (1), which describes the zeroth-order mode at the surface of the cylinder. For the bore and the rod, this equation corresponds to both the zeroth-order symmetric and antisymmetric modes. We also used the high-frequency asymptotic approximations to the phase and group velocities given by (12) and (13). The analysis involved two restrictions: the frequency had to be high enough that the disturbance was confined close to the surface

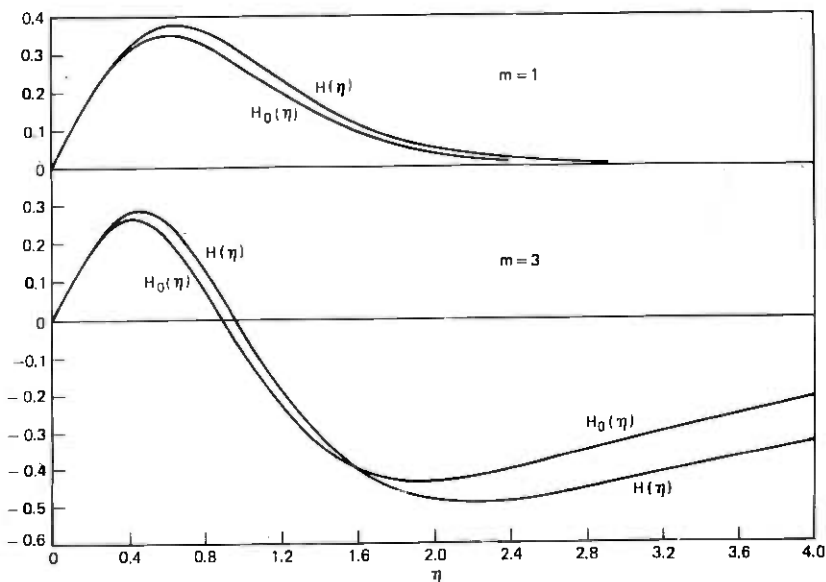


Fig. 20 — Refined and lowest-order surface-wave approximations $H(\eta)$ and $H_0(\eta)$ for the first- and third-order modes for the wedge; $k = 1.0$, frequency parameter $\chi = 40$, and Poisson ratio $\sigma = 0.16974$.

of the cylinder, and the deviation of the cross-sectional curvature from a constant value had to be sufficiently large that the disturbance was confined near points of maximum algebraic curvature.

We also were able to describe the mode behavior at the cylinder surface³ by the lowest-order, B.0, and refined, B.1, surface wave approximations (16) and (19). The phase and group velocities were given by (18). These surface-wave approximations B were subject to the same frequency restriction as were the asymptotic approximations A. In fact, the lowest-order and next-highest-order asymptotic approximations A.0 and A.1 for the zeroth-order mode could be obtained from the lowest-order and refined surface-wave approximations B.0 and B.1, respectively,

Table VII — Comparison of the lowest-order and refined approximations to the normalized differential phase and group velocities of the four modes for the wedge;
 $k = 1.0$, frequency parameter $\chi = 40$,
 and Poisson ratio $\sigma = 0.16974$

m	$-\delta_{\rho L} \times 10^3$	$-\delta_{\rho R} \times 10^3$	$-\delta_{\rho L} \times 10^3$	$-\delta_{\rho R} \times 10^3$
0	2.778	2.521	0.351	0.614
1	1.408	1.231	0.821	0.944
2	0.497	0.394	0.828	0.836
3	0.050	0.021	0.370	0.264

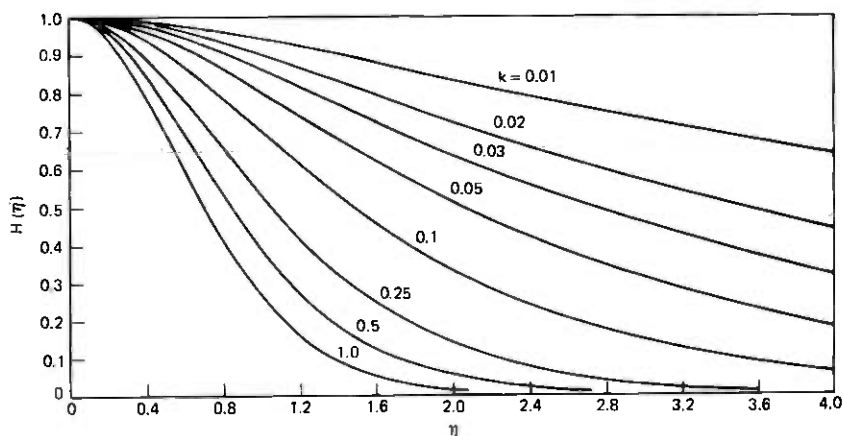


Fig. 21—Refined surface-wave approximation $H(\eta)$ for the zeroth-order mode for the wedge; various values of k , frequency parameter $\chi = 40$, and Poisson ratio $\sigma = 0.16974$.

provided that the above restriction on the cross-sectional curvature was satisfied.

The advantage of the surface-wave analysis B was that the curvature restriction could be dropped. It was possible, with the refined surface-wave approximation B.1 to describe the mode behavior, at high frequencies, in the transition region between the case of cross-sectional boundary curves of nonconstant (and not "almost" constant) curvature, for which the modes are localized, and the case of constant curvature, for which they are not localized. Also, the surface-wave approximations B permitted a more complete analysis of the higher-order modes. A disadvantage of the surface-wave approximations B was that they con-

Table VIII — Comparison of lowest-order and refined approximations to the normalized differential phase and group velocities of the zeroth-order mode for the wedge; k has various values, frequency parameter $\chi = 40$, and Poisson ratio $\sigma = 0.16974$

k	$-\delta_{pL} \times 10^3$	$-\delta_{pR} \times 10^3$	$-\delta_{gL} \times 10^4$	$-\delta_{gR} \times 10^4$
0.01	0.04302	0.04294	0.03381	0.03384
0.02	0.1426	0.1422	0.09537	0.09561
0.03	0.2763	0.2750	0.1635	0.1643
0.04	0.4333	0.4308	0.2324	0.2341
0.05	0.6076	0.6034	0.3003	0.3033
0.1	0.1639	0.1620	0.6116	0.6278
0.25	0.5424	0.5284	1.337	1.466
0.5	1.254	1.194	2.221	2.801
1.0	2.778	2.521	3.513	6.137

sisted of eigenvalue equations which, in general, had to be solved numerically. For the particular boundary curves chosen, the asymptotic approximations A involved little more than numerical evaluation of some analytical formulas, once the quadratures had been done analytically.

In general, we found numerically that the lowest- and next-higher-order asymptotic approximations A.0 and A.1 did agree with the lowest-order and refined surface-wave approximations B.0 and B.1, respectively, in their common region of validity. This was true both of the results for the disturbances, and for the phase and group velocities. The agreement improved as the frequency parameter χ was increased, and, for the phase and group velocities, was better between the higher-order and refined approximations than it was between the other two. The asymptotic and surface-wave approximations for the disturbance did not agree particularly well for the case of cylinders with closed boundary curves for values of η for which the disturbance was exponentially small. This was to be expected, since one expression had to suffice for both the lowest-order symmetric and antisymmetric modes in the asymptotic approximation A, while separate expressions were available in the surface-wave approximation B. We also used the refined surface-wave approximation B.1 numerically to describe disturbances in the transition region discussed earlier, and used the lowest-order and refined surface-wave approximations B.0 and B.1 to investigate the higher-order modes.

We turn now to a qualitative description of the numerical results. We first discuss the phenomenon of mode confinement and its dependence upon such things as the shape of the cylinder and the value of the frequency parameter χ . We then discuss our results for the phase and group velocities.

We found that the t component of the displacement for the lowest-order mode was only a few percent of the size of the n and k components. These latter two, when normalized to unity at $\eta = 0$, were either the same as a function of η (asymptotic theory A) or differed by a few percent at most (surface-wave theory B). It thus sufficed to consider a normalized scalar displacement function, rather than a vector function. The complete solution is essentially that for Rayleigh waves traveling on the surface of a plane infinite half space except that it is multiplied by a function of η , which describes the confinement of the wave due to the cylinder curvature, or, to be more precise, the confinement due to the deviation of the cylinder curvature function from a constant value. It is this confinement function (the normalized scalar displacement function) that we computed.

The wedge with a rounded tip and the plane with a ridge on it are cylinders whose cross-sectional boundaries are each described by a curvature function with a single algebraic maximum at $\eta = 0$. For these

cylinders, we found that the confinement function decays rapidly with $|\eta|$ away from its value of unity at $\eta = 0$. This means that the surface-wave disturbance is confined to the vicinity of the tip of the wedge or the ridge on the plane. In both cases, the amount of confinement decreases as the parameter k decreases and the cylinder becomes more nearly planar. For the ridged plane, we observed this when the curvature function was not "almost" constant (i.e., for k not too small). For the wedge, we also made computations for small values of k , corresponding to the flattening out of the wedge into a plane. Here we were aided by an analytical solution of the lowest-order surface wave approximation B.0. It showed that, as $k \rightarrow 0$, only the zeroth-order mode exists, that it is symmetric, and that it tends to a Rayleigh wave on a plane infinite half space. This was confirmed by the numerical computations, both in the lowest-order and in the refined surface-wave approximations B.0 and B.1.

We also plotted the confinement functions for higher-order modes on the wedge. For given values of k and the frequency parameter χ , there are finitely many surface modes. The even-order modes are symmetric about $\eta = 0$, and the odd-order modes are antisymmetric.

The ellipse-like rod and bore have boundary curves that are symmetric and which attain their algebraic maxima at two points, $\eta = 0$ and $\eta = \pi$. We investigated only the zeroth-order modes, although higher-order modes may also be studied numerically. The asymptotic approximation A for the zeroth-order mode on a rod or bore actually corresponds to two modes, a symmetric one and an antisymmetric one. These can be treated separately with the surface-wave approximation B. For a cylinder whose curvature is not "almost" constant, we observed confinement of the displacement to two regions. Each cylinder cross-section has two points of maximum algebraic curvature. They define two generators of the cylinder. The displacement is confined in the vicinity of these generators.

We considered the transition from an ellipse-like bore with the definite confinement properties discussed above to a circular bore ($k = 0$), which exhibits no confinement at all. For small values of k , it was necessary to use the refined surface-wave approximation B.1 rather than the lowest-order approximation B.0 in order to describe the modes adequately. We treated the lowest-order symmetric and antisymmetric modes. For $k = 0$, the results agreed with the known analytical results for a circular bore: the confinement function is constant for the symmetric mode and goes like $\cos \eta$ for the antisymmetric mode. As k increased, confinement began to appear. As k approached 0.5, there was definite confinement and the surface-wave approximate results B agreed with the asymptotic results A, which had been obtained earlier and which were valid for curvature functions that were not "almost" constant.

These were the basic confinement properties that we observed when we studied cylinders described by several different cross-sectional curvature functions with a variable parameter k . We also varied the frequency parameter χ and found that, for any given cylinder, the confinement becomes more pronounced as χ increases.

For most of the numerical computations we chose the Poisson ratio to be $\sigma = 0.16974$, corresponding to fused silica. A few computations were made with other values of σ ; we found that the confinement increases as σ decreases.

We also calculated the phase and group velocities. In the asymptotic approximation A, these are given by explicit asymptotic formulas. In the surface-wave approximation B, the velocities are given in terms of an eigenvalue and its derivative with respect to χ . The eigenvalue was determined from a periodicity condition in the case of a closed boundary curve and from an appropriate condition at infinity in the case of an open boundary curve. The derivative of the eigenvalue with respect to χ was expressed in terms of quadratures, which were evaluated numerically. This avoided the difficulty of numerical differentiation with respect to the frequency. Both the phase and group velocities tend to the Rayleigh wave velocity as $\chi \rightarrow \infty$. We computed the differential phase and group velocities normalized with respect to the transverse-wave velocity c_T .

The trends that we generally observed were that the asymptotic approximations δ_{p2} and δ_{g2} to the differential phase and group velocities agreed roughly with the lowest-order surface-wave approximations δ_{pL} and δ_{gL} . Better agreement was obtained between the next-order asymptotic approximations δ_{p3} and δ_{g3} and the refined surface-wave approximations δ_{pR} and δ_{gR} . The convergence and the agreement improve as the frequency parameter χ increases.

In the transition region between cylinders of constant curvature and those of not "almost" constant curvature (where the parameter k is small and the asymptotic theory is not valid), the lowest-order surface-wave approximation B.0, as expected, was not always too good, particularly for the differential group velocity, so it is necessary to use the refined surface-wave approximation B.1.

Finally, we compared the surface-wave approximation results B for the circular bore with exact theoretical results and obtained excellent agreement.

VI. ACKNOWLEDGMENTS

We are grateful to J. L. Blue and N. L. Schryer for several helpful discussions on some of the numerical procedures, and to R. L. Rosenberg for many helpful suggestions for improving the presentation.

APPENDIX A

We summarize here the asymptotic results² in terms of suitably normalized quantities. The longitudinal and transverse velocities are given by $c_L = [(\lambda + 2\mu)/\rho]^{1/2}$ and $c_T = (\mu/\rho)^{1/2}$, where λ and μ are Lamé's constants. Also, the Poisson ratio is $\sigma = \lambda[2(\lambda + \mu)]^{-1}$. The normalized Rayleigh wave velocity is $w_R = c_R/c_T$, where w_R is the root of the equation

$$(1 - \frac{1}{2}w_R^2)^4 = (1 - w_R^2) \left[1 - \frac{(1 - 2\sigma)}{2(1 - \sigma)} w_R^2 \right], \quad (24)$$

which satisfies $0 < w_R < 1$. We define the quantities

$$b = 1/w_R, a_L = \left[b^2 - \frac{(1 - 2\sigma)}{2(1 - \sigma)} \right]^{1/2}, a_T = (b^2 - 1)^{1/2}, \quad (25)$$

and

$$P = \frac{a_L a_T^2 (b^2 - a_L a_T)}{b^2 (a_L - a_T)^2 + 2a_L a_T^2 (a_L - a_T)} > 0. \quad (26)$$

We further define the quantities R and τ by means of the equations

$$4(a_L - a_T)[b^2(a_L - a_T) + 2a_L a_T^2]R = \frac{P^2(a_L - a_T)^2}{a_L^2 a_T^2} [b^2(a_L + a_T)^2 - 4a_L^2 a_T^2] + 2P[a_L(b^2 - a_L a_T) - a_T(a_L - a_T)^2] + [b^2(a_T^2 - 3a_L^2) + 2a_L a_T^3], \quad (27)$$

and

$$(a_L - a_T)[b^2(a_L - a_T) + 2a_L a_T^2](\tau + R) = P \left[\frac{b^2}{a_L a_T} (a_L^3 + a_T^3 - a_L^2 a_T) + a_L a_T (2a_L - 3a_T) \right]. \quad (28)$$

If η is small, the curvature function $K(\eta)$ has an expansion of the form

$$K(\eta) = d_0 + d_2 \eta^2 + d_3 \eta^3 + d_4 \eta^4 + \dots \quad (29)$$

There is no term proportional to η in (29), because of our assumption that the curvature attains its algebraic maximum at $\eta = 0$. It is assumed that $d_2 < 0$. We define the quantity

$$Q = \frac{11}{16} \left(\frac{d_3}{d_2} \right)^2 - \frac{3d_4}{4d_2} - \left(\frac{d_0 P}{2b} \right)^2 + d_0^2 R. \quad (30)$$

Then, from the asymptotic results,² the reciprocals of the normalized phase and group velocities defined in (11) have the expansions

$$\frac{1}{\omega_p} = b + \frac{d_0 P}{2b\chi} - \frac{(-d_2 P)^{1/2}}{2b\chi^{3/2}} + \frac{Q}{2b\chi^2} + \dots, \quad (31)$$

and

$$\frac{1}{\omega_g} = b + \frac{(-d_2 P)^{1/2}}{4b\chi^{3/2}} - \frac{Q}{2b\chi^2} + \dots. \quad (32)$$

If we expand the reciprocals of these expansions we obtain those given in (12) and (13).

We now define the functions $C(\eta)$, $F(\eta)$, $G(\eta)$, and $I(\eta)$ occurring in (1). In terms of the curvature function $K(\eta)$, we define

$$I(\eta) = [d_0 - K(\eta)]^{1/2} \operatorname{sgn} \eta, \quad (33)$$

and let

$$L(\eta) = \frac{[K'(\eta) + 2(-d_2)^{1/2}I(\eta)]}{4[d_0 - K(\eta)]}. \quad (34)$$

The prime denotes differentiation with respect to the argument, and it is seen from (29) that $L(0)$ is finite. Then, we define

$$F(\eta) = \exp \left[\int_0^\eta L(\zeta) d\zeta \right], \quad G(\eta) = \int_0^\eta I(\zeta) d\zeta. \quad (35)$$

Next, we let

$$M(\eta) = \int_0^\eta I(\zeta) K(\zeta) d\zeta, \quad (36)$$

and

$$N(\eta) = \int_0^\eta \{L'(\zeta) + [L(\zeta)]^2 - L'(0) - [L(0)]^2\} / I(\zeta) d\zeta. \quad (37)$$

Finally, we define

$$C(\eta) = N(\eta) - d_0 R G(\eta) + \tau M(\eta). \quad (38)$$

Then, from the asymptotic results,² the disturbance corresponding to the lowest-order mode can be expressed as

$$\frac{c_T e^{i(\beta z - \omega t)}}{\omega b^{(0)}(0)} \mathbf{u}(\Xi, \eta) = F(\eta) \exp[-(P\chi)^{1/2} G(\eta)] \left(\left[\frac{(b^2 + a_T^2)}{2a_T} e^{-a_T \chi \Xi} - a_L e^{-a_L \chi \Xi} \right] \right. \\ \times \left[1 + \frac{C(\eta)}{2(P\chi)^{1/2}} \right] \mathbf{n} - \left[e^{-a_L \chi \Xi} - \frac{(b^2 + a_T^2)}{2b^2} e^{-a_T \chi \Xi} \right] \\ \left. \times \left\{ \left(\frac{P}{\chi} \right)^{1/2} \mathbf{I}(\eta) \mathbf{t} + ib \left[1 + \frac{C(\eta)}{2(P\chi)^{1/2}} \right] \mathbf{k} \right\} \right). \quad (39)$$

APPENDIX B

We describe here the "shooting" method used to solve numerically the eigenvalue problems for the refined and lowest-order approximate equations (16) and (19) for the bore and rod, corresponding to the curvature functions $K_1(\eta)$ and $K_2(\eta)$ given by (4) and (5). It is desirable to shoot from $\eta = \pi/2$ to $\eta = 0$, since in the asymptotic region the mode decays exponentially away from $\eta = 0$, and integration from $\eta = 0$ toward $\eta = \pi/2$ would lead to numerical instabilities. Consequently, we let

$$\xi = \pi/2 - \eta, \quad Z_1(\xi) = H(\eta), \quad Z_2(\xi) = dZ_1/d\xi. \quad (40)$$

Since the eigenvalue ν has to be determined, we also consider the differential equations for

$$Z_3(\xi) = \frac{\partial Z_1}{\partial \nu}, \quad Z_4(\xi) = \frac{\partial Z_2}{\partial \nu}. \quad (41)$$

The initial conditions are taken as

$$Z_1(0) = 1, \quad Z_2(0) = 0, \quad \text{or } Z_1(0) = 0, \quad Z_2(0) = 1, \quad (42)$$

according to whether the mode is symmetric, or antisymmetric, about $\eta = \pi/2$. In either case, the remaining initial conditions are

$$Z_3(0) = 0, \quad Z_4(0) = 0. \quad (43)$$

An initial guess for the value of ν was made, and the system of equations for $Z_i(\xi)$, $i = 1, 2, 3, 4$, was integrated from $\xi = 0$ to $\xi = \pi/2$. When a mode symmetric about $\eta = 0$ was sought corresponding to $Z_2(\pi/2) = 0$, the initial value of ν was changed to $\nu - Z_2(\pi/2)/Z_4(\pi/2)$, since $Z_2(\pi/2, \nu + \delta) \approx Z_2(\pi/2, \nu) + \delta \partial Z_2 / \partial \nu (\pi/2, \nu)$. Analogously, if a mode antisymmetric about $\eta = 0$ was sought, corresponding to $Z_1(\pi/2) = 0$, then the initial value of ν was changed to $\nu - Z_1(\pi/2)/Z_3(\pi/2)$. The process of integrating the system of equations was repeated, until the boundary condition at

$\eta = 0$ was satisfied with sufficient accuracy. The initial iterations were done in single precision, and the final ones in double precision, and only a few iterations were required to obtain the desired accuracy.

The shooting program was checked in the case of the lowest-order approximate equation (19), since the eigenfunctions may be expressed in terms of Mathieu functions⁹ when the curvature function is given by (4) or (5). The checks were carried out for values of the parameter $q = P\chi k$ equal to 1, 5, and 10, the eigenvalues and eigenfunctions being checked against tabulated values.¹⁰

We now turn our attention to the calculation of $d\nu/d\chi$, which is needed to calculate the group velocity from (18). If we let $H_\chi = \partial H/\partial\chi$, then from (16) we obtain

$$\frac{d^2 H_\chi}{d\eta^2} + \{\chi[PK(\eta) - 2b\nu] - \nu^2 + \nu SK(\eta) - \tau[K(\eta)]^2\} H_\chi = \left\{ [2(b\chi + \nu) - SK(\eta)] \frac{d\nu}{d\chi} + [2b\nu - PK(\eta)] \right\} H(\eta). \quad (44)$$

Hence,

$$\frac{d}{d\eta} \left(H \frac{dH_\chi}{d\eta} - H_\chi \frac{dH}{d\eta} \right) = H \frac{d^2 H_\chi}{d\eta^2} - H_\chi \frac{d^2 H}{d\eta^2} = \left\{ [2(b\chi + \nu) - SK(\eta)] \frac{d\nu}{d\chi} + [2b\nu - PK(\eta)] \right\} [H(\eta)]^2. \quad (45)$$

But from the boundary conditions at $\eta = 0$ and $\eta = \pi/2$, it follows that $[H dH_\chi/d\eta - H_\chi dH/d\eta]_0^{\pi/2} = 0$. Hence, if we integrate (45) from $\eta = 0$ to $\eta = \pi/2$, we obtain

$$\frac{d\nu}{d\chi} \int_0^{\pi/2} [2(b\chi + \nu) - SK(\eta)] [H(\eta)]^2 d\eta = \int_0^{\pi/2} [PK(\eta) - 2b\nu] [H(\eta)]^2 d\eta. \quad (46)$$

Analogously, from (19), it follows that

$$2b\chi \frac{d\nu_0}{d\chi} \int_0^{\pi/2} [H_0(\eta)]^2 d\eta = \int_0^{\pi/2} [PK(\eta) - 2b\nu_0] [H_0(\eta)]^2 d\eta. \quad (47)$$

The program was written so that the system of equations for $Z_i(\xi)$, $i = 1, 2, 3, 4$, was augmented in the double-precision stage of the iterations to include the evaluation of the two quadratures in (46) or (47).

APPENDIX C

We describe here the "shooting" method, similar to that described in Appendix B, that was used to solve numerically the eigenvalue

problem for the refined approximate equation (16) for the wedge, corresponding to the curvature function $K_3(\eta)$ given by (6). From symmetry, it suffices to consider the interval $\eta \geq 0$. It is desirable to make a transformation of variables that reduces this interval to a finite one, particularly since we want to integrate from $\eta = \infty$ toward $\eta = 0$, in order to avoid numerical instabilities in the asymptotic region. Consequently, we introduce the new independent variable

$$\zeta = \frac{1}{2}(1 - \tanh \eta), \quad (48)$$

which is suggested by the form of the solution (21) of the lowest-order approximate equation (19). This form also suggests the substitution

$$H(\eta) = (\operatorname{sech} \eta)^\alpha g(\zeta), \quad \alpha = (2b\chi\nu + \nu^2)^{1/2} > 0. \quad (49)$$

From (6), (16), (48), and (49), it follows that

$$\begin{aligned} \zeta(1 - \zeta) \frac{d^2g}{d\zeta^2} + (\alpha + 1)(1 - 2\zeta) \frac{dg}{d\zeta} \\ + [(P\chi + \nu S)k - \alpha(\alpha + 1) - 4\tau k^2\zeta(1 - \zeta)]g = 0. \end{aligned} \quad (50)$$

The range of ζ is from 0 to $\frac{1}{2}$, with $\zeta = 0$ corresponding to $\eta = \infty$. Examination of the behavior of the solutions of (50) for $\zeta \rightarrow 0$, and the requirement that $H(\eta) \rightarrow 0$ as $\eta \rightarrow \infty$, lead to the condition that $g(0)$ be finite. The value of $g'(0)$ may be determined by setting $\zeta = 0$ in (50). Thus, as initial conditions, we take

$$g(0) = 1, \quad g'(0) = \alpha - (P\chi + \nu S)k/(\alpha + 1). \quad (51)$$

Since the eigenvalue ν has to be determined, we also consider the differential equation for $\partial g/\partial \nu$.

Because the coefficient of $d^2g/d\zeta^2$ in (50) vanishes at $\zeta = 0$, we let

$$\begin{aligned} Y_1 = g - 1, \quad Y_2 = dY_1/d\zeta - g'(0), \quad Y_3 = \partial Y_1/\partial \nu, \\ Y_4 = \partial Y_2/\partial \nu, \end{aligned} \quad (52)$$

so that $Y_i(0) = 0$, and $Y_i(\zeta)/\zeta$ is finite at $\zeta = 0$, $i = 1, 2, 3, 4$. The system of equations for $Y_i(\zeta)$ was integrated from $\zeta = 0$ to $\zeta = \frac{1}{2}$, the value of ν being adjusted after each step of the iteration procedure until the condition $g'(\frac{1}{2}) = 0$, or $g(\frac{1}{2}) = 0$, was satisfied with sufficient accuracy. The former condition corresponds to a mode that is symmetric about $\eta = 0$, and the latter to one that is antisymmetric.

It remains to discuss the calculation of $d\nu/d\chi$. If we integrate equation (45) from $\eta = 0$ to $\eta = \infty$, with $K(\eta)$ given by (6), it follows that

$$\frac{d\nu}{d\chi} \int_0^\infty [2(b\chi + \nu) - Sk \operatorname{sech}^2 \eta][H(\eta)]^2 d\eta$$

$$= \int_0^\infty (Pk \operatorname{sech}^2 \eta - 2b\nu)[H(\eta)]^2 d\eta. \quad (53)$$

In terms of the new variables given by (48), (49), and (52), this requires the evaluation of the definite integrals

$$\int_0^{1/2} [4\zeta(1-\zeta)]^\alpha [1 + Y_1(\zeta)]^2 d\zeta,$$

$$\int_0^{1/2} [4\zeta(1-\zeta)]^{\alpha-1} Y_1(\zeta)[2 + Y_1(\zeta)] d\zeta, \quad (54)$$

and the calculation of

$$\int_0^{1/2} [4\zeta(1-\zeta)]^{\alpha-1} d\zeta = \frac{\sqrt{\pi}\Gamma(\alpha)}{4\Gamma(\alpha + 1/2)}. \quad (55)$$

The integral in (55) was expressed in terms of gamma functions,¹¹ for which a double-precision routine was available, in order to avoid a singular integrand at $\zeta = 0$ when $0 < \alpha < 1$. The integrals in (54) were evaluated in the double-precision stage of the iterations by augmenting the system of equations for $Y_i(\zeta)$, $i = 1, 2, 3, 4$.

To check the accuracy of the shooting method, the analogous system of equations corresponding to the lowest-order approximate equation (19) was solved numerically, and the results were checked against those calculated from the analytical solution (21) to (23).

REFERENCES

1. J. A. Morrison, "Propagation of High Frequency Surface Waves Along Cylinders of General Cross-Section," *J. Math. Phys.*, **16** (September 1975), pp. 1786-1794.
2. L. O. Wilson and J. A. Morrison, "Propagation of High Frequency Elastic Surface Waves Along Cylinders of General Cross-Section," *J. Math. Phys.*, **16** (September 1975), pp. 1795-1805.
3. J. A. Morrison, "High Frequency Approximations for Elastic Surface Waves Propagating Along Cylinders of General Cross-Section," *J. Math. Phys.*, **17** (June 1976), pp. 958-963.
4. M. A. Biot, "Propagation of Elastic Waves in a Cylindrical Bore Containing a Fluid," *J. Appl. Phys.*, **23** (September 1952), pp. 997-1005.
5. P. Franklin, *Differential and Integral Calculus*, New York: McGraw-Hill, 1953, p. 223.
6. R. L. Rosenberg, R. V. Schmidt, and L. A. Coldren, "Interior-Surface Acoustic Waveguiding in Capillaries," *Appl. Phys. Lett.*, **25** (September 1974), pp. 324-326; also private communication.
7. P. M. Morse and H. Feshbach, *Methods of Theoretical Physics*, Pt. II, New York: McGraw-Hill, p. 1651.
8. M. Abramowitz and I. A. Stegun, *Handbook of Mathematical Functions*, Washington, D. C.: National Bureau of Standards, 1964, p. 556.
9. Ref. 8, pp. 721-750.
10. E. L. Ince, "Tables of the Elliptic Cylinder Functions," *Proc. Roy. Soc., Edinburgh*, **52** (October 1932), pp. 355-423.
11. Ref. 8, pp. 253-266.

Contributors to This Issue

M. Eisenberg, B.S.(E.E.), 1964, M.S. (E.E.), 1964, Ph.D.(E.E.), 1967, Massachusetts Institute of Technology, Bell Laboratories, 1967—. Mr. Eisenberg has worked on problems in the fields of queuing theory, network management, and network design. He is presently supervisor of the Network Engineering Group. Member, Operations Research Society of America, Sigma Xi, Tau Beta Pi, Eta Kappa Nu.

Enrique A. J. Marcatili, Aeronautical Engineer, 1947, and E.E., 1948, University of Cordoba (Argentina); research staff, University of Cordoba, 1947-54; Bell Laboratories, 1954—. Mr. Marcatili has engaged in theory and design of filters in multimode waveguides and in waveguide systems research. As head of the transmission and circuit research department, he is concerned with optical transmission media, with circuitry for long-distance communication, and with integrated optics. Fellow IEEE; member of NAE.

John A. Morrison, B.Sc., 1952, King's College, University of London; Sc.M., 1954, and Ph.D., 1956, Brown University; Bell Telephone Laboratories, 1956—. Mr. Morrison has done research in various areas of applied mathematics and mathematical physics. His recent interests have included stochastic differential equations and propagation in random media, electromagnetic scattering by raindrops, and the high-frequency propagation of surface waves. He was a Visiting Professor of Mechanics at Lehigh University during the Fall semester 1968. Member, American Mathematical Society, SIAM, Sigma Xi.

F. W. Mounts, E.E., 1953; M.S., 1956, University of Cincinnati; Bell Telephone Laboratories, 1956—. Mr. Mounts has been concerned with research in efficient methods of encoding pictorial information for digital television systems. Member, Eta Kappa Nu; Senior Member, IEEE.

Willis M. Muska, A.A.S. Electronic Technology, 1967, Old Dominion Technical Institute; Bell Laboratories, 1967—. Mr. Muska has worked on hybrid integrated circuits for millimeter waveguide repeaters and

optical integrated circuits. More recently he has been involved in digital repeater techniques and systems for optical fiber transmission.

Arun N. Netravali, B. Tech. (Honors), 1967, Indian Institute of Technology, Bombay, India; M.S., 1969 and Ph.D. (E.E.), 1970, Rice University; Optimal Data Corporation, Huntsville, Alabama, 1970-1972; Bell Laboratories, 1972—. Mr. Netravali has worked on various aspects of signal processing. Member, Tau Beta Pi, Sigma Xi.

Birendra Prasada, B.S., 1953, M.S., 1955, Banaras University; Ph.D., 1960, University of London; Central Electronics Engineering Research Institute, Pilani, India, and Defence Science Laboratory, Delhi, India, 1961-1963; Massachusetts Institute of Technology, 1965-1966; Indian Institute of Technology, 1968-1972; Bell Laboratories, 1963-1965, 1973-1976. Mr. Prasada's main research and teaching interests are in the areas of visual communications, systems engineering, systems design, and human communication. He has worked as an industrial consultant in India and the United States. Member, 1963, Senior Member 1976, IEEE.

Judith B. Seery, B.A., 1968, College of St. Elizabeth; M.S., 1972, New York University; Bell Laboratories, 1968—. Ms. Seery does computing and analysis in the Mathematics and Statistics Research Center. She has recently participated in problems in fiber optics, minimal spanning networks, and multidimensional scaling. Member, Mathematical Association of America, Association for Women in Mathematics.

Lynn O. Wilson, A.B. (Physics), 1965, Oberlin College; Ph.D. (Applied Mathematics), 1970, University of Wisconsin; Bell Laboratories, 1970—. Ms. Wilson has pursued research in various areas of applied mathematics. She has worked on problems concerning *Picturephone*® demand, electromagnetic theory, dielectric waveguides, elastic surface waves, and crystalline vibrations. Member, Sigma Xi, American Physical Society, SIAM.

Abstracts of Papers by Bell System Authors Published in Other Journals

CHEMISTRY

The Electrical Conductivity of Fluid Selenium Up to Supercritical Temperatures and Pressures. H. Hoshino*, R. W. Schmutzler[†], W. W. Warren, and F. Hensel, *Phil. Mag.*, 33, No. 2 (1976), pp. 255-259. The electrical conductivity of fluid selenium has been measured as a function of temperature and pressure to 1750°C and 1200 bars, respectively. The conductivity isobars exhibit strong increases to nearly metallic behavior in selenium above 1300°C at supercritical pressures. Above 1500-1600°C the conductivity isobars drop sharply toward more insulating behavior. *Hokkaido University, Japan; [†] Philipps Universität, Germany.

Excited State Bromine Atom and Molecule Reactions. K. B. McAfee, Jr., R. M. Lum, and R. S. Hozack *J. Chem. Phys.* 64, No. 12 (June 15, 1976), pp. 5073-5076. Using a novel capillary optical reactor to shorten drastically free radical chain lengths, we have separately identified and followed substitution and photo-addition reactions of excited $^2P_{1/2}$ and ground state $^2P_{3/2}$ bromine atoms with propylene. Evidence for reactions of electronically excited bromine molecules ($B^3\Pi_u^+$) has also been obtained.

Non-bonded vs. Bonded Interactions in $(Ph_3P)_4Ag_2Br_2-(Ph_3P)_4Ag_1Br_4$ and its Stereochemical Analogue $[(RS)_4Fe_2S_2]^{2-}-[(RS)_4Fe_4S_4]^{2-}$. Boon-Keng Teo and Joseph C. Calabrese*, *J. C. S. Chem. Comm.* (1976), pp. 185-186. The stereochemistry of the metal-metal nonbonded dimer-tetramer pair $(Ph_3P)_4Ag_2Br_2-(Ph_3P)_4Ag_1Br_4$ exhibits trends resembling those of the structurally analogous metal-metal bonded pair $[(RS)_4Fe_2S_2]^{2-}-[(RS)_4Fe_4S_4]^{2-}$, indicating that the metal atoms within each pair probably bear similar gross atomic charges.

*University of Wisconsin, Madison.

ELECTRONIC AND ELECTRICAL ENGINEERING

Continuous Room-Temperature Operation of GaAs-Al_xGa_{1-x}As Double-Heterostructure Lasers Prepared By Molecular-Beam Epitaxy. A. Y. Cho, R. W. Dixon, H. C. Casey, Jr., and R. L. Hartman, *Appl. Phys. Lett.*, 28, No. 9 (May 1, 1976), pp. 501-503. The continuous (cw) operation at temperatures as high as 100°C of stripe-geometry GaAs-Al_xGa_{1-x}As double-heterostructure lasers fabricated by molecular-beam epitaxial (MBE) techniques has been achieved. Improved MBE laser performance was the result of the extensive efforts to eliminate hydrocarbon and water vapor from the growth apparatus. For 12- μ m-wide stripe-geometry lasers with 380- μ m-long cavities, the cw threshold currents varied between 163 and 297 mA at room temperature.

GaAs MESFET Prepared by Molecular Beam Epitaxy (MBE). A. Y. Cho and D. R. Ch'en*, *Appl. Phys. Lett.*, 28, No. 1 (January 1, 1976), pp. 30-31. GaAs metal-semiconductor field-effect transistors (MESFET) have been prepared by molecular-beam epitaxy. At 6 GHz a noise figure of 3 dB was obtained with a corresponding gain of 10 dB. The transconductance of the device was 28 mmhos and F_{max} was approximately 35 GHz.

*Avantek, Santa Clara, California.

On Solving the Transient, Conducting Slab With Radiating and Convecting Surfaces. J. L. Milton and W. P. Goss*, *Trans. ASME, J. Heat Transf.*, 97 (November 1975), pp. 630-631. Physical reasoning has been employed to develop stability criteria for explicit finite-difference solutions to transient conducting slabs with (nonlinear) radiating and convecting surfaces. The "derivative method" of stability analysis requires $\partial T^{new}/\partial T^{old} \geq 0$. The "explicit method" requires that the positive (real) root of the governing quartic polynomial be determined. Favorable comparison of the methods is reported.

MATERIALS SCIENCE

Effect of Hydrogen on Amorphous Silicon. J. J. Hauser, *Solid State Commun.*, 19 (1976), pp. 1049-1051. Amorphous Si films prepared by dc sputtering in hydrogen—argon mixtures possess a high resistivity ($\approx 10^{10} \Omega\text{-cm}$) similar to that of films prepared by the glow discharge decomposition of silane.

PHYSICS

Distribution Coefficient of P for Growth of $\text{Ga}_{1-x}\text{Al}_x\text{As}_{1-y}\text{P}_y$ by LPE Determined Using Auger Spectroscopy. C. C. Chang, M. B. Panish, W. R. Wagner, D. L. Rode, S. Sumski and R. G. Sobers, *J. Appl. Phys.*, 47 (1976), pp. 3752-3753. Auger spectroscopy was combined with ion milling for quantitative chemical analysis and depth profiling to measure the effective distribution coefficient of phosphorus, k_p , during growth of $\text{Ga}_{1-x}\text{Al}_x\text{As}_{1-y}\text{P}_y$ by liquid phase epitaxy. Below $y = 0.02$ (with $x = 0.36$), and with cooling rate of $0.1^\circ\text{C}/\text{min}$ for growth, k_p was 290 at growth temperature of 790°C and constant down to at least $y = 0.002$. This high value of k_p caused depletion of P from the growth solution.

Implications of Radiative Equilibrium in Neoclassical Theory. F. R. Nash and J. P. Gordon, *Phys. Rev. A, Gen. Phys.*, 12, No. 6 (December 1975), pp. 2472-2486. It is found that the description of spontaneous emission provided by the neoclassical extension of semiclassical electrodynamics, which has been given by Jaynes and his collaborators, is inconsistent with the well-secured laws of Boltzmann and Planck for conditions of thermal equilibrium.

Nd:YAG Single-Crystal Fiber Laser: Room-Temperature CW Operation Using a Single LED as an End Pump. J. Stone, C. A. Burrus, A. G. Dentai, and B. I. Miller, *Appl. Phys. Lett.*, 29, No. 1 (July 1, 1976), pp. 37-39. CW laser action has been obtained using as-grown single-crystal Nd:YAG fibers end-pumped by a single high-radiance LED. The fibers were 0.5 cm long and $80 \mu\text{m}$ in diameter, and the diameter of the LED luminous area was $85 \mu\text{m}$. The lowest cw laser threshold was observed at a diode drive current of 45 mA.